SANDIA REPORT

SAND2016-9762
Unlimited Release
Printed September, 2016

The Arctic Coastal Erosion Problem

Jennifer M. Frederick, Matthew A. Thomas, Diana L. Bull, Craig A. Jones, and Jesse D. Roberts

Prepared by
Sandia National Laboratories
Albuquerque, New Mexico 87185 and Livermore, California 94550

Sandia National Laboratories is a multi-mission laboratory managed and operated by Sandia Corporation, a wholly owned subsidiary of Lockheed Martin Corporation, for the U.S. Department of Energy's National Nuclear Security Administration under contract DE-AC04-94AL85000.

Sandia National Laboratories
PO Box 5800, MS 0747
Albuquerque, NM, 87185-0747

Sandia National Laboratories

Issued by Sandia National Laboratories, operated for the United States Department of Energy by Sandia Corporation.

Available to DOE and DOE contractors from
U.S. Department of Energy
Office of Scientific and Technical Information
P.O. Box 62
Oak Ridge, TN 37831

Telephone: (865) 576-8401
Facsimile: (865) 576-5728
E-Mail: reports@adonis.osti.gov
Online ordering: http://www.osti.gov/bridge

Available to the public from
U.S. Department of Commerce
National Technical Information Service
5285 Port Royal Rd
Springfield, VA 22161

Telephone: (800) 553-6847
Facsimile: (703) 605-6900
E-Mail: orders@ntis.fedworld.gov
Online ordering: http://www.ntis.gov/help/ordermethods.asp?loc=7-4-0#online

SAND2016-9762
Unlimited Release
Printed September, 2016

The Arctic Coastal Erosion Problem

Jennifer M. Frederick
jmfrede@sandia.gov

Matthew A. Thomas
mthoma2@sandia.gov

Diana L. Bull
dlbull@sandia.gov

Craig A. Jones
cjones@integral-corp.com

Jesse D. Roberts
jdrober@sandia.gov

Contents

List of Figures

Executive Summary

Permafrost-dominated coastlines in the Arctic are rapidly disappearing. Arctic coastal erosion rates in the United States have doubled since the middle of the twentieth century and appear to be accelerating. Positive erosion trends have been observed for highly-variable geomorphic conditions across the entire Arctic, suggesting a major (human-timescale) shift in coastal landscape evolution. Unfortunately, irreversible coastal land loss in this region poses a threat to native, industrial, scientific, and military communities.

The Arctic coastline is vast, spanning more than 100,000 km across eight nations, ten percent of which is overseen by the United States. Much of area is inaccessible by all-season roads. People and infrastructure, therefore, are commonly located near the coast. The impact of the Arctic coastal erosion problem is widespread. Homes are being lost. Residents are being dispersed and their villages relocated. Shoreline fuel storage and delivery systems are at greater risk. The U.S. Department of Energy (DOE) and Sandia National Laboratories (SNL) operate research facilities along some of the most rapidly eroding sections of coast in the world. The U.S. Department of Defense (DOD) is struggling to fortify coastal radar sites, operated to ensure national sovereignty in the air, against the erosion problem.

Rapid alterations to the Arctic coastline are facilitated by oceanographic and geomorphic perturbations associated with climate change. Sea ice extent is declining, sea level is rising, sea water temperature is increasing, and permafrost state is changing. The polar orientation of the Arctic exacerbates the magnitude and rate of the environmental forcings that facilitate coastal land area loss. The fundamental mechanics of these processes are understood; their non-linear combination poses an extreme hazard. Tools to accurately predict Arctic coastal erosion do not exist. To obtain an accurate predictive model, a coupling of the influences of evolving wave dynamics, thermodynamics, and sediment dynamics must be developed. The objective of this document is to present the state-of-the-science and outline the key steps for creation of a framework that will allow for improved prediction of Arctic coastal erosion rates. This is the first step towards the quantification of coastal hazards that will allow for sustainable planning and development of Arctic infrastructure.

This report is organized into six chapters:

- Chapter 1: Problem Statement and Infrastructure Concerns
- Chapter 2: Review of Arctic Coastal Erosion Studies: Observations and Trends
- Chapter 3: Changes in Arctic Sea Ice and Oceanographic Conditions
- Chapter 4: Arctic Coastal Geomorphology
- Chapter 5: Review of Existing Models
- Chapter 6: Putting It All Together to Create a Predictive Tool

Chapter 1 provides a snapshot of the magnitude of Arctic coastal erosion as well the social and economic costs associated with the hazard. The consistency in erosion trends is indicative of a major disruption to oceanographic/geomorphic equilibrium. Billions of dollars are being spent to relocate or fortify infrastructure.

Chapter 2 synthesizes decades of observation-based studies aimed at quantifying long-term rates of coastal erosion across the Arctic. These kinds of studies typically rely upon ground survey, aerial imagery, or remotely-sensed data. The collective efforts of researchers leads to a fairly consistent conclusion: erosion rates in the Alaskan Arctic are among the highest in the world and they are accelerating.

Chapter 3 discusses how Arctic Ocean conditions are changing. Sea ice is melting earlier and forming later. Perennial ice is being replaced by thinner first-year ice. By some accounts, the Arctic Ocean may experience ice-free summers by 2018. As the duration of open water conditions in the Arctic increases, more powerful ocean waves are expected to form. These changes will facilitate the delivery of heat to the permafrost-laden coastlines of the Arctic.

Chapter 4 describes the characteristics of permafrost in the Arctic and discusses those traits relative to the geomorphic nature of the coastline. The character of Arctic coastal permafrost varies widely. Some of the permafrost coastlines are lithified, but many consist of unconsolidated sediment with grain sizes ranging from fine to coarse. It is not uncommon for the volumetric ice content of the permafrost to be greater than 50 percent. The sediment type and degree to which the permafrost is ice-bonded affects its thermal and mechanical (i.e., sediment strength) properties.

Chapter 5 reviews the models that have been (or could be) used to model oceanographic and geomorphic conditions in the Arctic. Wave, sea-ice, near-shore circulation, permafrost thermal, and permafrost erosion models are discussed. Ocean wave modeling is a well-established discipline, but understanding of how waves form and propagate in the vicinity of sea-ice is an area of active research with efforts split among wave-ice, weather and storm ocean-ice, and earth systems models. Near-shore circulation modeling is also a well-established method that is critical to finely resolve the sea water-temperature, -salinity, -velocity, and -level in the vicinity of a permafrost bluff. Permafrost thermal model complexity often depends upon the scale of interest. Physically-based thermal models, typically employed at the field scale, are highly parameterized. Earth system thermal models require simplifying assumptions about the physics, but can be applied on regional scales. Existing permafrost bluff erosion models are typically calibrated to operate within a narrow range of geomorphic conditions. A common theme that emerges from the literature is that water setup (i.e., depth and duration) and temperature are first-order controls on the rate of erosion.

Chapter 6 provides an outline for a new modeling strategy that could be used to predict coastal erosion rates in the Arctic. The inputs and outputs of each major model type (i.e., the sea-ice-wave model, ocean circulation model, permafrost thermal model, and the permafrost erosion model) are presented. Ten advancements associated with the proposed effort are identified. These improvements will introduce more physical processes into each

model component and result in a degree inter-model coupling greater than previous efforts.

Despite the fact that the Arctic coastline comprises one-third of the global coastline length, much of our current understanding of coastal landscape evolution is applicable to coasts that are fundamentally different than the Arctic. This whitepaper demonstrates that Arctic coastal erosion is driven by complex oceanographic and geomorphic feedbacks. The social and economic costs associated with these destructive processes are large. Although surrogate-type models have shown promise, care should be taken such that the hydrologic, thermal, and mechanical processes associated with the Arctic system are properly coupled. With this complete approach, models based upon ground truth and physical parameters will facilitate the process-based understanding needed to inform Arctic stakeholders.

Chapter 1

Problem Statement and Infrastructure Concerns

Recent Observations Show Rates of Arctic Coastal Erosion Are Increasing

One-third of the coastline in the world is Arctic permafrost [*Lantuit et al.*, 2012]. Despite this sizeable proportion, a comprehensive understanding of erosion dynamics in the Arctic has not yet emerged. Unfortunately, the majority of present knowledge regarding coastal landscape evolution is confined to areas with temperate climates and non-cohesive sediments. Oceanographic and geomorphic feedbacks in the Arctic may be complex, but the need to interrogate these processes with physics-based modeling is becoming increasingly important. This urgency is underscored by scientific work that demonstrates erosion rates for many Arctic locations are increasing.

The American and Canadian coastlines exhibit the highest erosion rates in the Arctic (Figure 1.1). These annual rates are also among the greatest in the world. For example, if one considers that the annual erosion in the Arctic is typically limited to a three-month window, the adjusted erosion rates can be eight times greater than those in the Gulf of Mexico [*Reimnitz et al.*, 1988]. Analysis of aerial photography for a section of the Alaskan Arctic coast reveals erosion rates for 1955-1979, 1979-2002, and 2002-2007 increasing as 6.8, 8.7, and 13.6 m yr^{-1} [*Jones et al.*, 2009]. A duplication and update of this analysis shows good agreement with the positive trend. *Arp et al.* [2010] found erosion rates for 1955-1979, 1979-2002, 2002-2007, and 2007-2009 increasing as 6.0, 8.3, 13.9, and 17.3 m yr^{-1}. These data suggest that erosion rates in the Arctic have doubled within the time period of interest (Figure 1.3). Using remotely-sensed imagery, *Mars & Houseknecht* [2007] also report a doubling in the rate of permanent Alaskan Arctic land area loss (i.e., 0.5 to 1.1 km^2 yr^{-1}). The increase in erosion rates transcends coastal geomorphic conditions. For example, *Jones et al.* [2009] show annual erosion rates increasing across all of the geomorphic zones in their study area (Figure 1.2). Moreover, the increase in annual erosion rates is not limited to the Alaskan and Canadian coastline. *Vasiliev et al.* [2005] calculate Eastern Siberia coastal erosion rates for 1961-1968, 1990-1998, and 1998-2010 increasing as 0.6, 2.8, and 4.8 m yr^{-1}.

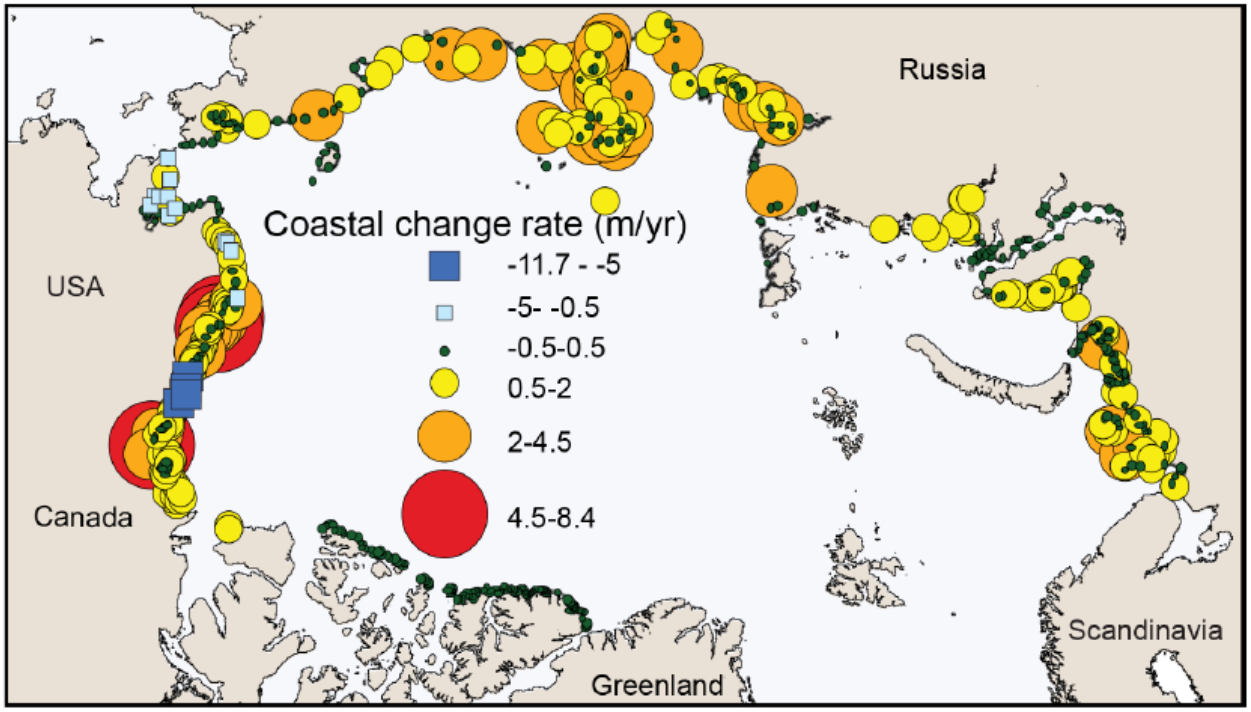

Figure 1.1. Coastal erosion rates along the circum-Arctic. The highest erosion rates are seen along the U.S. and Canadian Beaufort Sea coast. Adapted from *Barnhart et al.* [2014a]; *Lantuit et al.* [2012].

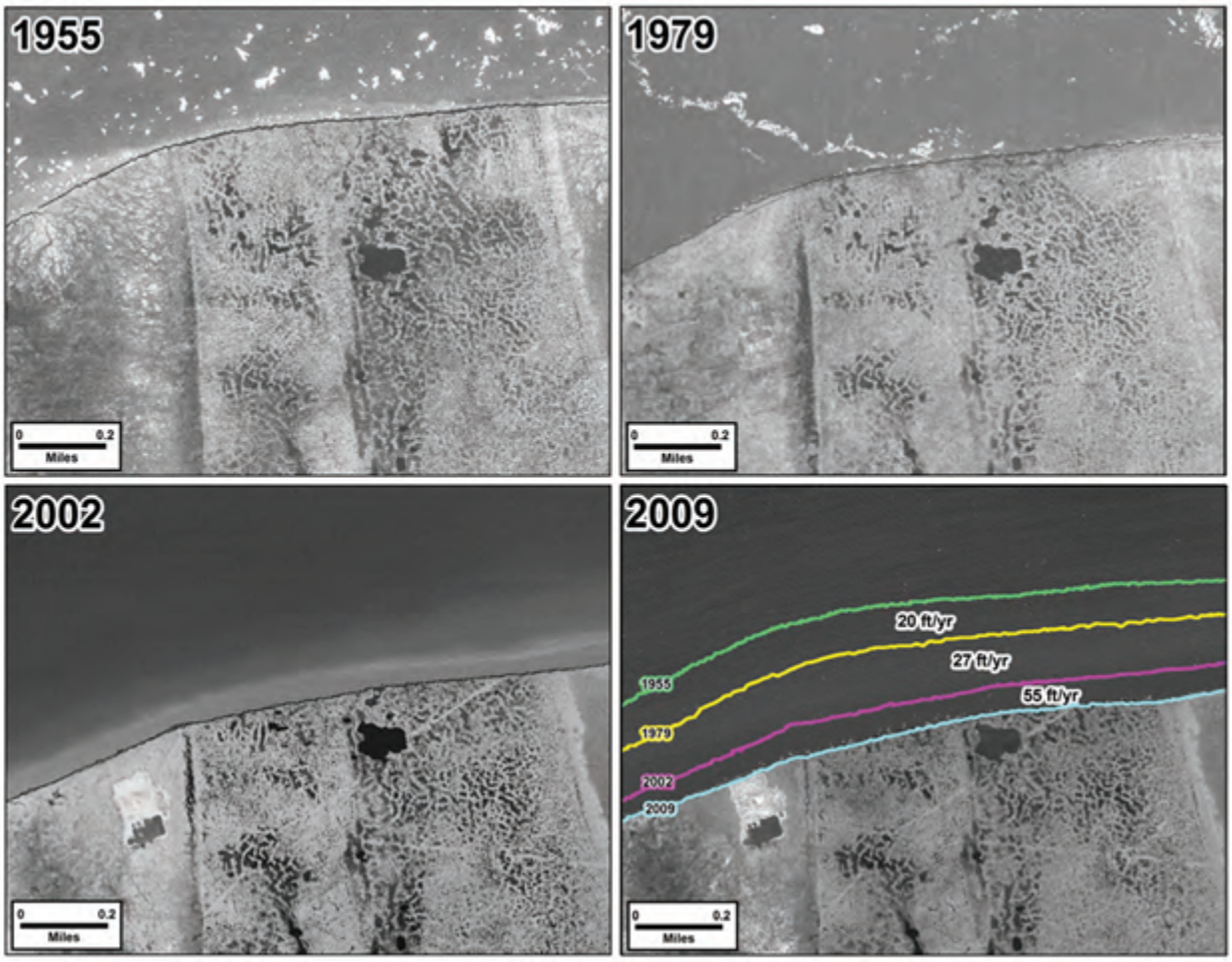

Figure 1.2. Aerial photography documenting increased rates of erosion near Drew Point, Alaska. Adapted from *Clement et al.* [2013]. Photo source: Benjamin M. Jones, U.S. Geological Survey.

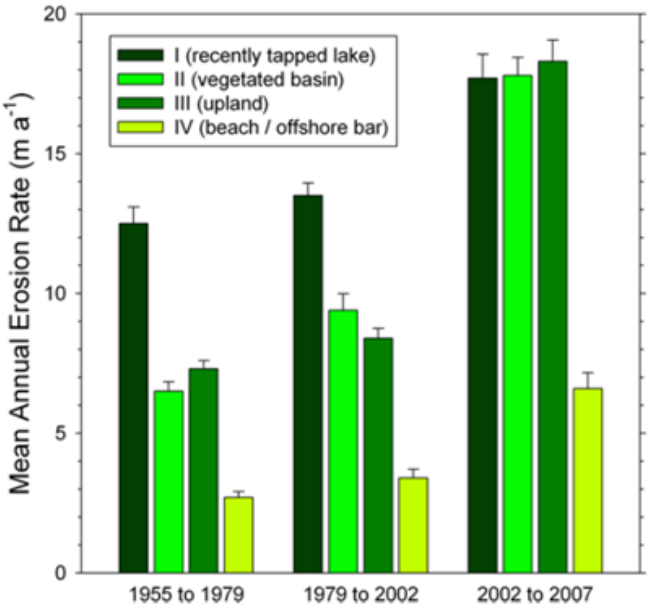

Figure 1.3. Plot showing an increase in the annual erosion rate for all geomorphic zones in the vicinity of Drew Point, Alaska. Adapted from *Jones et al.* [2009].

In summary, observation-based studies have demonstrated a significant increase in Arctic coastal erosion rates. These positive trends have been replicated and the time series extended by multiple investigators. Coastal erosion rates are increasing across highly-variable geomorphic conditions throughout the Arctic. The consistency in the positive trend is indicative of major a shift in coastal landscape evolution in the Arctic, likely fueled by changes in sea-ice extent, sea level rise, sea temperature, and permafrost state.

Existing Infrastructure in Jeopardy

Rapid Arctic coastal erosion stands to adversely impact native, scientific, industrial, and military communities in Alaska. Recent estimates suggest that 86 percent of the native villages in Alaska situated along rivers or coasts are now more frequently affected by floods or erosion [*Clement et al.*, 2013]. Homes have fallen into the sea (Figure 1.4). Archaeological sites and landfills have been compromised. In some cases, the dispersion or relocation of entire communities has been proposed. The social costs of such proposals are high. The North Slope of Alaska is also home to a large network of oil and gas infrastructure. Erosion conditions along the coast will likely impact the rate and cost of hydrocarbon extraction. Resource extraction necessitates frozen ground conditions to transport equipment and maintain infrastructure. Land-based development is needed to support offshore leases. Shoreline

fuel storage and delivery systems will be put at greater risk. The conditions at the coast, exacerbated by climate change, could increase the cost to design and build public and private infrastructure in the Arctic by 20 percent, a change of more than six billion dollars [*Clement et al.*, 2013].

Figure 1.4. Photograph of a building in Shishmaref, Alaska collapsed onto the beach. Adapted from *Sheppard* [2015].

The North Slope of Alaska is a base of research operations for Sandia National Laboratories (SNL) and the U.S. Department of Energy (DOE). As shown in Figure 1.5, there are also several active U.S. Department of Defense (DOD) sites on the Alaskan coast. Erosion may undermine the stability and function of these sites. Alaskan research facilities associated with the Atmospheric Radiation Program (ARM) are located in Barrow, Atqasuk, and Oliktok Point [*Ivey*, 2010]. The Barrow and Oliktok Point facilities are situated along one of the most rapidly eroding sections of coast in the world (Figure 1.6). Oliktok Point is also home to one of the 15 sites (a multi-billion dollar portfolio) dedicated to the U.S. Long Range Radar Program. The objective of the facility is to, in perpetuity, spot foreign aircraft heading into U.S. airspace. The network of radar sites maintains national sovereignty in the air. Severe coastal erosion problems in the vicinity of the Oliktok Point radar site have arrived two decades earlier than original projections. An airstrip, roads, and residential structures that support the radar equipment are at risk. It is thought that mitigation efforts must be completed within three years to maintain operations. Remediation projects on the North Slope, however, are extremely expensive due to the remote nature of the Arctic. Protecting

the runway at the Cape Lisburne Long Range Radar site from coastal erosion, for example, could cost 47 million dollars [*Hughes*, 2016].

Coastal erosion poses a threat to the social and cultural integrity of the Alaskan coast. It poses a significant threat to the existing infrastructure and, without an accurate predictive model, it also threatens future infrastructure development and relocation. Lastly, erosion can threaten the health and safety of local communities as well as the environment. Histories of disease, chemical warfare, and radiologic materials are buried and frozen around the Arctic coastline and, as it is eroded, new threats may be unleashed. The combination of these aspects necessitate a predictive model that can accurately account for erosion in the Arctic.

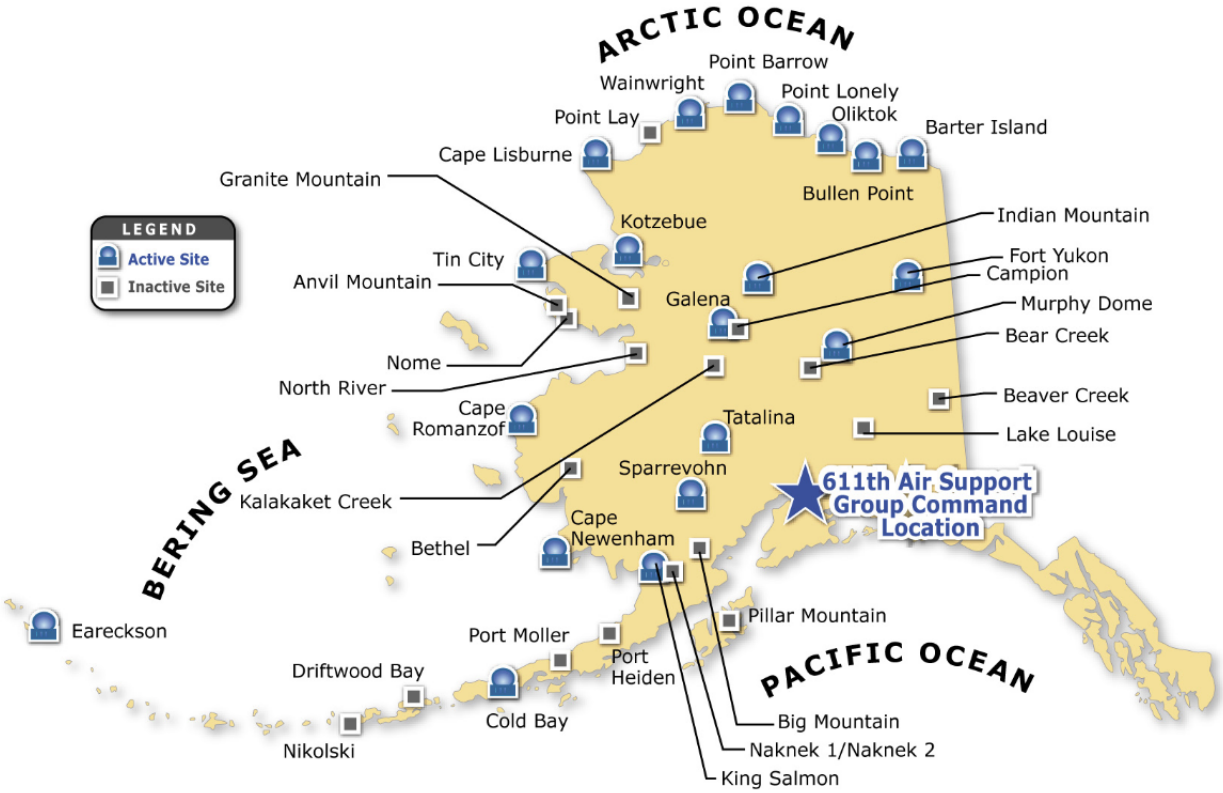

Figure 1.5. Locations of active and inactive Department of Defense sites in Alaska. Adapted from *DEC* [2016].

Figure 1.6. Aerial photographs showing the location of the U.S. Atmospheric Radiation Program facilities at Barrow (top) and Oliktok Point (bottom), Alaska. Adapted from *Ivey* [2010].

Chapter 2

Review of Arctic Coastal Erosion Studies: Observations and Trends

Alaskan Coastline

The Alaskan Arctic coast, bordered by the American Chukchi Sea and American Beaufort Sea, extends more than 8,000 km from the Bering Strait to the Canadian border (Figure 2.1). The coastal zone is typified by high-energy, low-frequency oceanographic forcings with low mean annual wave energy. Despite low mean annual wave energy, the coastline is dominated by erosional landforms. Field survey, aerial photography, and remote sensing products have been employed for observation-based Alaskan coastal erosion studies. In areas where barrier islands do not protect the mainland, the American Beaufort Sea coast exhibits the highest rates of erosion in the circum-Arctic [*Overduin et al.*, 2014].

Gorokhovich & Leiserowiz [2012] analyze the coastline along the Kotzebue Sound (part of the Northwest Arctic Borough shoreline) near the Bearing Strait on the American Chukchi Sea coast (Figure 2.2). The area includes bluffs comprised of glacial till fronted by sandy or gravelly beaches. Shallow slumps and mudflows are common erosional features (Figure 2.3). Individual storm events have caused up to 20 m of erosion in the vicinity of air strips and schools. *Gorokhovich & Leiserowiz* [2012] use aerial photographs dating from 1950-2003 to quantify coastal erosion rates. The long-term average erosion rate is 0.1 m yr^{-1}. Shorter term (1993-2006) retreat rates, for locations near the *Gorokhovich & Leiserowiz* [2012] study area, range from 0.1 to 2.0 m yr^{-1} [*Jordan et al.*, 2006]. Despite the historically low average erosion rates, the low-lying tundra, marshes, and tidal flats in the Kotzebue Sound are thought to be vulnerable to sea-level rise. In the next 50 years, *Gorokhovich & Leiserowiz* [2012] estimate average erosion rates may increase to 1.7 m yr^{-1}.

Northeast of the Kotzebue Sound, *Gibbs & Richmond* [2015] provide a comprehensive assessment of coastal erosion along the north slope of Alaska from Icy Cape to Demarcation Bay (Figure 2.4). The approximately 50-60 yr (i.e., circa 1940s to circa 2000s) average erosion rates were measured with aerial photography, satellite imagery, and Light Detecting and Ranging data for more than 26,000 transects at 50 m spacing. Across the entire study area, the long-term average erosion rate is 1.4 m yr^{-1}, with a maximum rate of 18.6 m yr^{-1}. *Gibbs & Richmond* [2015] find erosion rates along the Beaufort Sea coast (1.7 m yr^{-1})

Figure 2.1. Circum-Arctic coastal erosion rates, ground ice contents, and cliff heights. Adapted from *Overduin et al.* [2014].

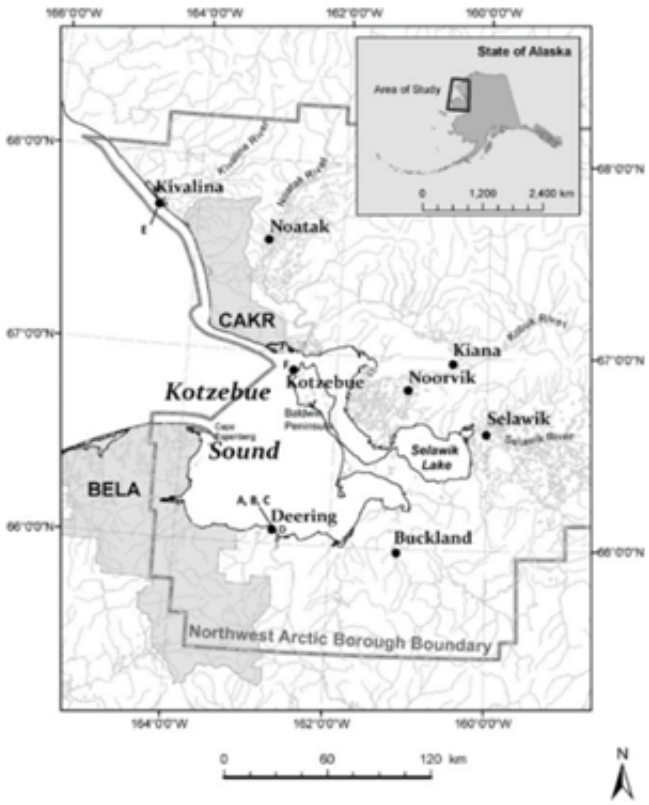

Figure 2.2. The coastline along the Kotzebue Sound is part of the Northwest Arctic Borough shoreline and is near the Bearing Strait on the American Chukchi Sea coast. Adapted from *Gorokhovich & Leiserowiz* [2012].

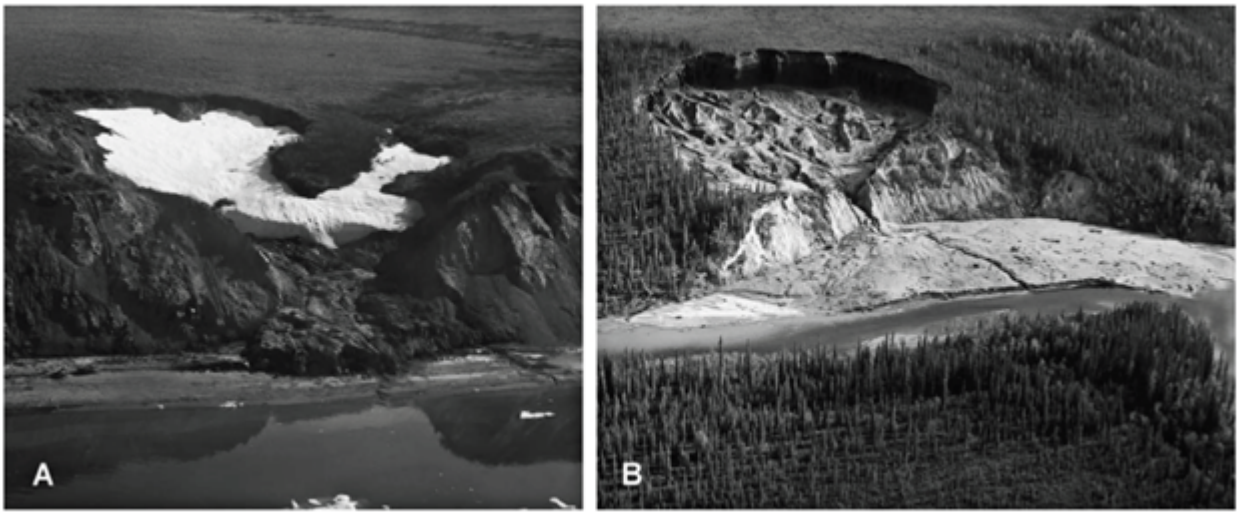

Figure 2.3. Photographs of slump and mudflow activity along the American Chukchi Sea coast near the Bering Strait. Adapted from *Gorokhovich & Leiserowiz* [2012].

are approximately six times greater than those along the Chukchi Sea coast (0.3 m yr^{-1}). Barrier islands and mainland areas exhibit similar average erosion rates (1.7 and 1.8 m yr^{-1}, respectively). Shoreline type and exposure appear to exert an important control on erosion rates (Figure 2.5). Exposed shorelines experience erosion rates twice as high as sheltered areas (1.8 and 0.9 m yr^{-1}, respectively).

Harper [1978] examines coastal erosion rates from Peard Bay to Barrow on the American Chukchi Sea coast (Figure 2.6). The 75 km of coastline is typified by 10 m high bluffs that consist of ice-bonded clays, silts, and sands. Aerial photographs from 1948-1976 reveal an average erosion rate of 0.3 m yr^{-1}. *Hume et al.* [1972] look at a smaller section of cliffs just southwest of Barrow and report an average retreat rate of 2.0 m yr^{-1} for a similar time period. The *Harper* [1978] average rate is much lower than those associated with the nearby Beaufort Sea coast (i.e., eastward from Barrow). *Harper* [1978] suggests the contrast may be linked to the coarse sediment, low ice content, and high cliffs typical of the Peard Bay-Barrow study area.

Erosion along the American Beaufort Sea coast, particularly between Drew Point and Cape Halkett, has received widespread attention. *Jorgenson & Brown* [2005] divide the approximately 2,000 km-long American Beaufort Sea coast (Barrow to the Canadian border; Figure 2.7) into 48 segments and five classes. The five classes include exposed bluffs (313 km), bays and inlets (235 km), lagoons with barrier islands (546 km), tapped basins (171 km), and deltas (691 km). *Jorgenson & Brown* [2005] compile erosion rates from the literature (1940s-2000s) and compute average erosion rates for the five classes. They find high erosion rates for steep and silty bluffs that lack beaches, intermediate rates for bluffs with a broad gravelly foreshore, and low rates for flat silty deltaic environments (Figure 2.8). With the exception

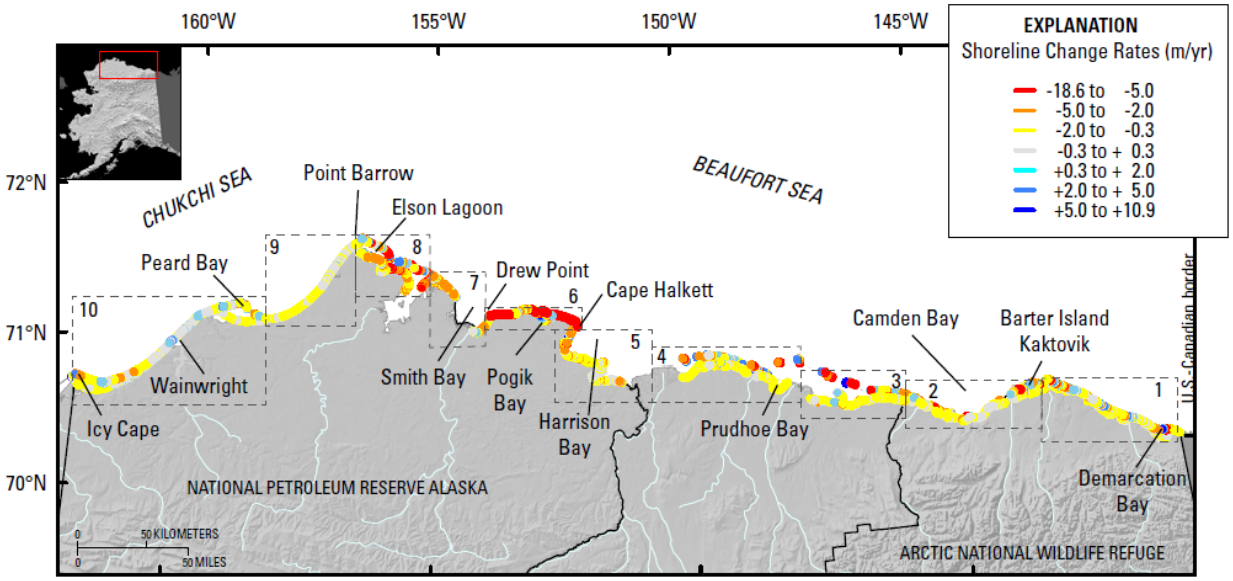

Figure 2.4. Erosion rates for the north coast of Alaska. Adapted from *Gibbs & Richmond* [2015].

of areas where deposition has occurred and erosion is zero (e.g., deltas), the lagoons have the lowest average erosion rate (0.7 m yr^{-1}). The exposed bluffs have the highest average erosion rate (2.4 m yr^{-1}).

To provide a spatially continuous (344 km-long) picture of erosion between Drew Point and Prudhoe Bay (Figure 2.9), *Reimnitz et al.* [1988] use U.S. Coast and Geodetic Survey and National Ocean Survey charts from 1950 and 1980, respectively. The long-term average retreat rate is 2.5 m yr^{-1}. Coastal sections comprised of fine-grained sediment appear to erode faster (5.4 m yr^{-1}) than areas comprised of coarse-grained sediment (1.4 m yr^{-1}). *Reimnitz et al.* [1988] point out that if one considers the short, approximately three-month window in which the bulk of erosion occurs along the Beaufort Sea coast, the retreat rates are eight times greater than those in the Gulf of Mexico.

The narrow 60 km strip of coast between Drew Point and Cape Halkett (Figure 2.10) has been the subject many observation-based Arctic coastal erosion studies. The 2-6 m high, fine-grained, ice-rich bluffs, with narrow or non-existent beaches, retreat rapidly because of the thermal-mechanical effects of the ocean undermining the base of the cliff (Figure 2.11). *Mars & Houseknecht* [2007] use 1955 aerial photographs and 1985/2005 infrared imagery to estimate changes in land area. They find erosion rates are greater for open-ocean shorelines than for partially-closed shorelines such as in bays and lagoons. Land loss increases from 0.5 to 1.1 km^2 yr^{-1} from the 1955-1985 period to the 1985-2005 period (Figure 2.12). Erosion is also seen breaching large freshwater lakes (Figure 2.13).

Jones et al. [2009] divide the Drew Point-Cape Halkett coastline into 100 m increments

Shoreline type	Number of transects	Average of rates (m/yr)	Maximum rate (m/yr)		Percent of transects		Percent of study area
			Erosion	Accretion	Eroding	Accreting	
Study Area: U.S.-Canadian border to Icy Cape							
All transects	26,567	-1.4	-18.6	10.9	84	16	100
Beaufort Sea coast	19,222	-1.7	-18.6	10.9	88	12	72
Chukchi Sea coast	7,345	-0.3	-8.5	8.0	74	25	28
All sheltered shorelines	11,199	-0.9	-16.4	10.9	88	11	42
All exposed shorelines	15,368	-1.8	-18.6	9.6	81	19	58
All mainland shorelines	18677	-1.2	-18.6	10.9	12	88	70
Only exposed mainland	7,478	-1.8	-18.6	7.3	87	12	28
Only exposed barriers (island, spit, beach)	7,725	-1.7	-17.9	9.6	75	25	29
Only exposed islands	165	-1.0	-2.6	0.9	92	8	0
Region 1: U.S.-Canadian border to Jago River							
All Transects	3,673	-1.0	-13.5	5.5	86	14	14
Sheltered shorelines	1,705	-0.5	-3.0	1.7	90	9	6
Exposed shorelines	1,968	-1.4	-13.5	5.5	82	18	7
Region 2: Jago River to Staines River							
All Transects	3,464	-1.1	-16.5	9.6	84	15	13
Sheltered shorelines	1,749	-0.5	-4.5	1.9	85	14	7
Exposed shorelines	1,715	-1.6	-16.5	9.6	83	17	6
Region 3: Staines River to Sagavanirktok River							
All transects	2,162	-1.5	-16.8	6.7	89	11	8
Sheltered shorelines	1,439	-0.8	-4.4	2.7	93	6	5
Exposed shorelines	723	-3.0	-16.8	6.7	81	19	3
Region 4: Sagavanirktok River to Colville River							
All transects	2,973	-1.1	-14.7	7.0	85	15	11
Sheltered shorelines	1,918	-0.8	-4.2	1.2	95	5	7
Exposed shorelines	1,055	-1.6	-14.7	7.0	66	34	4
Region 5: Colville River to Cape Halkett							
All transects (all exposed)	1,989	-1.1	-9.6	5.0	92	8	7
Region 6: Cape Halkett to Drew Point							
All transects	1,545	-6.3	-18.6	10.9	90	10	6
Sheltered shorelines	202	-0.5	-5.7	10.9	62	38	1
Exposed shorelines	1,343	-7.1	-18.6	7.3	94	6	5
Region 7: Drew Point to Dease Inlet							
All transects	1,315	-2.4	-16.4	3.4	92	8	5
Sheltered shorelines	457	-3.2	-16.4	0.6	96	4	2
Exposed shorelines	858	-1.9	-6.8	3.4	90	10	3
Region 8: Dease Inlet to Barrow							
All transects	2,228	-2.5	-17.9	7.0	90	10	8
Sheltered shorelines	1,406	-2.1	-9.9	4.9	95	5	5
Exposed shorelines	822	-3.2	-17.9	7.0	82	18	3
Region 9: Barrow to Peard Bay							
All transects (all exposed)	1,779	-0.3	-1.2	0.7	86	14	7
Region 10: Peard Bay to Icy Cape							
All transects	5,439	-0.3	-8.5	8.0	71	29	20
Sheltered shorelines	2,323	-0.3	-2.2	2.0	77	23	9
Exposed shorelines	3,116	-0.4	-8.5	8.0	66	33	12

Figure 2.5. Summary of erosion rates along the Beaufort and Chukchi Sea coast, organized by region and shoreline type. Adapted from *Gibbs & Richmond* [2015].

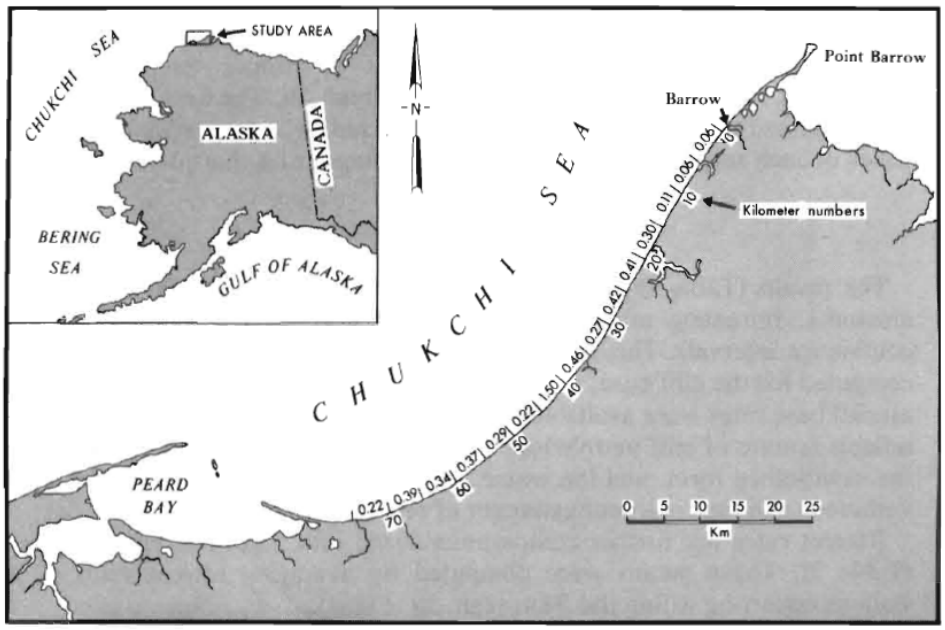

Figure 2.6. Study area from *Harper* [1978]. Erosion rates for each section are reported in m yr^{-1}.

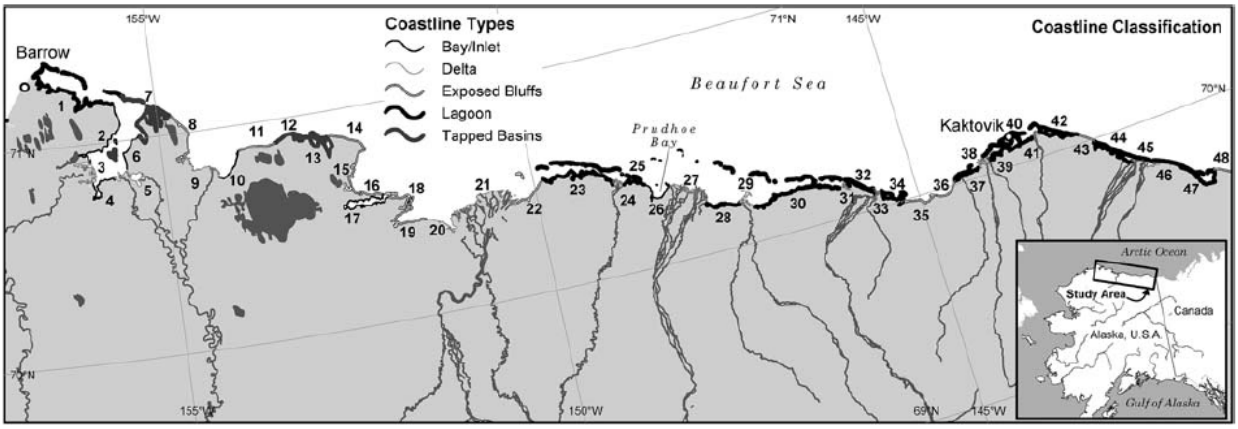

Figure 2.7. The Alaskan Beaufort Sea coast, showing the study area from *Jorgenson & Brown* [2005].

Figure 2.8. Photographs of coastal archetypes on the American Beaufort Sea coast. High, intermediate, and low coastal erosion rates were observed for locations similar to the top, middle, and bottom photographs. Adapted from *Jorgenson & Brown* [2005].

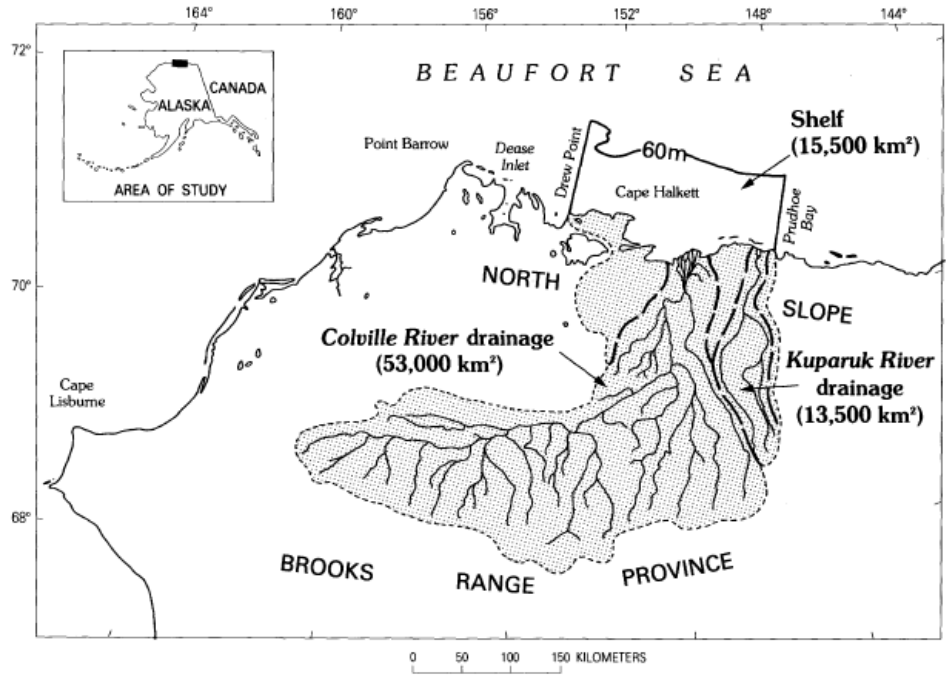

Figure 2.9. The Alaskan Beaufort Sea coast and the Colville River drainage area, showing the study area from *Reimnitz et al.* [1988].

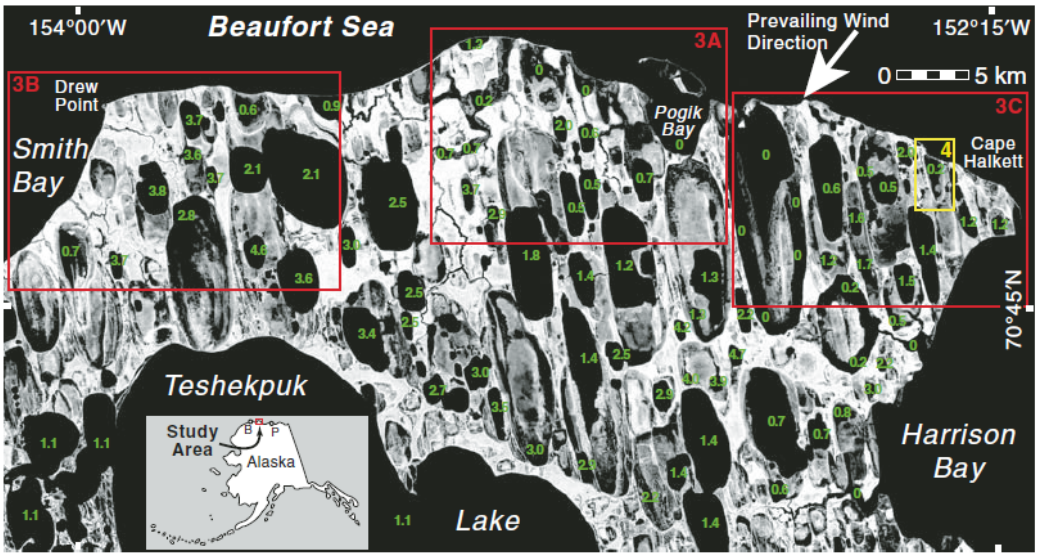

Figure 2.10. The central Alaskan Beaufort Sea coast, showing the study area from *Mars & Houseknecht* [2007]. Green numbers on lakes indicate lake elevation in meters.

Figure 2.11. Photograph of thermo-abrasion driving coastal erosion along the Alaskan Beaufort Sea coast near Drew Point. Adapted from *Mars & Houseknecht* [2007].

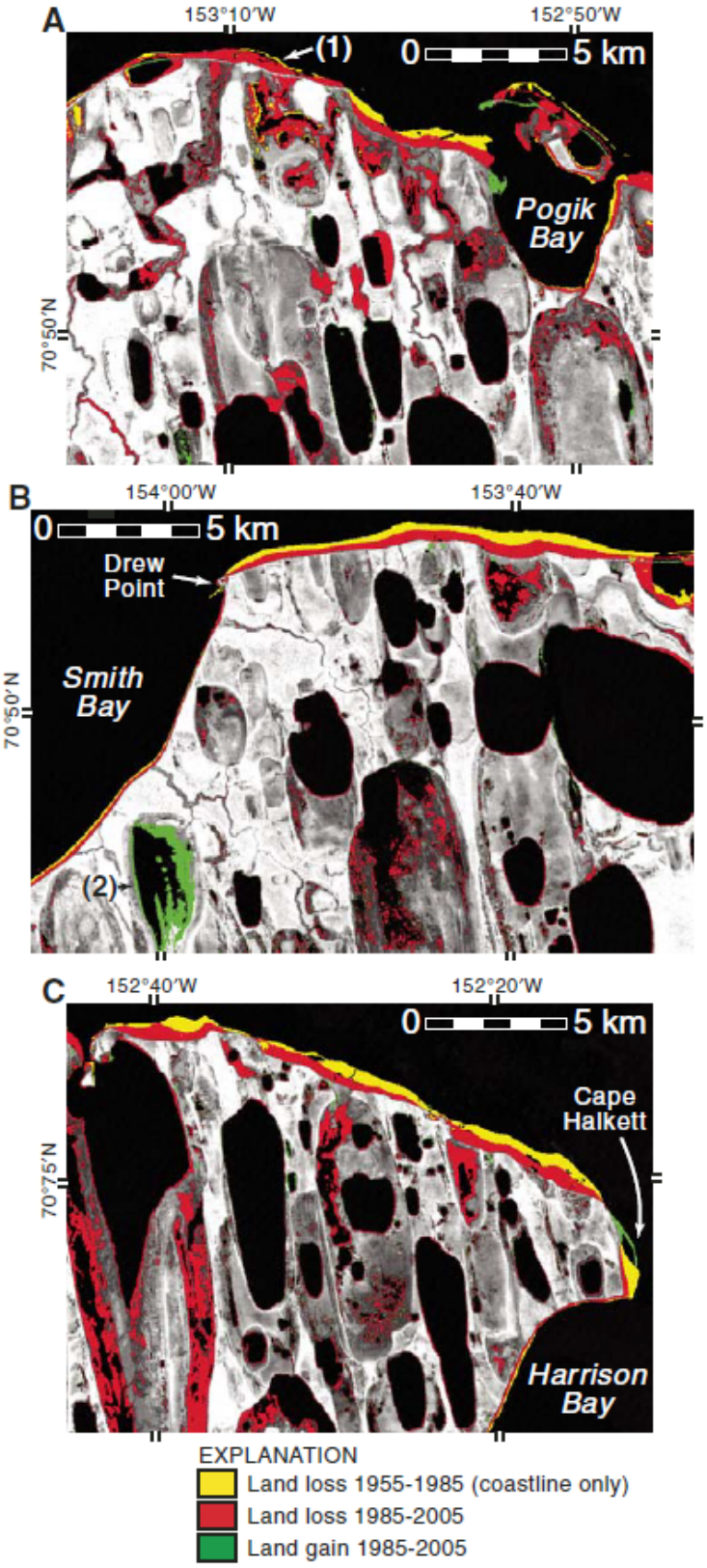

Figure 2.12. Infrared imagery with changes in land area between Drew Point and Cape Halkett. Adapted from *Mars & Houseknecht* [2007].

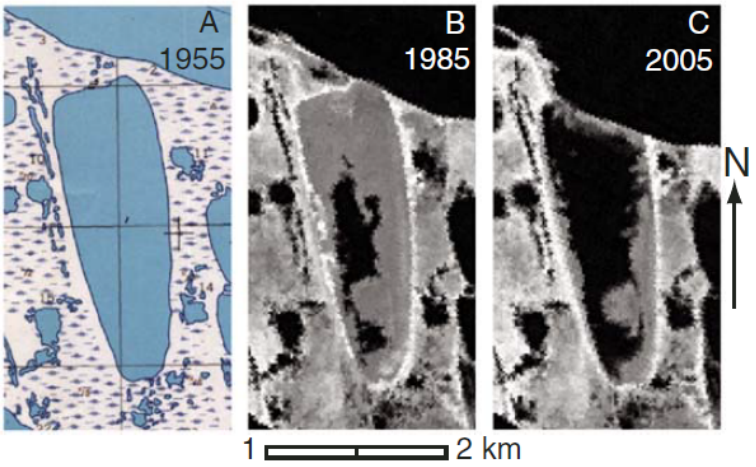

Figure 2.13. Infrared imagery showing coastal erosion breaching a freshwater lake between Drew Point and Cape Halkett. Adapted from *Mars & Houseknecht* [2007].

and four classes (i.e., recently breached lake, vegetated basin, upland, and beach/upshore bar). The study uses aerial imagery to calculate erosion rates for 1955-1979, 1979-2002, and 2002-2007. The average erosion rates for the three periods increase as 6.8, 8.7, and 13.6 m yr^{-1}. The youngest land surfaces, such as recently tapped lakes, which lack a vegetative mat, appear to be the most susceptible to erosion. *Arp et al.* [2010] build upon *Jones et al.* [2009] by using aerial photographs and satellite imagery for the same three time periods as well as from 2007-2009. The average erosion rates for the four periods increase as 6.0, 8.3, and 13.9, and 17.3 m yr^{-1}. *Arp et al.* [2010] confirm an increase in Drew Point-Cape Halkett erosion rates through time.

Observation-based studies that have focused on erosion in the Alaskan Arctic encompass a wide variety of spatial and temporal scales. Many geologic/geomorphic classification schemes have been employed. The highly-variable resolution of coastal position data as well as the site-specific nature of erosion can make comparison between studies difficult. It is not uncommon for minimum and maximum rates of erosion to differ from the average by an order of magnitude. Despite these challenges, the collective efforts of researchers lead to a fairly consistent conclusion: erosion rates in the Alaskan Arctic are among the highest in the world and they are accelerating.

Canada's Mainland Coastline

The Canadian Arctic coastline is vast, stretching from the U.S. border at the Beaufort Sea, all the way east to the North Atlantic (Figure 2.1). The majority of the Canadian coastline is rocky and lithified along the Arctic Archipelago islands, such as Baffin, Victoria,

or Ellesmere Islands. Erosion studies on these rocky lithified coasts are very rare. However, along mainland coastline of Canada, several studies show high rates of erosion. The mainland coast is predominantly unlithified, and consists of unconsolidated sediments.

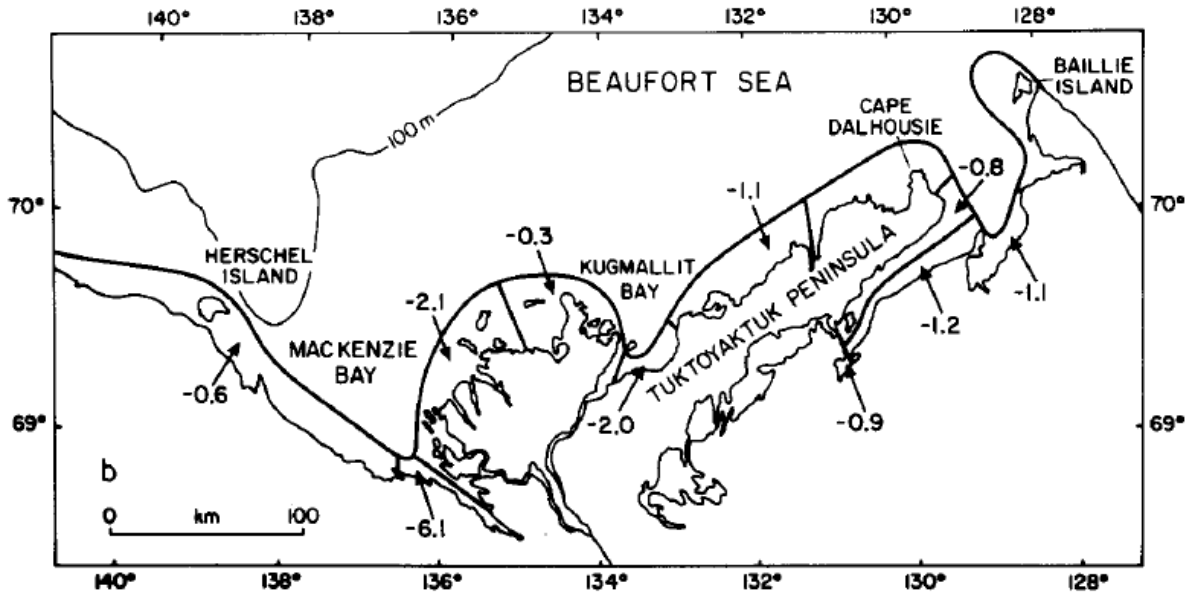

Figure 2.14. Average coastal retreat rates in m yr^{-1} along the Canadian Beaufort Sea. Adapted from *Harper* [1990].

Hequette & Barnes [1990] used stake observations and aerial photography to assess coastal retreat along the mainland Canadian Beaufort Sea coast, but measurements were made over a variable timespan (1970s to 1980s). Retreat rates varied between 0-6 m yr^{-1}. A more comprehensive review study by *Harper* [1990] reported that the entire Canadian Beaufort Sea coast is undergoing widespread retreat with point measurements in excess of 18 m yr^{-1}. The fastest average retreat rates were measured along the Mackenzie Delta, averaging between 2.1 and 6.1 m yr^{-1}. Figure 2.14 shows a map of the average coastal retreat rates compiled by *Harper* [1990].

Solomon [2005] reports that coastal changes from 1972 to 2000 are dominated by the retreat of the shoreline, with average annual retreat rates of 0.6 m yr^{-1}, but ranging as high as 22.5 m yr^{-1}. The table in Figure 2.15 shows a comprehensive compilation of retreat rates in the study by *Solomon* [2005]. The erosion rates shown in the table were obtained by the analysis of aerial photographs from 1972, 1985 and 2000.

Radosavljevic et al. [2016] investigated shoreline dynamics for the eastern tip of Herschel Island, with a focus on the gravelly spit, Simpson Point. Herschel Island is a UNESCO World Heritage candidate site, with a historic whaling settlement, as well as many native archeological sites. It is an ice push moraine, formed during the Wisconsin Glaciation, and consists of perennially frozen marine and glacigenic sediments, characterized by rolling topography with a maximum elevation of 183 m asl [*Lantuit & Pollard*, 2008]. Shoreline

Zone	N	Mean	Minimum	Maximum	Median	Standard deviation	Standard error
All 1972–2000	2697	−0.94	−15.33	3.84	−0.51	1.53	0.03
All 1972–1985	2697	−1.02	−16.86	7.31	−0.68	1.92	0.04
All 1985–2000	2697	−0.87	−22.50	6.57	−0.47	1.86	0.04
Outer Delta 1972–2000	717	−1.77	−10.67	2.66	−1.27	1.82	0.07
Outer Delta 1972–1985	717	−1.77	−16.86	5.48	−1.21	2.29	0.09
Outer Delta 1985–2000	717	−1.77	−11.75	6.57	−1.34	1.99	0.07
East Richards Island 1972–2000	571	−0.40	−4.65	1.95	−0.28	0.62	0.03
East Richards Island 1972–1985	571	−0.58	−6.24	3.19	−0.47	1.08	0.05
East Richards Island 1985–2000	571	−0.25	−5.09	4.84	−0.24	0.87	0.04
Outer Islands 1972–2000	196	−1.51	−15.33	2.86	−0.91	2.79	0.20
Outer Islands 1972–1985	196	−1.29	−11.58	5.29	−0.93	2.20	0.16
Outer Islands 1985–2000	196	−1.70	−22.50	5.59	−0.74	3.95	0.28
West Richards Island 1972–2000	251	−0.46	−4.99	1.05	−0.30	0.79	0.05
West Richards Island 1972–1985	251	−0.60	−7.58	4.65	−0.49	1.35	0.09
West Richards Island 1985–2000	251	−0.34	−6.48	2.97	−0.22	1.19	0.08
Tuktoyaktuk Peninsula 1972–2000	466	−0.75	−6.84	2.04	−0.44	1.28	0.06
Tuktoyaktuk Peninsula 1972–1985	466	−0.84	−10.95	4.68	−0.51	2.00	0.09
Tuktoyaktuk Peninsula 1985–2000	466	−0.67	−9.00	4.44	−0.34	1.48	0.07

Figure 2.15. Coastal statistics for Canadian Beaufort Sea coast study sites compiled by *Solomon* [2005].

retreat was assessed based on aerial photographs for the periods 1952-1970, 1970-2000, and 2000-2011. Widespread shoreline retreat was observed, with a mean rate of 0.6 m yr^{-1} in 1952-1970, 0.5 m yr^{-1} in 1970-2000, and 1.3 m yr^{-1} in 2000-2011, nearly tripling in the last decade of study.

Siberian Coastline and Other Coasts

Across the Arctic from the Canadian and American shorelines, bordered by the Eastern Siberian Sea, Laptev Sea, Kara Sea, Barents Sea, and Greenland Sea, lies more than 83,000 km of coastline (Figure 2.1). By some estimates, fewer than 4% of these coastlines have been studied closely [*Overduin et al.*, 2014]. Similar to efforts in Alaska and Canada, field surveys, aerial photography, and remote sensing products have been employed for observation-based erosion studies.

Northwest of the Chukchi Sea coast are the Eastern Siberian Sea coast and Laptev Sea coast (Figure 2.1). These two areas have been noted for their similar geomorphologies *Overduin et al.* [2014]. The Laptev Sea coast is characterized by 10-40 m tall very ice-rich bluffs with ice wedges up to 50 m deep and 8 m wide. Roughly 22% of the coast is rocky. Where the bluffs consist of unconsolidated material, the failure mode is similar to the American Beaufort Sea coast (i.e., thermal-mechanical undermining). The Arctic Coastal Dynamics Project reports a weighted mean coastal erosion rate of 0.7 m yr^{-1} for the Laptev Sea coast [*Lantuit et al.*, 2011]. *Günther et al.* [2013] calculates erosion rates for three sites in the Laptev Sea (Figure 2.16) using satellite imagery from 1965-2011 and classify erosion as either thermo-denudation (TD; the combined influences of solar insolation, and heat transfer,

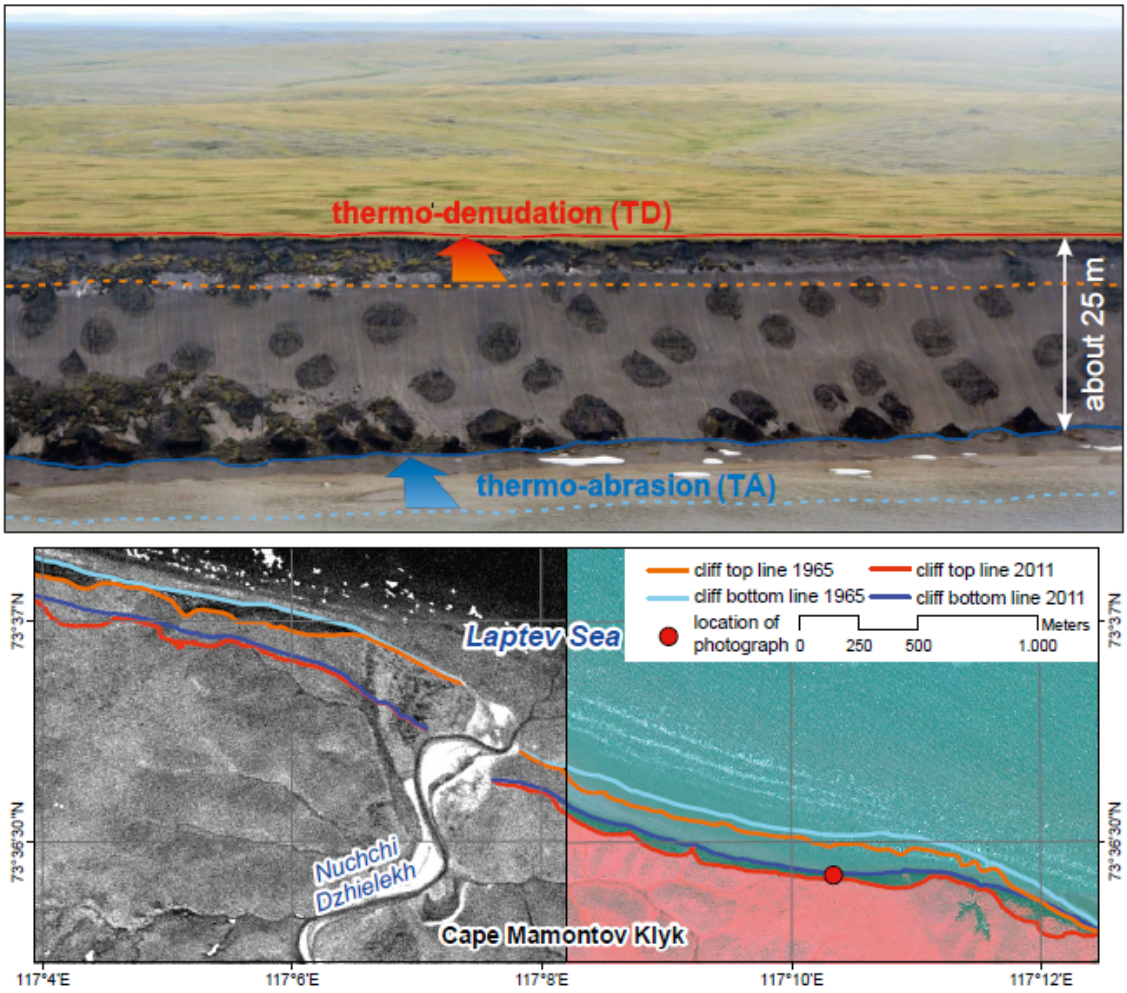

Figure 2.16. Study area from *Günther et al.* [2013], including an illustration of subaerial (i.e., thermo-denudation) and submarine (i.e., thermo-abrasion) processes. The coastline is characterized by massive ice complex deposits.

above the water line) or thermo-abrasion (TA; the combined mechanical and thermal effects of impinging wave energy at the shoreline). The measurements (Figure 2.17) indicate the most recent 2-yr erosion rates (5.3 m yr^{-1}) are roughly two-times faster than the 42-yr average (2.2 m yr^{-1}). At Mamontov Klyk, Laptev Sea, Siberia, mean long term TA and TD are both 2.1 m yr^{-1}, with a nearly consistent range between 0.5 and 3.5 m yr^{-1}. West of the Buor Khaya Peninsula, Laptevarchip Sea, Siberia, long term TD is 0.6 m yr^{-1}, and TA is 0.5 m yr^{-1}. The fastest erosion rates among the three locations occurred at Oyogos Yar, Laptev Sea, Siberia, with mean long term TD and TA rates of 3.4 and 3.2 m yr^{-1}, respectively. Across the entire study area, *Günther et al.* [2013] report that recent erosion rates were at least 1.6 times higher than the long term mean, with a total variability between

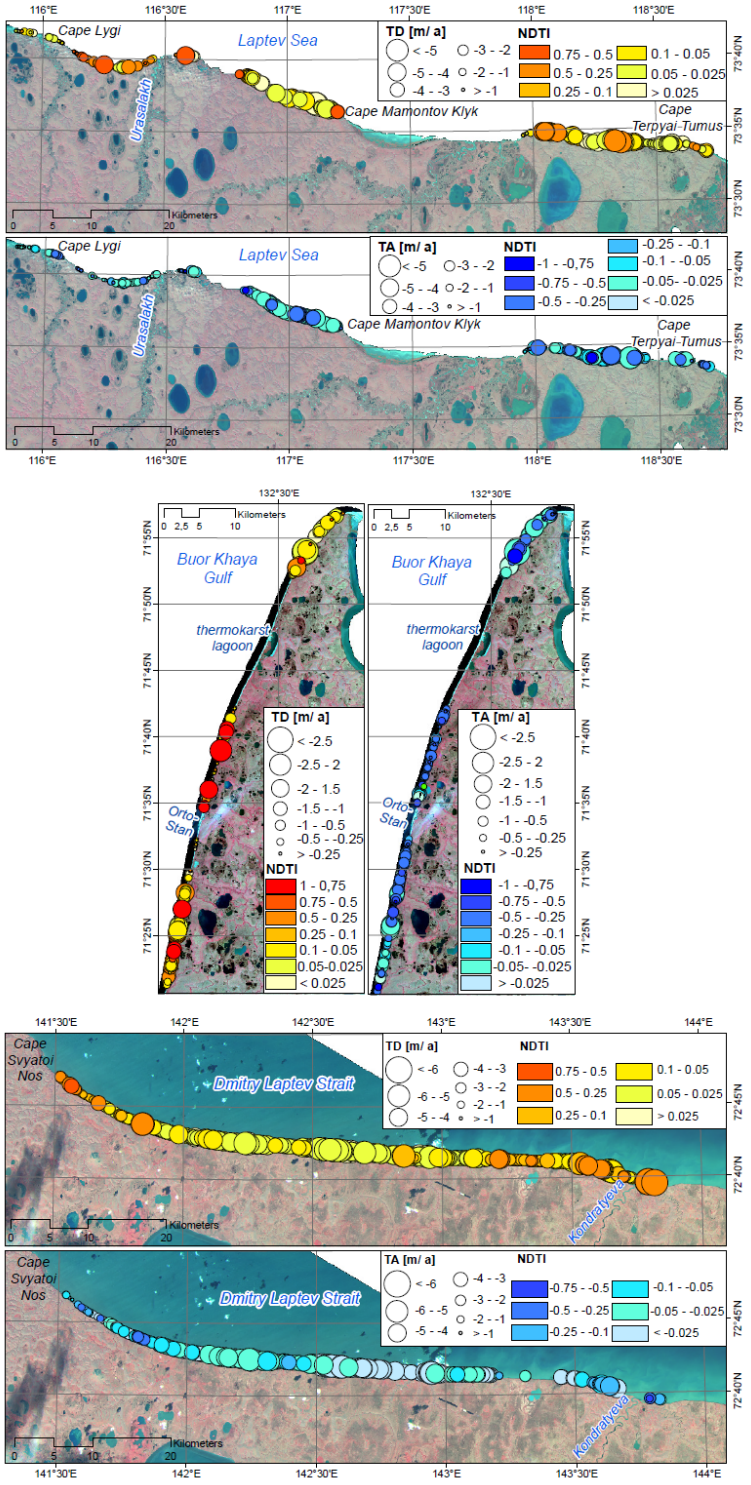

Figure 2.17. Coastal erosion transect data for the Laptev Sea, showing erosion rates split by thermo-denudation (TD) and thermo-abrasion (TA) processes. Adapted from *Günther et al.* [2013].

0 and 21 m yr^{-1}. *Lantuit et al.* [2011] focus on a single 150 km long peninsula that shelters a harbor in the Laptev Sea. The landscape is dominated by retrogressive thaw slumps. Aerial photographs and satellite imagery dating from 1951-2006 (Figure 2.18) suggest a long-term average erosion rate of 0.6 m yr^{-1}. *Lantuit et al.* [2011] find no significant temporal trend in erosion for the study period, but highlight strong interdecadal variability.

For all Siberian yedoma ice complex coastlines, *Grigoriev* [2008] reports a mean erosion rate of 1.9 m yr^{-1}. For key study sites along the Laptev Sea, *Grigoriev et al.* [2009] report erosion rates of up to 25 m yr^{-1}, with the highest rates occurring since 1985. *Vasiliev et al.* [2006] find annual rates of erosion between 0.8 to 2 m yr^{-1} at Marre Sale, Yamal Peninsula, Siberia. *Pizhankova & Dobrynina* [2010] report erosion rates from Bolshoy Lyakhovsky Island between 3.2 and 5.3 m yr^{-1}. Figure 2.19 provides a set of graphs illustrating coastline retreat rates between 1950 and 2010 for several Siberian sites.

Vasiliev et al. [2005] investigate coastal erosion for four sites on the Barents Sea coast and Kara Sea coast (Figure 2.20) using aerial photographs and ground survey. The 15-30 m high, ice-rich, clay- and sand-dominated permafrost bluffs on the Kara Sea coast have average erosion rates of 1.7 m yr^{-1} and 1.1 m yr^{-1} for 1978-2003 and 1999-2002, respectively. The 5-50 m high, less ice-rich, clay-, loamy- and sand-dominated permafrost bluffs on the Barents Sea coast have average erosion rates of < 0.1 m yr^{-1} and 2.0 m yr^{-1} for 1999-2003 and $\sim$1948-2002, respectively. Using aerial photographs and satellite imagery, *Guégan* [2015] calculates erosion rates for a 90 km section of the Barents Sea coast (Figure 2.21). The first two sites experience erosion in a fashion more typical of temperate coasts (i.e., dominated by the effects of wind and waves rather than thermal energy). The three long-term average erosion rates (1961-2012) follow as 2.0, 1.8, and 2.3 m yr^{-1}. The third site, with 5-15 m high, ice-rich permafrost bluffs of various sediment type, shows retreat increasing as 0.6 (1961-1968), 2.8 (1990-1998), and 4.8 m yr^{-1} (1998-2010).

The archipelagos of the high Arctic include Svalbard, Novaya, Zemlya, Franz Joseph Land, the Canadian Arctic, and Greenland. Owing to the challenging weather conditions, prolonged sea-ice cover, and protracted periods of darkness, considerably less coastal erosion research has been conducted in these areas [*Overduin et al.*, 2014]. The influence of glacial activity (past and present) is strong and the coasts tend to be comprised of relatively coarse sediments, sometimes underlain by bedrock. In general, coastal erosion along lithified coasts of the high Arctic Archipelagos is dominated by frost weathering, involving freeze-thaw-dry-wet cycling that is most intense at the coastline, and decreases inland. *Overduin et al.* [2014] provides a review of some existing studies. Erosion rates tend to be at least an order of magnitude lower along lithified coasts. For example, rates of 0.025 to 0.05 m yr^{-1} have been observed at Spitsbergen, Svalbard. In fjords and straits, landslide-induced tsunami waves can wash large volumes of sediment into the sea, but their recurrence intervals are low (500-1000 years in Greenland). *Guégan & Christiansen* [2016] use aerial imagery and detect virtually no erosion at a site in Svalbard (Figure 2.22) from 1971-2008, with an increase to 0.6 m yr^{-1} between 2008 and 2011. Time-lapse photography taken in 2012 and 2013 reveals average erosion rates of $\sim$0.8 and 0.4 m yr^{-1}, respectively. *Guégan & Christiansen* [2016] point out, however, that the majority of the erosion in 2012 and 2013 occurs in a single

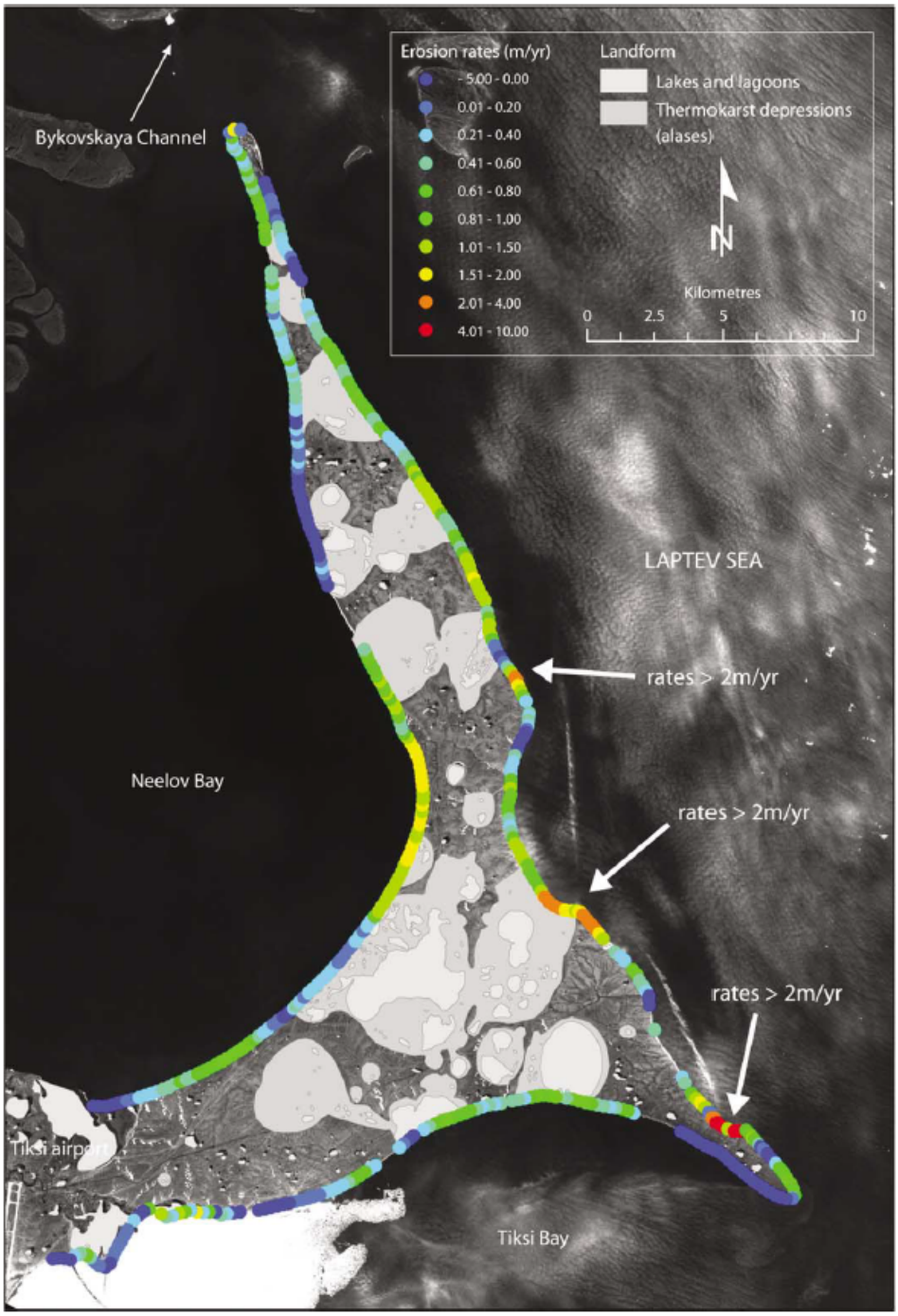

Figure 2.18. Erosion measurements made on the Bykovsky Peninsula in the Laptev Sea, Siberia. Adapted from *Lantuit et al.* [2011].

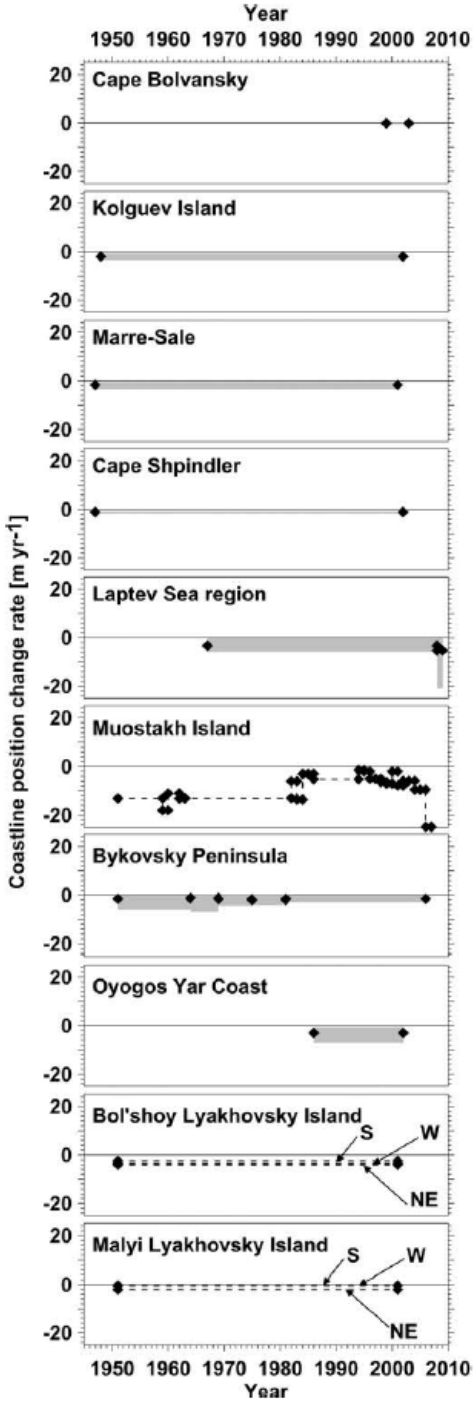

Figure 2.19. Erosion rates at Siberian study sites. Adapted from *Overduin et al.* [2014].

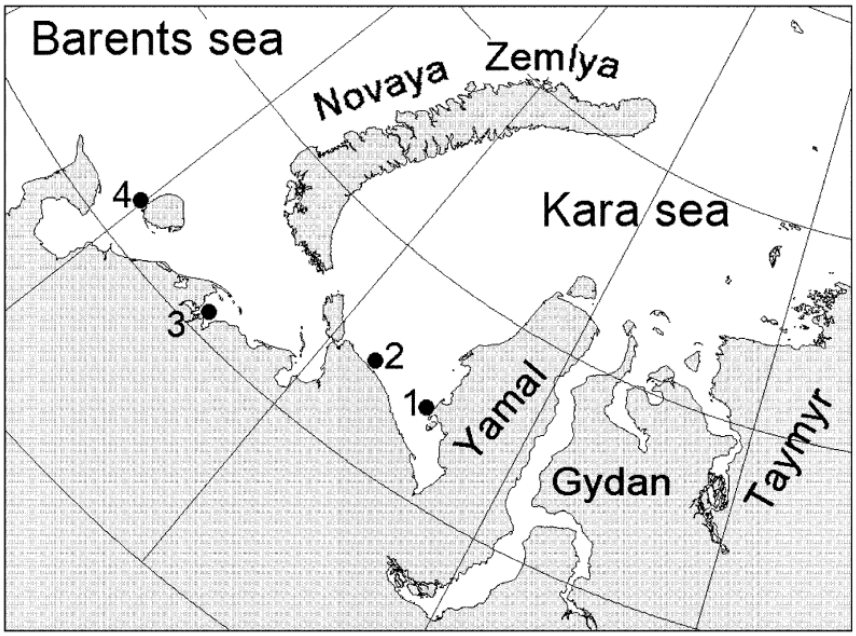

Figure 2.20. Study area from *Vasiliev et al.* [2005]. Four coastal sites along the Barents and Kara Sea, Siberia.

month.

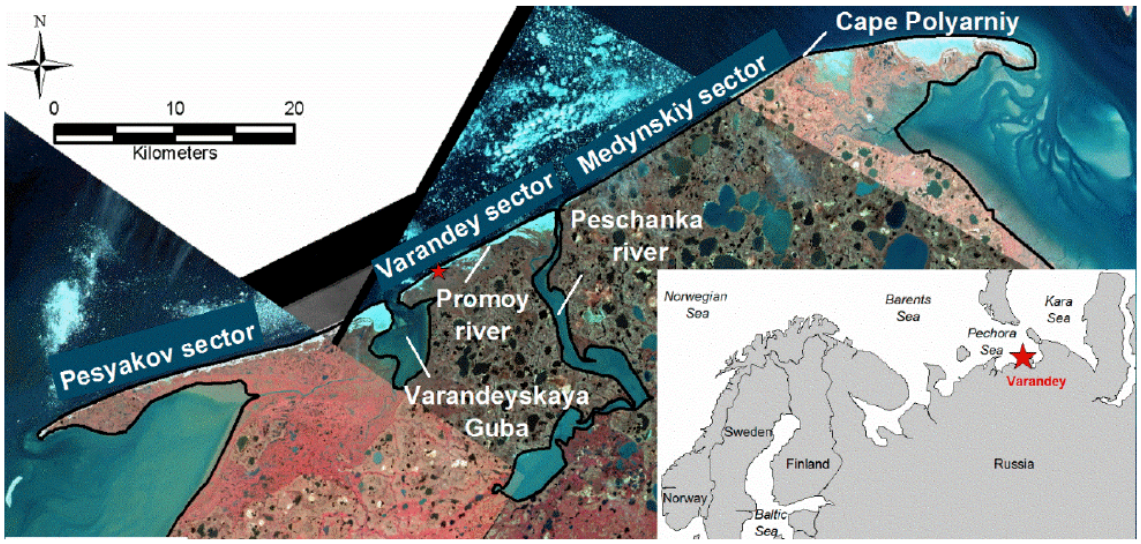

Figure 2.21. Study area from *Guégan* [2015] along the Barents Sea, Siberia.

The Arctic coastline bordering the Eastern Siberian Sea, Laptev Sea, Kara Sea, Barents Sea, and Greenland Sea is vast. Erosion rates based on routine observation encompass a small fraction of the region. Although some coastal areas are fronted by bedrock and exhibit slow erosion rates, many of the sections fronted by unconsolidated ice-bonded sediment are eroding at rates comparable to the Beaufort and Chukchi Sea coast.

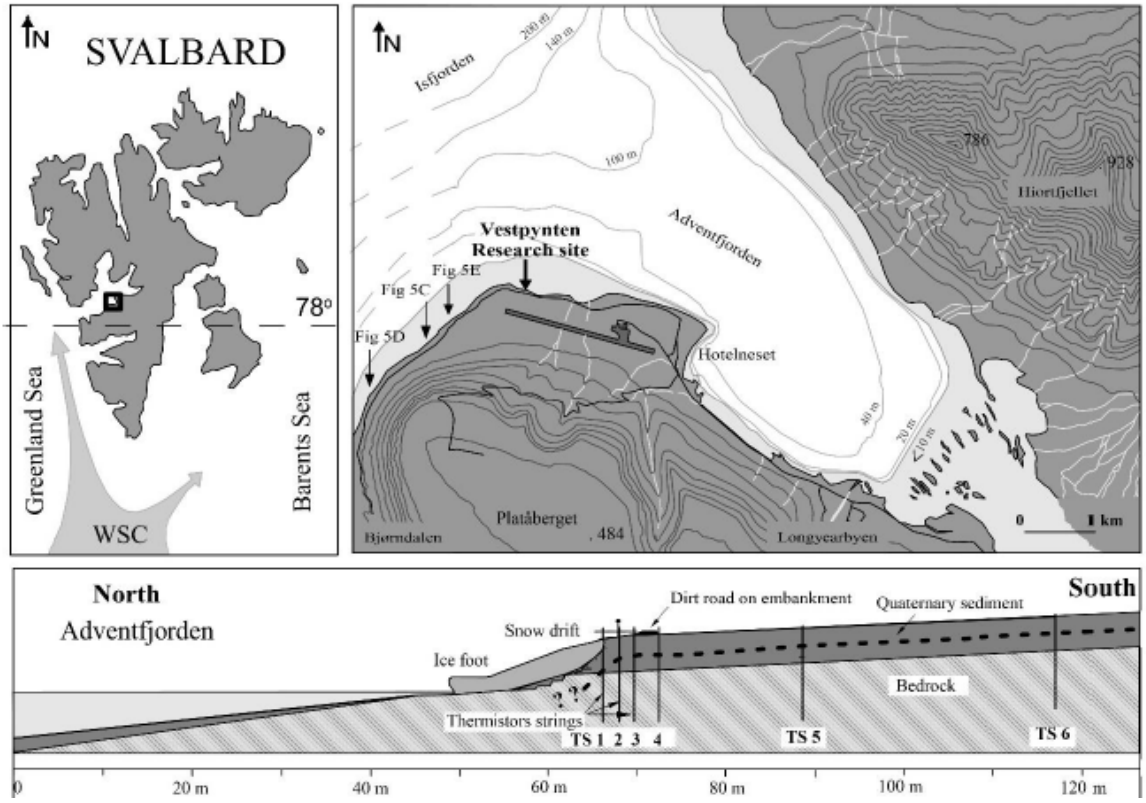

Figure 2.22. Study area from *Guégan* [2015] at Svalbard, with a cross section schematic of the study site along Adventfjorden.

Table 1 List of recently published studies with rates of erosion (or aggradation) for permafrost coasts.

Study location	Mean annual erosion rate (m a^{-1})	Period	Length of coastline studied (km)	Reference
Alaska				
Barrow, Alaska	-2.5	2003-2006	11	Aguirre *et al.* (2008)
Barrow, Alaska	-1.7	2006-2007	11	Aguirre *et al.* (2008)
Barrow, Alaska	-2.0	2007-2008	11	Tweedie *et al.* (2012)
Barrow, Alaska	-0.9	2008-2009	11	Tweedie *et al.* (2012)
Barrow, Alaska	-2.2	2009-2010	11	Tweedie *et al.* (2012)
Barrow, Alaska	-1.4	2010-2011	11	Tweedie *et al.* (2012)
Teshekpuk Lake Special Area	-5.0	1955-1979	100	Jones *et al.* (2008)
Teshekpuk Lake Special Area	-6.2	1979-2002	100	Jones *et al.* (2008)
Drew Point	-6.8	1955-1979	60	Jones *et al.* (2009a)
Drew Point	-8.7	1979-2002	60	Jones *et al.* (2009a)
Drew Point	-13.6	2002-2007	60	Jones *et al.* (2009a)
Cape Halkett	-6.2	1955-1966	12	Jones *et al.* (2009b)
Cape Halkett	-5.7	1966-1976	12	Jones *et al.* (2009b)
Cape Halkett	-7.5	1976-1979	12	Jones *et al.* (2009b)
Cape Halkett	-7.5	1979-2002	12	Jones *et al.* (2009b)
Cape Halkett	-8.5	2002-2007	12	Jones *et al.* (2009b)
Cape Halkett	-13.8	2007-2009	12	Jones *et al.* (2009b)
Drew Point	-17.0	2007-2009	60	Arp *et al.* (2010)
Alaskan Beaufort Sea coast	-0.6	1950-1980	1957*	Ping *et al.* (2011)
Alaskan Beaufort Sea coast	-1.2	1980-2000	1957*	Ping *et al.* (2011)
Alaskan Beaufort Sea coast	-2.0	1947-2000s	*ca.* 1900	Gibbs *et al.* (2011)
Kotzebue Sound north	-0.2	1950s-1980s	153	Gorokhovich and Leiserowiz (2012)
Kotzebue Sound north	**0.1**	1980s-2003	153	Gorokhovich and Leiserowiz (2012)
Kotzebue Sound south	-0.2	1950s-1980s	147	Gorokhovich and Leiserowiz (2012)
Kotzebue Sound south	0.0	1980s-2003	147	Gorokhovich and Leiserowiz (2012)
Canada				
Mackenzie Delta	-1.0	1972-1985	> 2000	Solomon (2005)
Mackenzie Delta	-0.9	1985-2000	> 2000	Solomon (2005)
Herschel Island	-0.6	1952-1970	32	Lantuit and Pollard (2008)
Herschel Island	-0.5	1970-2000	32	Lantuit and Pollard (2008)
Resolute Bay	**Aggradation****	1958-2006	12–13	St Hilaire-Gravel *et al.* (2012)
Russia				
Marre-Sale	-1.7	1978-2003	NA	Vasiliev *et al.* (2005)
Bykovsky Peninsula	-1.6	1951-1964	150	Lantuit *et al.* (2011)
Bykovsky Peninsula	-1.2	1964-1969	150	Lantuit *et al.* (2011)
Bykovsky Peninsula	-1.6	1969-1975	150	Lantuit *et al.* (2011)
Bykovsky Peninsula	-2.1	1975-1981	150	Lantuit *et al.* (2011)
Bykovsky Peninsula	-1.6	1981-1986	150	Lantuit *et al.* (2011)
Bykovsky Peninsula	-1.1	1986-2006	150	Lantuit *et al.* (2011)
Buor Khaya	-1.3	1974-2010	1	Günther *et al.* (2012)

Negative rates refer to erosion, positive rates to accumulation. Positive rates are in bold face.
*The study by Ping *et al.* (2011) is based on 48 sites distributed across the length provided in this table (1957 km). In reality, the distance covered is 48 km, **The study by St Hilaire-Gravel *et al.* (2012) did not provide aggradation rates.

Figure 2.23. A table of recently published coastal erosion studies for permafrost coasts including study location, mean annual erosion rate, study time period, length of coastline studied, and the study authors, as compiled by *Lantuit et al.* [2013].

Chapter 3

Changes in Arctic Sea-Ice and Oceanographic Conditions

Sea-ice decline

One of the most fundamental changes occurring in the Arctic Ocean is the disappearance of sea-ice. Sea-ice is melting earlier in the spring and is developing later in the fall. Since 1979, the initial point of comprehensive satellite measurements, perennial sea-ice (ice that survives the summer and thus exists longer than a one year time span) extents have decreased by approximately half, leading to the "Arctic Death Spiral." Figure 3.1 shows this death spiral by identifying the ice volume measured each month while Figure 3.2 pictorially represents the perennial sea-ice found in 1980 vs. 2012.

Barnhart et al. [2014a] has delved into the details of these trends discovering that although ice is melting earlier in the spring (typically by $\sim$1.5 days yr^{-1}), it is also taking longer to form in the fall ($\sim$2 days yr^{-1}). Hence the number of open water days is growing faster in the fall than in the spring.

This perennial ice is being rapidly replaced by thinner first-year ice, leading to significant changes in the thickness of the ice cover. Winter first-year ice thicknesses are generally 1.5 to 1.8 m (based on modeling, e.g., see PIOMAS results [*Schweiger et al.*, 2011]; airborne observations by EMI [*Haas*, 2012]; and satellite observations, e.g., IceSAT [*Kwok et al.*, 2009] and CryoSat).

Notable from Figure 3.2 is the decline in land fast sea-ice, particularly in the Beaufort Sea and Canadian Basin. Although not shown in Figure 3.2, the decline in land fast sea-ice mimics the same trailing ends with ice melting earlier in the spring and taking longer to form in the fall [*Lee et al.*, 2012]. The fastest decline and greatest loss in Arctic summer sea-ice is in the East Siberian, Chukchi, and Beaufort Seas [*Stopa et al.*, 2016; *Lee et al.*, 2012]. Additionally, the ice edge is now located beyond the continental shelf edge, exposing a significant area of deep ocean that was previously ice covered.

Superimposed on Figure 3.2 is an illustration of the Beaufort Gyre and the Transpolar drift current. The Beaufort Gyre is a large scale current, produced by large scale atmospheric circulation, that carries sea-ice clockwise from the Siberian and Alaskan coasts towards

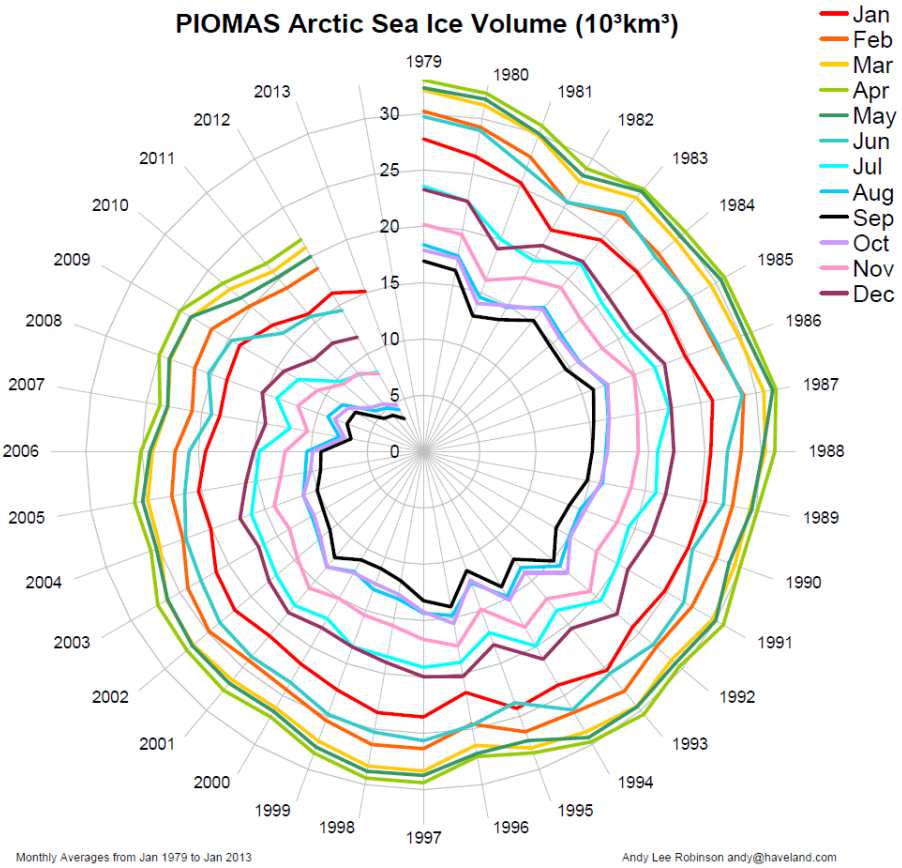

Figure 3.1. The "Arctic Death Spiral" created by the Pan-Arctic Ice Ocean Modeling and Assimilation System (PIOMAS) showing the decline in sea-ice volume from 1979 through 2016 [*Robinson*, 2016; *Schweiger et al.*, 2011]. Since 1998 it is clear that the overall volumes have been on a steady and steep downward path regardless of the season.

the Transpolar Drift Current and out the Fram Strait. This current is responsible for the generation of most of the thickest and oldest ice in the Arctic Ocean, adjacent to northern Greenland and the northwestern margin of the Canadian Arctic. The Beaufort Gyre carries ice from the northwestern margin of the Canadian Arctic southwestward into Alaska and the Yukon and then back up. Since sea-ice is now melting completely in the summer, there is no ice to circulate in the Gyre, which in turn is helping to accelerate the decay of older ice.

These documented reductions in sea-ice cover are leading some models to predict an "ice-free" Arctic summer in the near future; Peter Wadhams (Professor of ocean physics at Cambridge University) believes this could occur as soon as 2018 [*McKie*, 2016]. Sea-ice is still expected to form during the winter, however the total extent will continue to shrink.

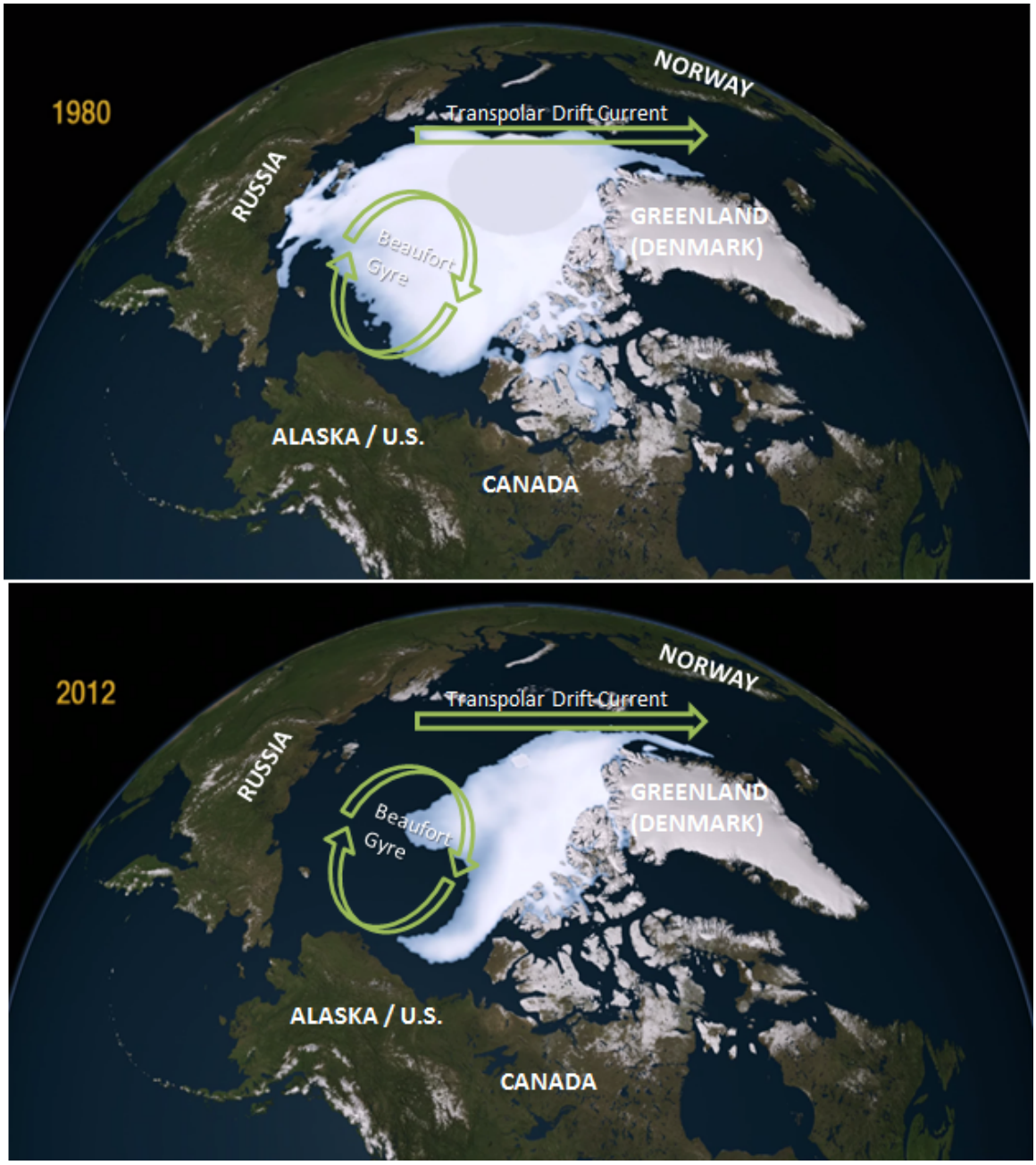

Figure 3.2. These images, taken as still shots from a NASA produced video, pictorially illustrate the effect of the death spiral by showing the decline in perennial sea-ice [*NASA*, 2016]. The grey disk at the North Pole indicates the region where no satellite data is collected.

Wave growth

Ocean waves are generated as wind blows over the surface of water. The friction at the air-sea interface (due to surface tension interacting with a driving force), and the fact that

sea water is a liquid which is capable of deformation in response to a driving force, result in the development of waves in response to wind. The length of water over which wind blows is known as the fetch length. The magnitude and duration of wind combined with the fetch length, water depth, and the width of the fetch length all affect the formation of ocean waves. Fetch length has been found to be the limiting variable for wave generation in coastal regions and marginal seas [*Hasselmann et al.*, 1973]. In open oceans however, duration is often the limiting variable for wave growth [*Young*, 1999].

There are two distinct classes of waves: wind and swell. Wind waves (or *wind-seas*) are directly generated by local winds and tend to be of higher frequency with shorter wavelengths ($\sim$100 m). Swell waves are not generated locally; they are the accumulation of energy in wind-seas generated elsewhere that have traveled over a long distance. Swell waves tend to be of lower frequency with longer wavelengths (>300 m).

Empirical models are used to describe the evolution of waves along a fetch x acted on by a uniform wind velocity U. Using the nondimensional parameters of wave energy, ϵ, fetch, χ, and storm duration, τ these models are [*Young*, 1999]

$$\epsilon = \frac{g^2 H^2}{16U}; \quad \chi = \frac{gx}{U^2}; \quad \text{and } \tau = \frac{gt}{U} \tag{3.1}$$

where H is significant wave height, g is gravity, and t is duration. Even though uniform winds are rarely observed, these empirical fetch laws provide surprisingly good agreement with observations [*Schwendeman et al.*, 2012]. The PiersonMoskowitz limit asserts a maximum nondimensional energy for wind-seas of ϵ=3.64x10^{-3} [*Pierson & Moskowitz*, 1964].

Traditionally the Arctic Ocean has had little to no waves to characterize. The large swath of perennial sea-ice severely limited the fetch length for wave development. However, as the perennial sea-ice has been melting and the duration of open water has been increasing, ocean waves are now increasingly developing in the Arctic Ocean. The geometry of the open water, as dictated by the sea-ice coverage, and the wind magnitude and direction determine this wave growth. As more open surface is exposed, larger amplitude and longer wavelength waves can be generated. Figure 3.3 pictorially illustrates the key physical processes that are resulting due to the alterations of exchanges of momentum, heat, and gases as the state of the ice shifts from pack ice, to a marginal ice zone (MIZ), and finally to open water. Figure 3.3 not only illustrates the development of wind-driven waves, but it also highlights other key physical phenomena that are strongly influenced by wind-driven waves. It is clear that thermodynamic effects play center stage.

Thomson & Rogers [2014] have shown that in the Arctic Ocean there is now enough open water that wind-seas are able to evolve into swell-seas. This continuum of wind- to swell-seas has allowed *Thomson & Rogers* [2014] to determine a new empirical relationship between ϵ and χ that includes both wind- and swell-seas. To isolate wind- and swell-seas, the nondimensional wave age was employed: $^{c}/_{U}$ which is the ratio of the dominant wave celerity c to wind speed. Pure wind-seas have an age less than one, indicating that the wind drives

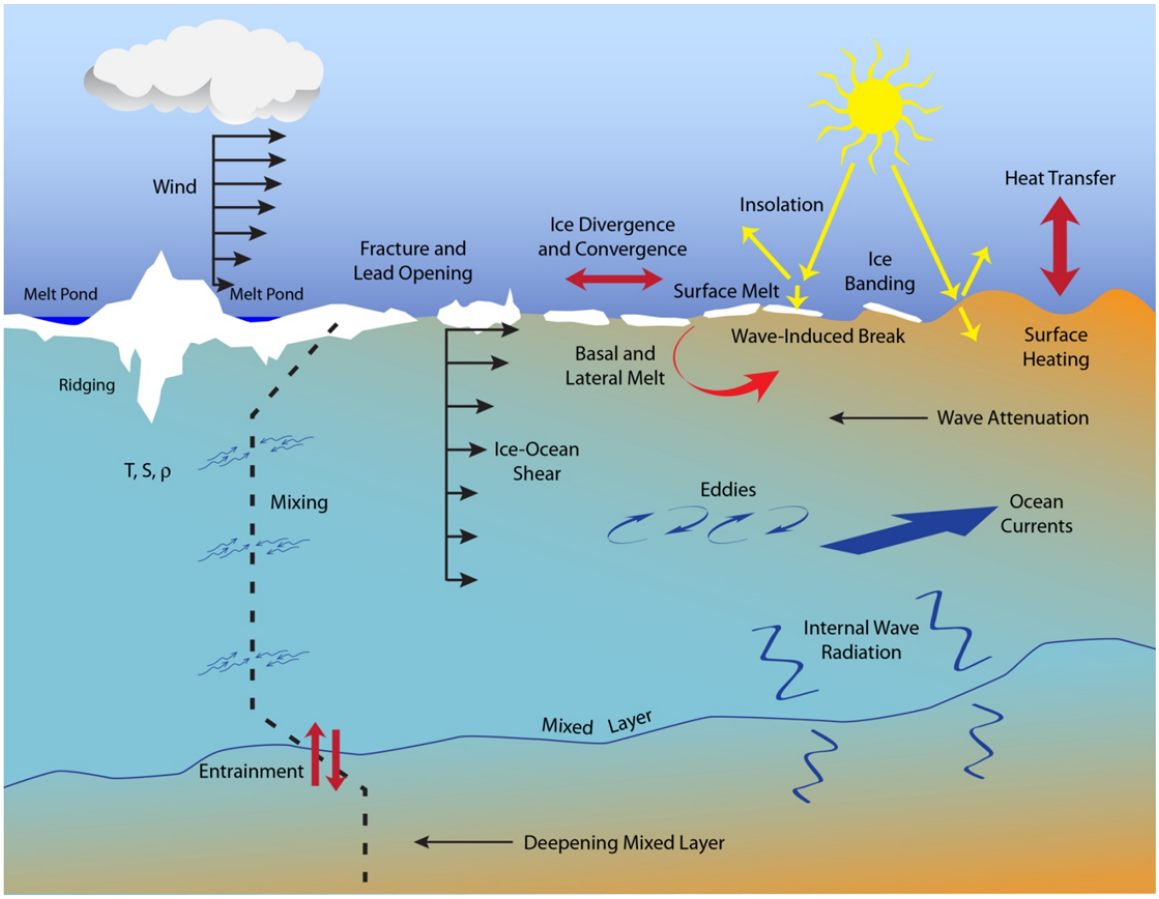

Figure 3.3. Illustration of the physical processes found in the Arctic Ocean from perennial sea-ice through the MIZ to the open ocean. Adapted from *Lee et al.* [2012].

these waves. The value of ϵ for wind-seas is less than the PiersonMoskowitz limit. Swell-seas have an age greater than one, indicating these waves have outrun the wind and the ϵ for these seas is greater than the PiersonMoskowitz limit. Further, *Thomson & Rogers* [2014] established that the open water distances are the controlling variable for wave generation in the Beaufort Sea (and likely the rest of the Arctic Ocean).

The *Thomson & Rogers* [2014] finding carries large importance because swell-seas carry more energy and have longer attenuation scales within ice than wind-seas [*Squire*, 2007]. In fact, a 20 s wave was recorded as propagating 1400 km into the ice pack with a 3 cm height [*Stopa et al.*, 2016] (original data [*Wadhams & Doble*, 2009]). These long propagation distances into the ice pack are thought to be involved in break-up of the pack by causing the sea-ice to flex rhythmically with their passing.

Relationship between oceanographic conditions and coastal geomorphic work

Given the fact that Arctic sea-ice is now subject to the influence of wind and swell waves, it is possible that increased wave activity in the Arctic Ocean will be the feedback mechanism that that drives the Arctic towards an ice-free summer. In addition to this, the other nonlinear feedback mechanisms illustrated in Figure 3.3 are of significant importance for the state of the ocean. The albedo of sea-ice is large compared to open water, and most of the incoming solar radiation incident on sea-ice is reflected back to the atmosphere. The thermal conductivity of sea-ice is small when compared to the ocean, so sensible energy transport between ocean and atmosphere is limited in the presence of sea-ice. As the sea-ice melts, increased insolation and increased mixing due to wave development will increase the temperature of the Arctic Ocean in concert with changing density and salinity due to the influx of fresh water. This will not only increase basal melting of sea-ice (melting from below), but warmer waters are interacting with submarine permafrost on the shallow continental shelves, as well as terrestrial permafrost along the coastlines.

Historical data from satellite-derived ice concentrations show the largest changes in ice cover are occurring in the East Siberia, Chukchi, and Beaufort Seas. These seas also have large relative changes in seasonal sea-ice coverage, with minimum coverage in August, September, and October. The largest waves are seen in October, with similar proportions of wind (40%) and swell (60%) waves [*Stopa et al.*, 2016]. The largest magnitude winds occur between November and December [*Stopa et al.*, 2016]; if a lack of sea-ice were to continue into these months, it is certain that even larger waves would be generated. *Solomon* [2005] reported that the highest average coastal retreat rates along the Canadian Beaufort coastline are found in areas that are most exposed to northwest winds. Conversely, *Solomon* [2005] found the lowest mean rates of coastal retreat were in areas sheltered from northwest winds. Hence there is evidence directly correlating wind and coastal exposure to increased erosion with the mitigating element being the production of waves.

The locations where sea-ice is declining most rapidly tend to be collocated with coastal regions containing high ground ice contents, as shown in Figure 3.4. These ice-rich permafrost regions seem to be very susceptible to erosion, perhaps due to the effectiveness of the delivery of heat to the coast [*Barnhart et al.*, 2014a]. As already mentioned, two factors are colluding to deliver this heat to the permafrost:

- the development of ocean waves is allowing the coastline to be impacted by Arctic Ocean water
- the temperature, salinity, and density of this water is now a dynamic variable that has been increasing in its capacity to deliver heat

The delivery of heat to these ice-rich permafrost regions are resulting in accelerated and devastating erosion rates (with average rates up to $17.3\,\mathrm{m\ yr^{-1}}$ [*Arp et al.*, 2010]).

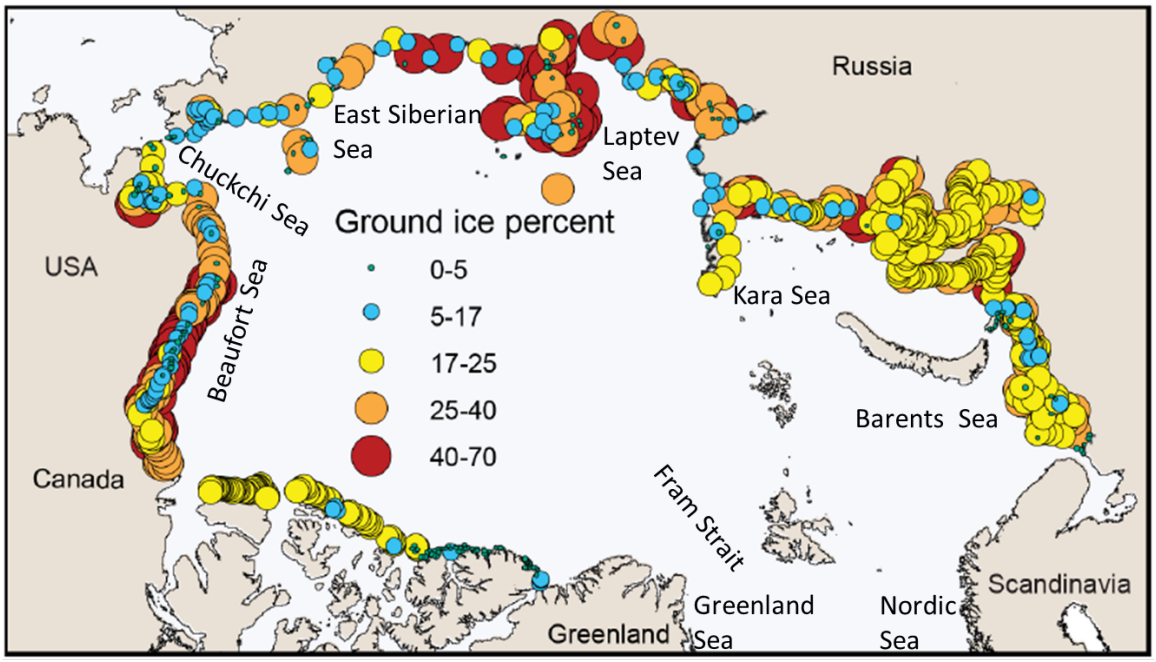

Figure 3.4. Permafrost ground ice content along studied Arctic coastlines. High ice content is found along the Northern Alaskan coastline. Adapted from *Barnhart et al.* [2014a].

Some positive correlation was observed between wave heights of over 1 m and coastal retreat rates (see Figure 3.5) in a study by *Hequette & Barnes* [1990]. The same study also found a similar positive correlation between wave power and coastal retreat rate (also shown in Figure 3.5). However, *Lantuit et al.* [2011] found no relation between storminess and erosion for the Bykovsky Peninsula for the years 1958-2006, but acknowledged that such a relationship is difficult to establish when the impacts of individual storms cannot be resolved, and when various confounding influences are present, such as variable sea-ice, water levels, and differences in the sediments and ground ice contents.

The time and spatial scales over which the influence of sea-ice in the Arctic Ocean can be considered results in distinct modeling goals. As identified in Figure 3.6, distinct model goals span distinct time horizons and spatial scales. Each of them are important to correctly predict sea-ice within the Arctic, however due to limits in computational resources, it is not possible to cover the same level of detail at all spatial scales.

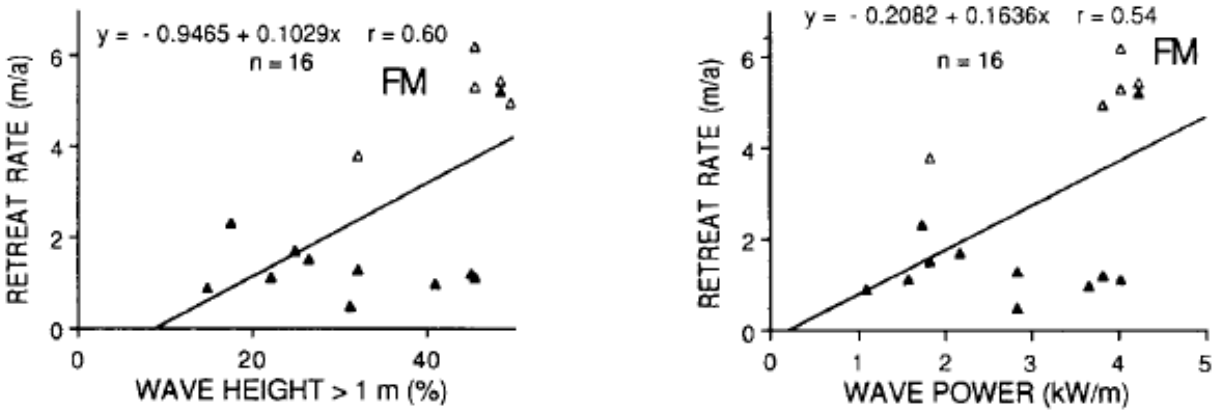

Figure 3.5. Correlations between coastal erosion rate and wave height, and coastal erosion rate and wave power, as calculated by *Hequette & Barnes* [1990] for the Canadian Beaufort Sea.

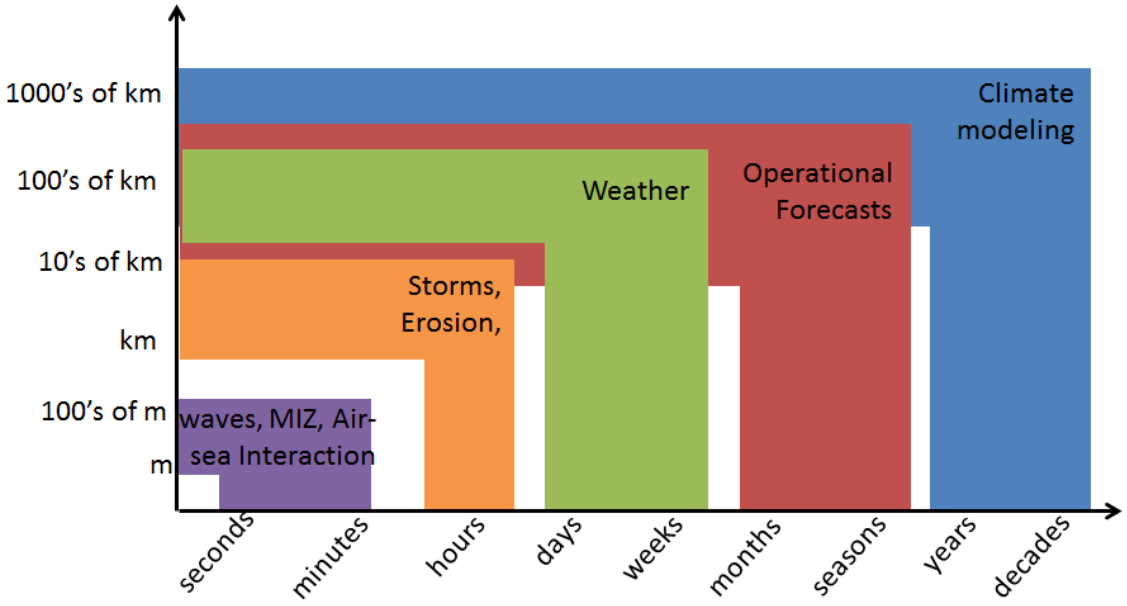

Figure 3.6. Links between time and spatial scales for ocean-ice modeling.

Chapter 4

Arctic Coastal Geomorphology

Permafrost History and General Description

By definition, *permafrost* is ground (soil, rock, or sediment) that remains frozen (temperature $< 0°C$) for two or more consecutive years. Permafrost underlies most land surfaces in the Arctic, varying from a few meters to several hundred meters thick, depending on its thermal history. The ice content of permafrost can vary significantly. It can be ice-rich, or it can contain practically no ice at all. The surface layer, called the *active layer*, typically thaws and re-freezes each year. Figure 4.1 shows a map of circum-Arctic permafrost distribution, showing regions of continuous, discontinuous, sporadic, and isolated permafrost. Permafrost along the Arctic Ocean coastlines is predominantly continuous.

Ice wedges and polygonal surface features (i.e., *ice-wedge polygons*) are typical of permafrost landscapes (see Figure 4.2). These form when thermal contraction during winter months cracks the frozen ground, much like the surface of sunbaked, dried mud. During the warmer, wetter season, water infiltrates the cracks and refreezes. Consecutive freeze-thaw cycles cause the ice wedges to grow and expand up to several meters wide, and 10s of meters deep, forming polygonal features often clearly seen on the surface. A recent survey of ground ice along the Alaskan Beaufort Sea coast found wedge ice and ice-wedge polygons nearly everywhere [*Kanevskiy et al.*, 2013].

In Alaska, the permafrost is thickest north of the Brooks Range. On the Arctic coastal plain along the Beaufort Sea, it extends as much as 2,000 feet below the surface, and most permafrost temperatures at the depth of zero annual amplitude vary between -10° to -5°C [*Kanevskiy et al.*, 2013]. Most of this permafrost formed tens of thousands of years ago during the late Pleistocene (more commonly known as the last ice-age ∼126,000-12,000 years ago), when the mean annual air temperature was much colder than today. Although the term permafrost implies a sense of permanence, permafrost is continually adjusting to changes in the thermal regime, and still warming since the last glacial maximum.

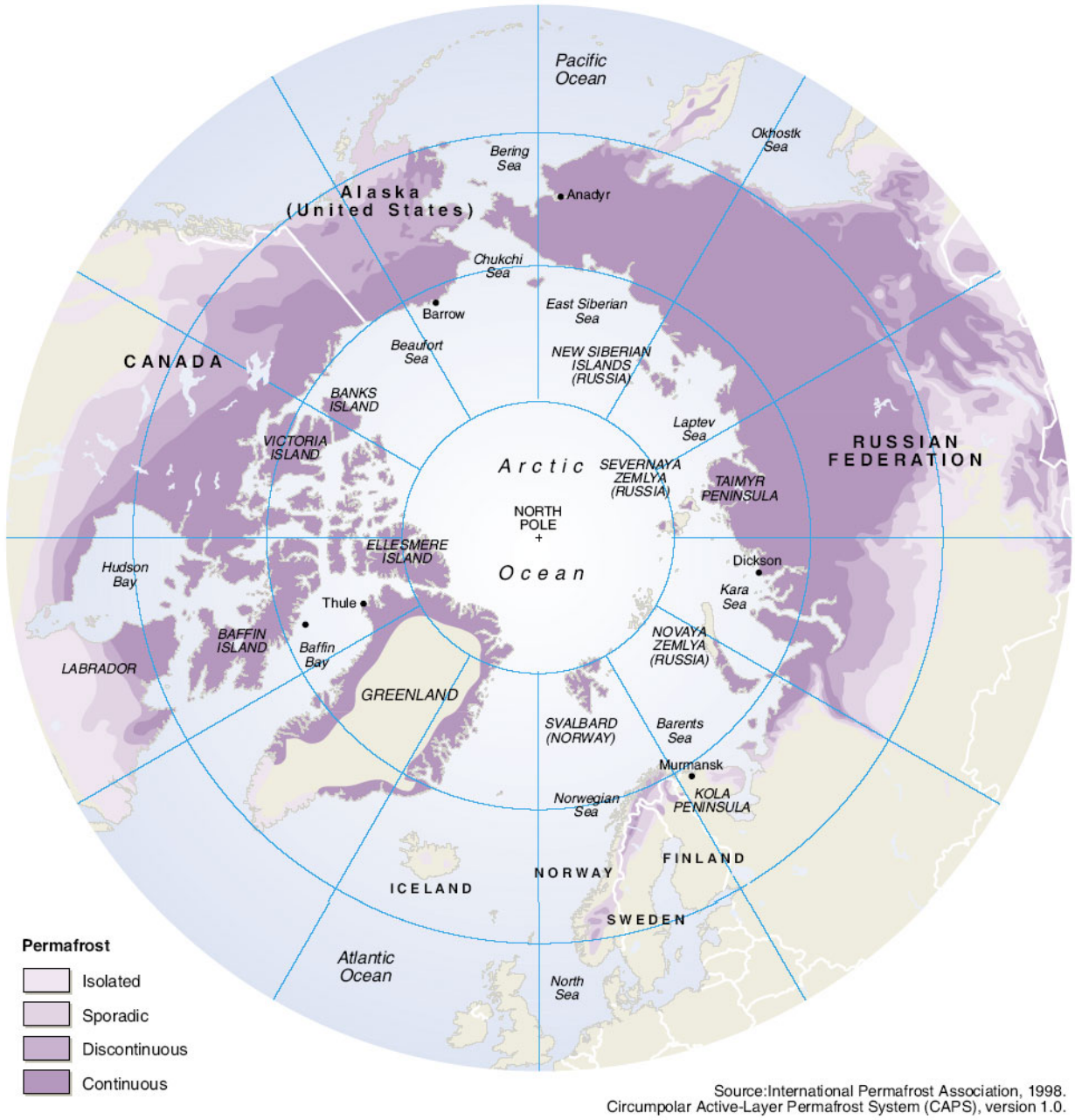

Figure 4.1. Map of permafrost distribution in the Arctic. Regions of isolated, sporadic, discontinuous, and continuous permafrost are shown. Adapted from [*Brown et al.*, 1998].

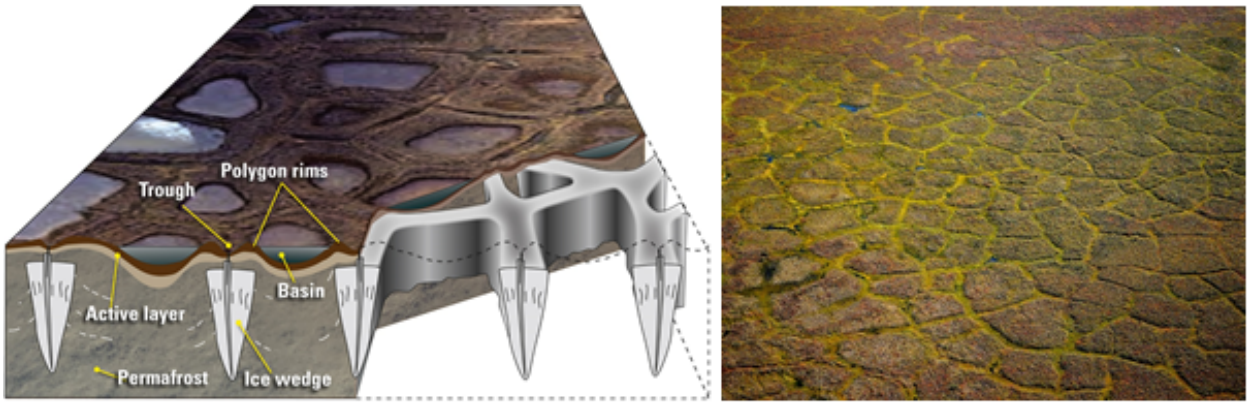

Figure 4.2. A schematic illustrating the formation of ice wedges and ice-wedge polygon landscapes. Adapted from [*Martin et al.*, 2009].

Ground-Ice Contents and Sediment/Terrain Types

The lithology of coastal sediments varies dramatically, but can generally be classified as lithified or unlithified. Along the circum-Arctic coastline, the Arctic Archipelago islands are generally rocky and lithified, while the vast majority of the mainland coasts are composed of unlithified, sedimentary deposits [*Overduin et al.*, 2014]. During the severely cold environment of the late Pleistocene, much of the Arctic mainland coastline remained unglaciated, and active sedimentation occurred [*Harper*, 1990; *Kanevskiy et al.*, 2011]. Such an environment was favorable to the accumulation of thick sequences of fine-grained, silt-dominated sediments that froze as they were deposited, forming into bodies of ice-rich syngenetic permafrost called yedoma. Yedoma is widespread in northern Siberia (see Figure 4.8), along the Beaufort Sea coast in Alaska (see Figure 4.4), the Yukon, and Northwest Territories, Canada [*Harper*, 1990]. It is a surficial deposit up to 50 m deep, with large syngenetic ice wedges often spanning the entire depth [*Kanevskiy et al.*, 2011]. Regions with high ice-contents often indicate yedoma permafrost (see Figure 4.3, which shows the ground ice content along the Arctic coastlines).

Alaska

Recent work by *Kanevskiy et al.* [2013] documented 65 study sites along the Alaskan Beaufort coast, from Pt. Barrow to the Canadian border. Each site was organized into one of five terrain units, distinguished on the basis of geomorphology and surficial geology (shown in Figure 4.5): primary surface of the coastal plain (western and eastern regions), yedoma, drained-lake basins, deltas and tidal flats, and eolian sand dunes.

According to *Kanevskiy et al.* [2013], the primary surface of the coastal plain is mostly

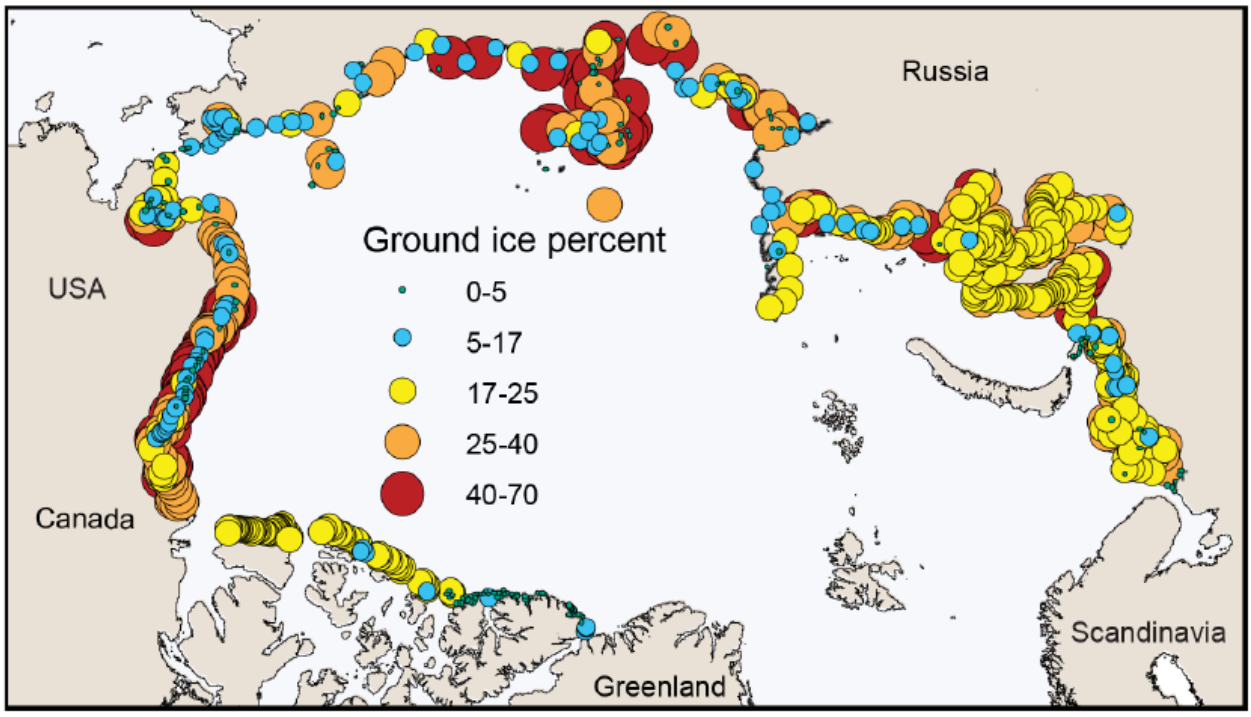

Figure 4.3. Permafrost ground ice content along studied Arctic coastlines. Adapted from [*Barnhart et al.*, 2014a; *Lantuit et al.*, 2012].

made up of silty sand and gravel in the eastern region, and silt and silty clay in the western region. The average volumetric ice content for the western region is 86%, while for the eastern region, volumetric ice content average is 80%. The majority of the ice content in both regions consists of segregated and pore ice, but wedge ice is common with a typical polygon spacing of 14 m.

The yedoma region of the low foothills is mostly made up of eolian silt (loess). This type of permafrost is widespread along the coast west of Pt. Barrow (see Figure 4.6), but much reduced in the east. The average volumetric ice content is 89%. The majority of the ice content in yedoma is wedge ice (50%), and the typical polygon spacing is 8 m.

Drained lake basins are associated with both new and old ice wedge polygon features, varying in size between 11 to 60 m. The largest polygons occurred in young, recently drained basins, suggesting that polygons are subdivided over time. Total volumetric ice content is 82%, with an average of 8% wedge ice volume.

In deltas and tidal flats, new deposition occurs of silty and clayey sediments. At the majority of these sites studied by *Kanevskiy et al.* [2013], well developed polygons were observed, with an average size of 22 m. The total ice volume is 73% on average, with an average 6% wedge ice.

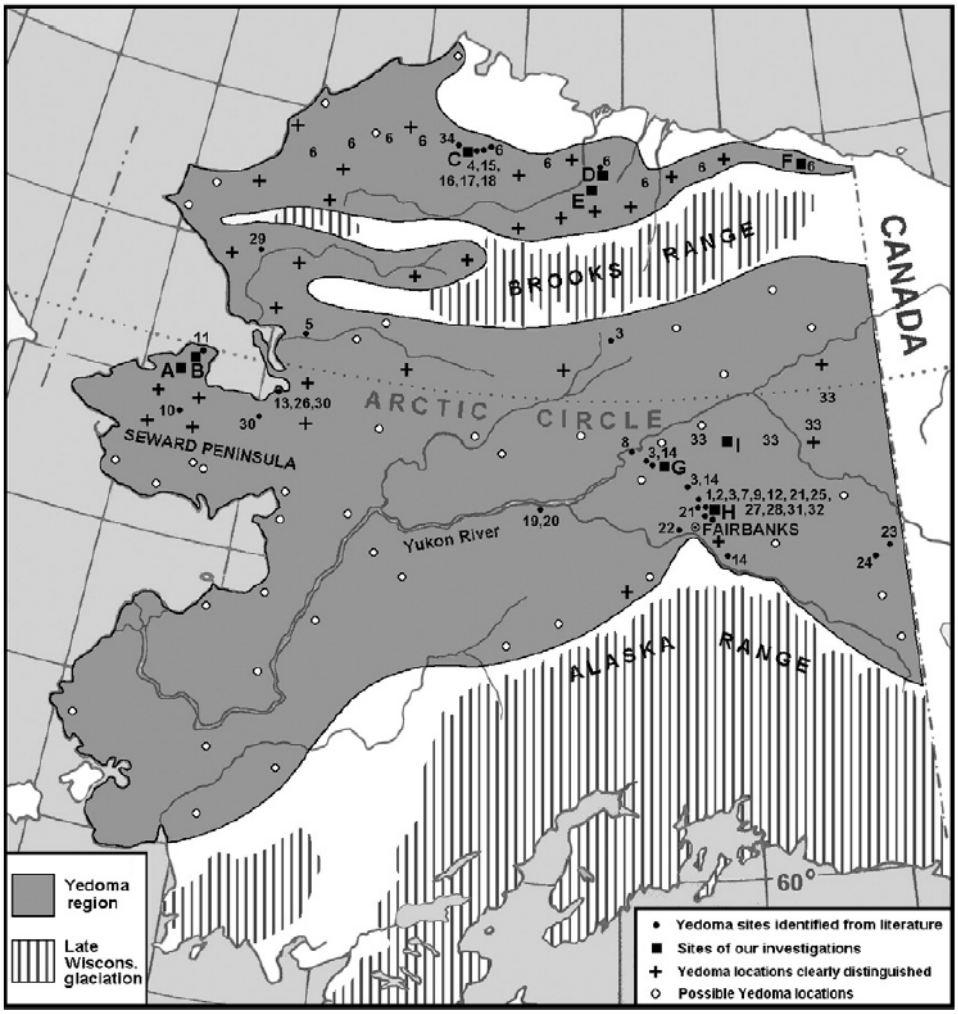

Figure 4.4. Distribution of yedoma permafrost in Alaska. Adapted from [*Kanevskiy et al.*, 2011].

Sand dune regions contain the least amount of total volumetric ice content (43%), which is almost entirely pore ice. The low ice content can be explained by the low frost susceptibility of sands, and the low moisture content typical of well drained soils. Very few developed polygons were observed (4% volumetric ice content). Those that were observed had an average spacing of 16 m.

Canada

Along the Canadian Beaufort Sea coast, sediments consist mainly of glacial and glacial-marine deposits in the west, deltaic and glacial marine deposits in the Mackenzie Delta area, and principally outwash materials around the Tuktoyaktuk Peninsula [*Harper*, 1990].

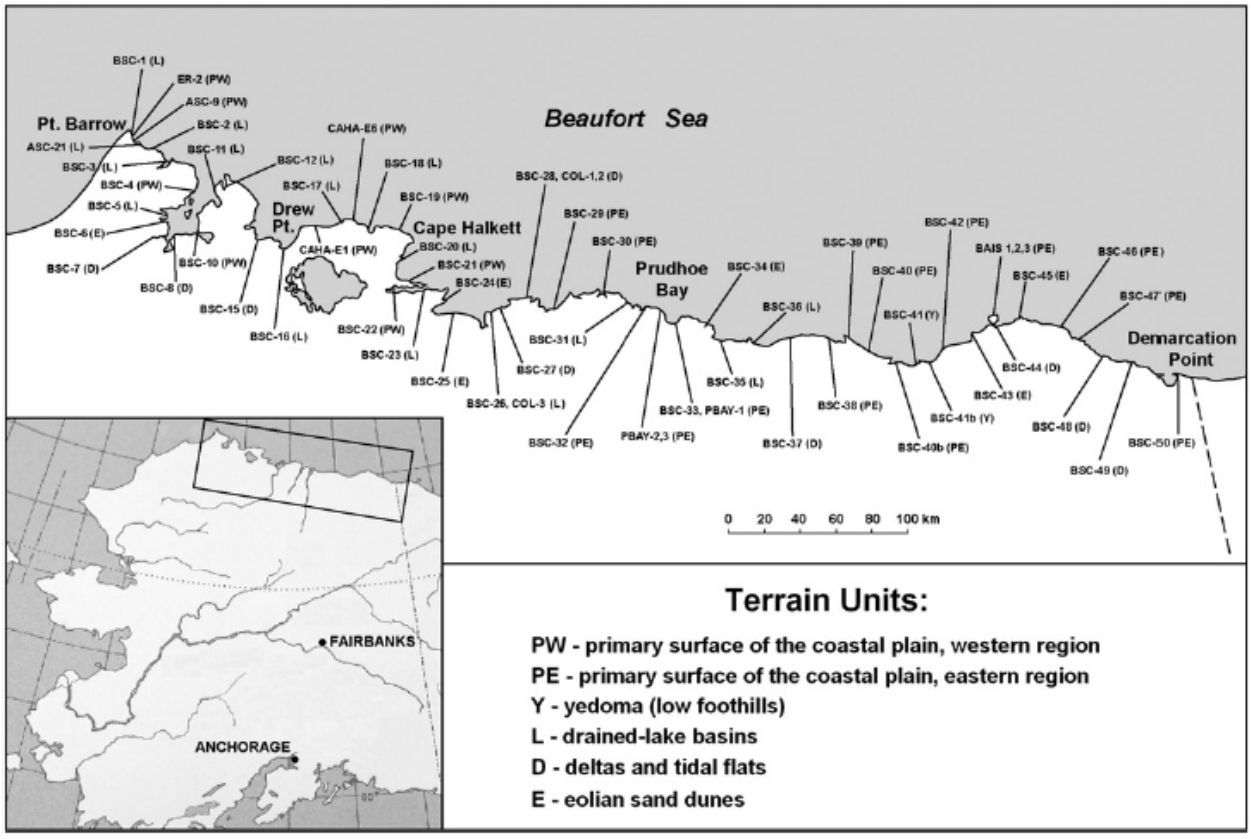

Figure 4.5. Terrain units along the Alaskan Beaufort coastline studied by *Kanevskiy et al.* [2013].

Massive ice and pore ice are common. Several types of coastal geomorphology were identified by *Harper* [1990], including ice-rich and ice-poor cliffs, low tundra cliffs, inundated tundra, barrier islands and spits, and flat wetland complexes. While landscapes varied, 80% of the coast was classified as erosional, which included deltas.

Harper [1990] and *Hequette & Barnes* [1990] describe the geomorphology observed along the Canadian Beaufort Sea coast. Coastal cliffs along the eastern Yukon coast are up to 30-50 m tall, consist of fine-grained, unlithified sediment, with narrow beaches. Along the western Yukon coast, low gravel/sand barriers enclosed shallow lagoons, and alluvial deltas and widely spaced inlets were observed with very low relief (< 5 m). Richards Island cliffs are variable, between 2-10 m tall, and contained predominantly interstitial ice (some massive ice was observed, but not common). On the Tuktoyaktuk Peninsula, cliff height was typically less than 5 m, also containing predominantly interstitial ice within sands overlain by till and glacial outwash of various thickness. Along Liverpool Bay, cliffs were predominantly ice-rich, had variable heights (2-10 m tall), with many flats and offshore bars. Finally, at the Mackenzie River Delta, some ice-rich cliffs were observed, but the landscape was dominated by tidal flats, wetland complexes and channels, with some barrier spits and very low relief ($<$

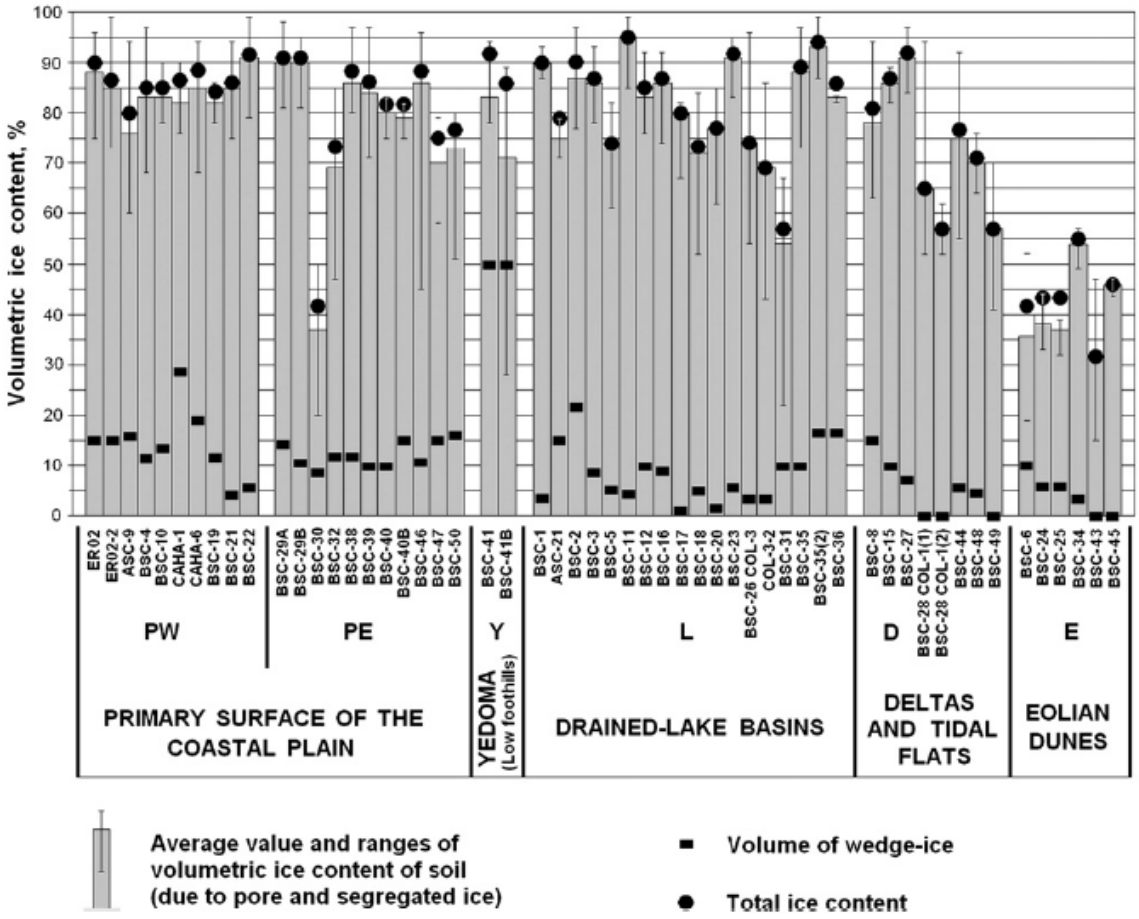

Figure 4.6. Volumetric ice content in the upper permafrost for each coastal terrain type in Alaska studied by *Kanevskiy et al.* [2013].

2 m). Unlike the Alaskan study by *Kanevskiy et al.* [2013], *Harper* [1990] does not specifically measure ice content or polygon spacing.

Siberia and Other Coasts

A systematic classification of the coastal geomorphology for the Siberian coastlines does not exist in English-language literature. *Grigoriev et al.* [2006] concluded that less than 4% of the East Siberian coastline and about 12% of the yedoma ice complex and thermokarst affected coasts have been studied. However, individual studies provide some information. A substantial portion (about 25%) of the Siberian coastline and coastal plain consists of yedoma, a fine grained and ice-rich surficial layer of syngenetic permafrost [*Grosse et al.*, 2013; *Günther et al.*, 2013]. Figure 4.8 shows a map of yedoma distribution in Siberia. In

Regional and subregional distribution of coastal types and modifiers

Coastal types and modifiers	Western Yukon (km)	Eastern Yukon (km)	Mackenzie Delta (km)	Richards Island (km)	Tuktoyaktuk Peninsula (km)	Liverpool Bay (km)	Region (km)
Coastal types							
Ice-rich cliffs	8	75	36	26	5	254	404 (19%)[1]
Ice-poor cliffs	19	51	20	67	94	153	404 (19%)
Low tundra cliffs	6	12	2	22	225	10	282 (14%)
Inundated tundra	3	7	8	18	98	26	160 (8%)
Barrier islands/spits	42	45	30	39	163	103	422 (20%)
Flat/channel/wetland complexes	19	12	344	4	4	21	404 (19%)
Total mapped	97	202	442	183	588	588	2077 (80%)
Unmapped[2]	1	0	166	254	78	27	526 (20%)
Total (mapped + unmapped)	98	202	608	437	666	591	2603 (100%)
Modifiers							
Flats/bars	5	2	0	64	275	244	
Ground-ice slumps	8	11	13	12	3	35	

[1]Proportion of coastline mapped.
[2]No aerial videotapes available and airphotos not of sufficient resolution for mapping.

Figure 4.7. Distribution of coastal types and modifiers along the Canadian Beaufort Sea coast. Adapted from [*Harper*, 1990].

Russian territory, yedoma is commonly referred to as ice complex. It is thicker than the yedoma deposits found North America, extending up to 50 m deep. For example, at the Bykovsky Bay near the Lena River Delta, ice wedges can be nearly 5 m wide, and reach 40-50 m deep. In yedoma coasts, the dominant landforms are cliffs (reaching 45 m high), retrogressive thaw slumping, and low-lying topographical depressions formed by thermokarst basins which cause subsidence [*Lantuit et al.*, 2011].

As described in the review by *Overduin et al.* [2014], the coastal zone of the East Siberian Seas consists of coastal lowlands in the western and central parts, with isolated ice complex deposits amongst thermokarst depressions. For example, at the Bolshoy Lyakhovsky Island, typical volumetric ice content can be up to 80-90% in thermo-terraces. Along the New Siberian Archipelago coast, volumetric ice content is lower (18-25%) and composed of sand and pebble Holocene accumulation. In the eastern part of the East Siberian Seas coast, rocky, lithified coastline is more common.

The review by *Overduin et al.* [2014] also describes the geomorphology of the Archipelagos of the high Arctic (Svalbard, Canadian Arctic Islands, Greenland, etc), whose coastlines are characterized as paraglacial, meaning they are on or adjacent to formally ice-covered terrain, where glacially excavated landforms or glacigenic sediments have a recognizable influence on the character and evolution of the coasts. These coasts are permafrost coasts, but they are made up of coarse-grained glacigenic sediments as well as by rocky, high-relief features such as fjords and narrow straits. Because of their paraglacial classification, these coasts are influenced more strongly by glacial loading and isostatic rebound.

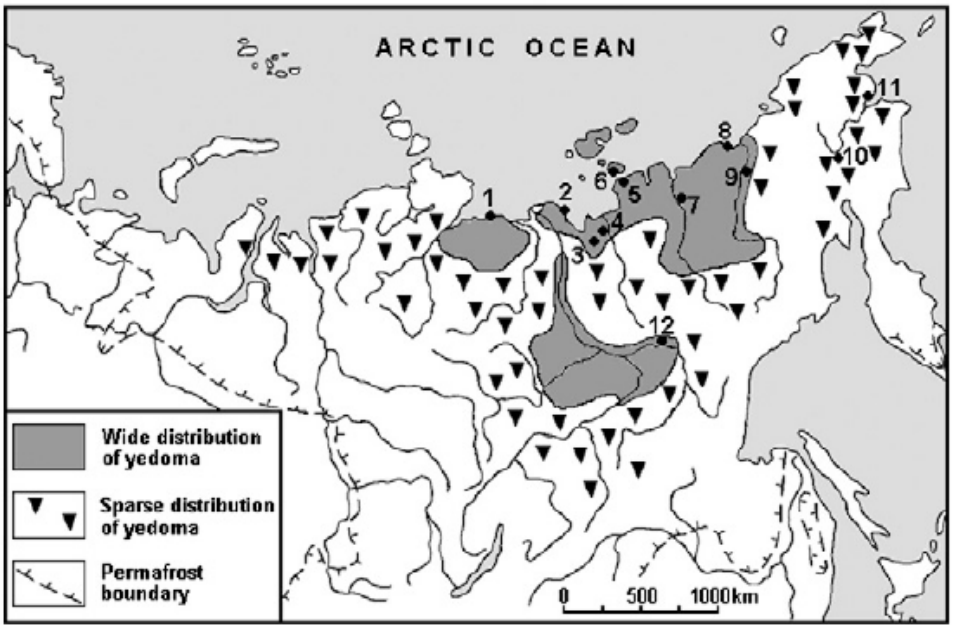

Figure 4.8. Distribution of yedoma permafrost in Siberia. Adapted from [*Kanevskiy et al.*, 2011].

Permafrost Thermal Regime

Permafrost is defined by the ground temperature, thus it is of fundamental importance to understand the thermal regime in a permafrost zone. Because the ground temperature must remain below freezing for at least two consecutive years, this naturally leads to the conclusion that permafrost will only exist where the mean annual air temperature has been below 0°C for an extended period of time. Figure 4.9 shows a typical ground temperature profile in permafrost ground. Several zones are generally identified.

Large temperature swings occur in the near surface zone. The near surface is where the active layer resides, which alternates between frozen and unfrozen depending on the season, or even the day. The time average of the temperature oscillations is below 0°C (i.e. mean annual air temperature). In general, the propagation of the mean annual air temperature into the ground depends on the rate of oscillation, the thermal conductivity of the ground material, and the absolute value of the temperature oscillation range. The oscillation rate is set by nature, as it is controlled by the change in winter and summer seasons. The absolute value of the temperature oscillation range is set by location, elevation, etc. And finally, the thermal conductivity of the ground material depends on the sediment or rock type. The propagation of the mean annual air temperature into the ground is more effective (e.g., propagated deeper) if the oscillation range is larger, the ground material is more conductive, or the rate of oscillation is slower. In this general and simple description, the effects of snow cover (insulation), hydrology, latent heat of phase change, and solar radiation are ignored.

For example, across the airsoil interface, snow acts to insulate during the winter but not during the summer, leading to thermal rectification and warmer mean soil temperatures than mean air temperatures [*Koven et al.*, 2013].

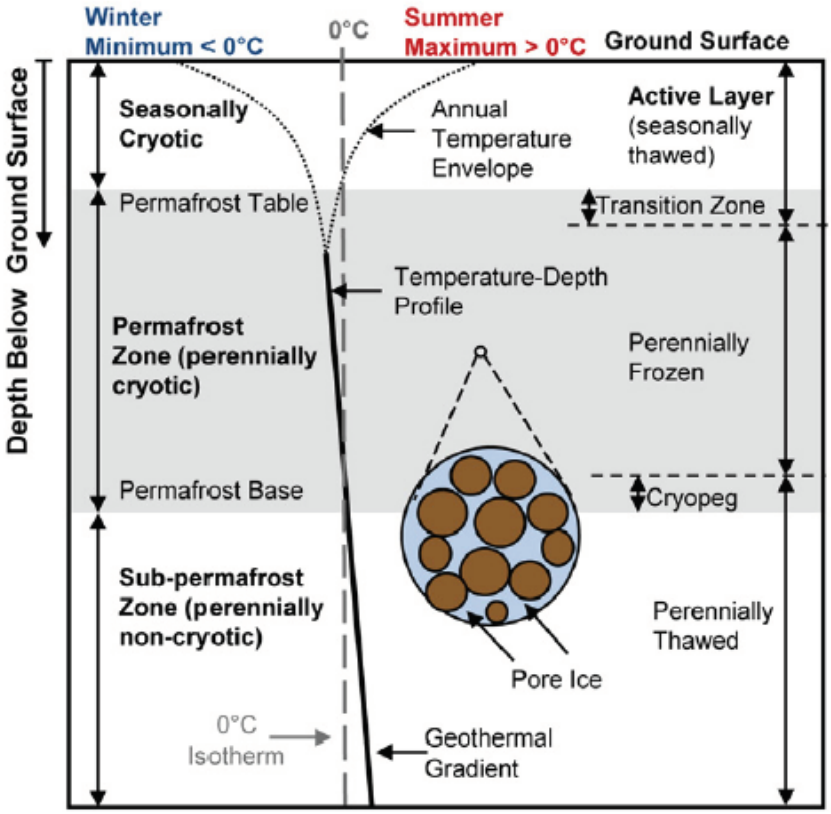

Figure 4.9. A typical permafrost ground temperature profile. Adapted from [*Woo et al.*, 2012; *Walvoord & Kurylyk*, 2016].

Below the active layer, the perennially frozen zone remains below freezing temperature all year. The depth at which this occurs is often called the *permafrost table*, similar in concept to a water table. Within the perennially frozen ground, varying amounts of pore ice may exist between sediment grains. While most coastal permafrost considered here contains significant pore ice or massive ice, it is possible that no ice exists at all (e.g., frozen bedrock, which is often the case in mountain permafrost, for example). The temperature profile within the perennially frozen zone is often linear, sloping along the geothermal gradient. It may also display temperature reversals (although always below 0°C) which often reflects more complex thermal history (Figure 4.10). The temperature profile might also become vertically linear, where the temperature is everywhere equal to ∼0°C along a depth interval. This vertically linear profile suggests ice-rich permafrost where phase change is occurring from ice to liquid (or vice-versa).

Due to geothermal heat flow from below, permafrost thickness is limited, and the ground remains perennially unfrozen at depth. Regions with high heat flow result in thinner permafrost, while regions with low heat flow tend to support very thick permafrost layers.

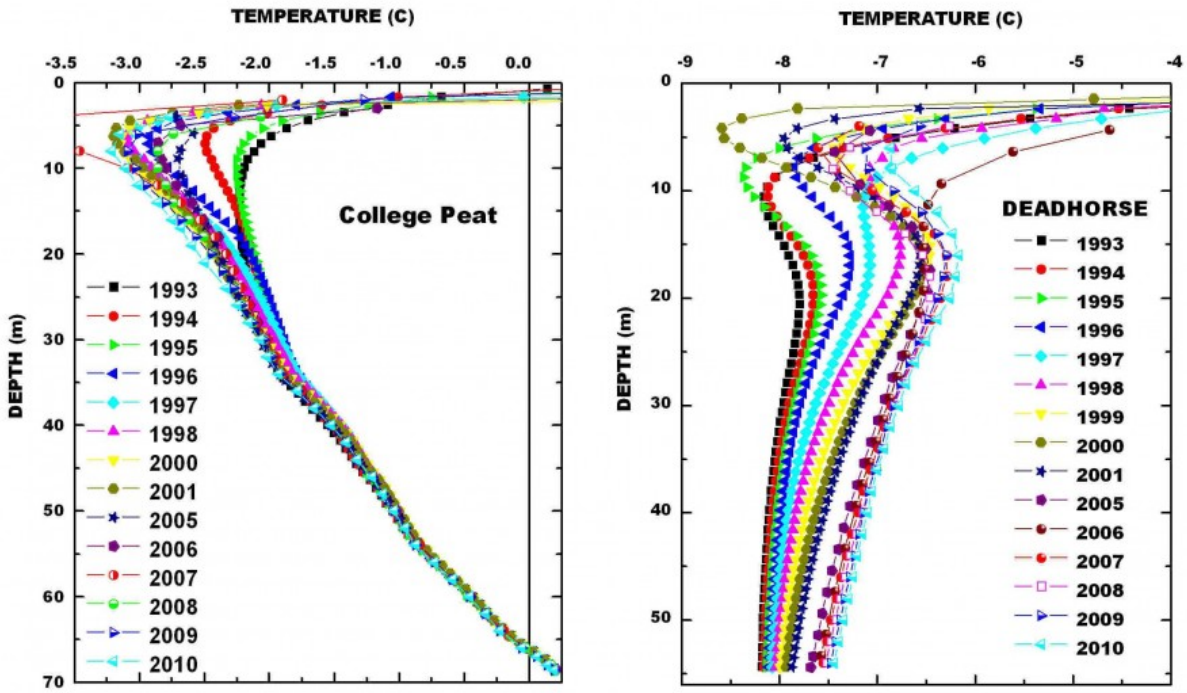

Figure 4.10. Permafrost ground temperature profiles at College Peat (near Fairbanks, Alaska) and Dead Horse, Alaska, recorded at similar times of the year. Images obtained from the Permafrost Laboratory, Geophysical Institute, University of Alaska, Fairbanks.

The thermal conductivity of ground material varies depending on the material type. The thermal conductivity of the ground is typically the dominant factor in how permafrost responds to changes in boundary conditions. The thermal conductivity is defined as the amount of heat that is allowed to pass through the material in unit time through a unit cross-sectional area under a unit temperature gradient. Most ground materials have thermal conductivity values on the order of $1\text{x}10^{-1}$ to $1\text{x}10^{1}$ W m^{-1} C^{-1} [*Farouki*, 1981]. The thermal conductivity of the ground should be thought of as an effective value, since the ground is made up of several constituents (e.g., rock/mineral particles, water, and air), each which contribute to the effective ground conductivity value.

In unsteady conditions, the thermal behavior of the ground also depends on the ground material's heat capacity, which is a measure of the amount of heat a material can absorb before changing temperature. The ratio of the thermal conductivity k and the heat capacity

C is called the thermal diffusivity,

$$\alpha = k/C \tag{4.1}$$

As described by *Farouki* [1981], ground that has a high thermal diffusivity value implies it has the ability to rapidly change temperature given some perturbation. In the case of permafrost, where high ice content may exist, permafrost ground can have a much greater thermal diffusivity than its unfrozen state due to two factors: the thermal conductivity of ice is higher than water and the specific heat of ice is lower than water. The resulting effect means temperature can change much more rapidly within permafrost than the equivalent unfrozen soil, because ice has a thermal diffusivity roughly eight times larger than liquid water [*Farouki*, 1981].

Areas where the mean annual air temperature has been consistently very cold are regions where the deepest permafrost occurs. Most of the permafrost in the Arctic formed during the glacial epochs, with the thickest permafrost forming in regions which were exposed to the atmosphere (although permafrost formation is possible underneath a cold-bedded ice sheet). Figure 4.11 shows simulated permafrost depths, constrained by observations, using an Earth system model. On a time-integrated scale, Earth's climate has spent more time in glacial epochs than interglacials, since glacial cycling first began (see for example *Lisiecki & Raymo* [2005]). Heat transfer by conduction is a slow process, therefore, much of the Arctic permafrost is still warming since its state at the last glacial maximum.

The depth at which each zone transitions to the next depends on the boundary conditions. For typical air temperatures and ground properties, diurnal penetration is on the order of 0.3-0.8 m, while annual penetration may be roughly 10 m [*Farouki*, 1981]. The active layer depth spans some upper portion of the annual penetration depth, for example.

Permafrost Strength Properties

Certain physical properties of permafrost may change as a function of temperature and ice content. Properties which are important to consider in our understanding of coastal erosion have also been historically important in other fields, namely in cold regions engineering and construction of infrastructure such as roads, pipelines, and buildings, as well as artificially frozen ground techniques in the mining industry [*Arenson et al.*, 2007]. These properties include: tensile strength, shear strength, and cohesion of ice and/or of frozen ground.

A review of the rheology of frozen soils by *Arenson et al.* [2007] emphasizes that when the strength and deformation behavior of frozen ground is estimated, three main characteristics must be considered: (a) ice-content, (b) unfrozen water content, and (c) frost susceptibility. The ice-content and unfrozen water content are not only functions of temperature, but of other variables such as sediment type, pore water salinity, and freezing history. The essential information for each characteristic is summarized next. Additionally, Figure 4.12 provides a summary of several variables that affect the strength of frozen ground.

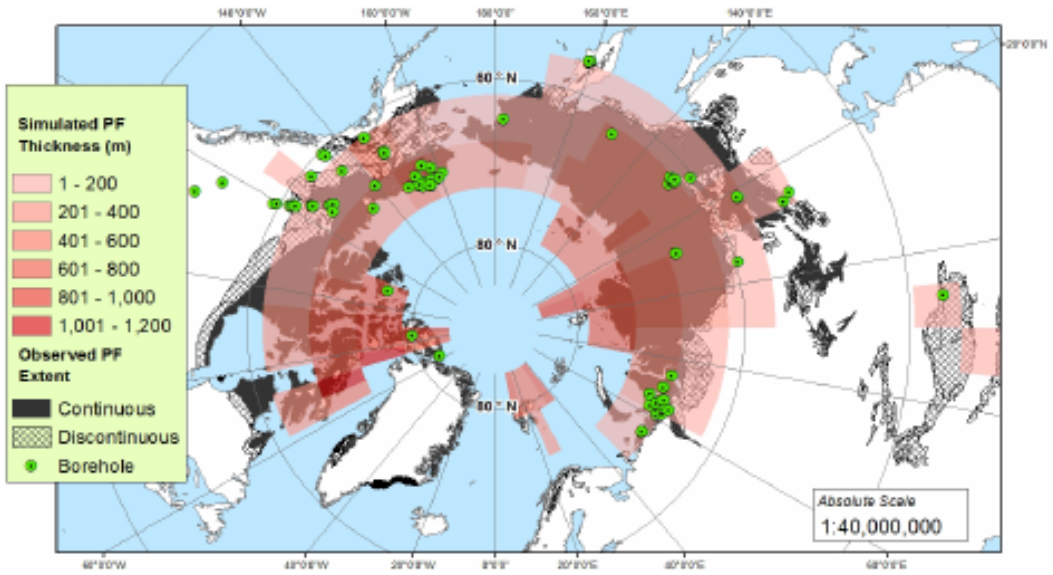

Figure 4.11. Map of deep Global Terrestrial Network for Permafrost (GTN-P) borehole locations with the simulated permafrost thickness and observed permafrost extent. Adapted from [*Kitover et al.*, 2015].

For ice-rich permafrost, significant creep deformation occurs, and the strength is mainly controlled by the characteristics of the ice and its interaction with the soil particles. Ice contents lower than 40% show distinct increases in strength due to cementation and increased interactions between ice and particles. The strength characteristics of the soil particles themselves are of secondary importance, suggesting that sediment type is not critical.

In general, unfrozen water content weakens a partially frozen soil, resulting in a strength decrease and the possibility of larger deformations, because the presence of water reduces ice cementation. Depending on the salinity, temperature, grain size, and pressure, the amount of unfrozen water content can be significant, even at temperatures below 0°C. Frost susceptible soils (e.g., poorly draining soils like clays and silts) tend to have larger unfrozen water contents at temperature well below 0°C, and also tend to change the inter-particle structure upon freezing when compared to non-frost susceptible soils (e.g., sands or gravels). An example of this is the formation of ice wedging, which is predominant in yedoma permafrost, but almost non-existent in sands or frozen dunes.

Finally, *Arenson et al.* [2007] recommends against extrapolations from individual studies, because of the great variety of mechanical responses from different soils. For example, a surface for the post-peak shear strength was determined as a function of the volumetric ice content and confining stress for a sandy gravel at -2°C, shown in Figure 4.13A. The surface is only valid for the sample tested. Nevertheless, individual studies such as this one show certain trends typical for most frozen soils, as explained in *Arenson et al.* [2007] and

Variable	Effect on strength of frozen soil
Temperature	Generally the strength increases as the temperature decreases. In addition, the stress-strain behaviour can change from ductile to brittle. The change in behaviour can be mainly attributed to the change in unfrozen water content, which is discussed later in the paper.
Strain Rate	An increase in strain rate results in an increase in strength, but also a change towards brittle behaviour, as shown in Figures 5 and 6. Under very low strain rates, creep dominates the deformation and sample response, because complete relaxation takes place in parallel to the small increase in stress caused by the added strain.
Ice Content	The strength increases as the ice content decreases because of the structural hindrance that develops as solid particles first contact each other. Within a medium to dense frozen soil, the ice is the bonding (cohesive) agency. This apparent cohesion results in a higher resistance at zero (tensile strength) and low confining stress compared to unfrozen soils. The confining stress represents the horizontal pressure applied on a soil sample during testing. Some researchers reported a slight decrease in strength for dirty ice [77, 78]. Numerical modelling on mixtures confirmed this observation and showed that the failure plane follows the boundaries between the ice matrix and the solids [79].
Air Content	Only a few tests on the effect of air content on the strength behaviour of frozen soils (or ice) are available [e.g. 67, 69, 80]. These tests suggest that the air within the samples suppresses any tendency for dilatancy to occur by providing significant opportunity for elimination of the air voids and associated contraction.
Confining Stress	Confining stress has a minor effect on the strength of ice [81] at stresses below the melting pressure. Only when the ice content decreases below approximately 60%, is the strength of a mixture increased by increased confinement. The more solid particles, the more pronounced the increase in resistance, because the component of resistance due to frictional dissipation of work is a function of the confining stress.
Salinity	The resistance of a frozen saline soil decreases as the salinity increases [82 - 84]. This is explained by the freezing point depression resulting in higher unfrozen water contents at similar temperatures. In addition, Arenson and Sego [85] showed that the ice crystal structure within a saline pore fluid environment is more fragile, which may be an additional cause for the lower resistance of saline soils compared to similar non-saline soils.
Dynamic Load	Recent progress in the dynamic characteristics of frozen soils was summarised by Zhao et al. [86]. Various tests have shown that a critical strain rate exists at which the dynamic strength is similar to the static strength. At higher strain rates, the dynamic strength is higher, with a slight decrease in peak strength with an increasing frequency of oscillation. Contrary behaviour was noted for lower strain rates. However, only a few data-sets are available, and more research is needed.
Refreezing	Arenson and Springman [67] present some tests during which the compression was stopped and broken bonds within the ice matrix were allowed to refreeze. Immediately after reloading, the resistance exceeded the values expected under comparable conditions with ongoing continuous loading. The resistance converged towards the continuous values following additional shearing with no obvious volume change. It is thought that the extra resistance is mobilised to break the refrozen ice bonds.

Figure 4.12. Table of variables that affect the strength of frozen ground. Adapted from [*Arenson et al.*, 2007].

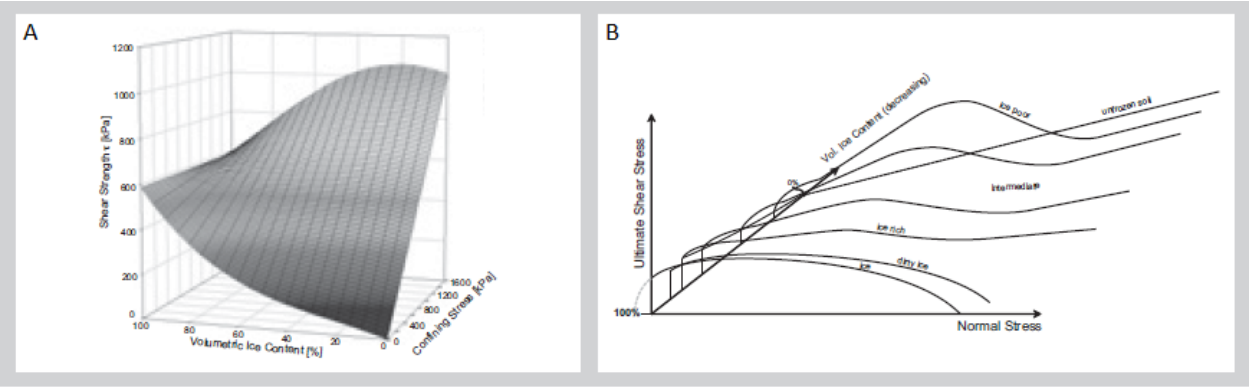

Figure 4.13. A) Post-peak shear strength for a sandy gravel at -2°C. B) Trends in the failure envelope for frozen soils at distinct temperature. Adapted from [*Arenson et al.*, 2007].

illustrated in Figure 4.13B:

(a) at low confinement stress, strength of the frozen material is higher than the strength of the unfrozen material due ice matrix cohesion

(b) the strength of pure ice is independent of the confining stress for low confining stress

(c) for unconfined compression, peak strength increases with decreasing ice content

(d) ultimate shear strength increases with a decrease of ice content

(e) at low normal stress, strain softening occurs

(f) at higher normal stress, strain hardening begins to occur

(g) at very high normal stress, pressure melting of ice occurs, and the unfrozen strength is reached, often resulting in a dramatic drop in resistance

Razbegin et al. [1996] review a significant amount of Soviet literature (128 references) and outline the major effects of temperature, moisture content, salinity, and cryotexture on the mechanical properties of frozen ground. Decreasing temperature is commonly known to increase a frozen soils strength and resistance, but below -50°C, a reduction in strength has been observed, possibly due to micro damage accumulation from variations in the coefficient of expansion/contraction among the mineral particles and ice matrix. In general, temperature affects cohesion to a greater degree than the angle of internal friction. *Razbegin et al.* [1996] presents a possible relationship between ultimate long term normal stress and temperature, as originally proposed by *Vyalov* [1959],

$$\sigma_{11} = \sigma_0 + B|T|^n \tag{4.2}$$

where B is a parameter, T is temperature in Celcius, and n is 0.5, or $n = 1$ for naturally compacted soils. Some moisture content has been observed to increase a frozen soil's strength until the moisture content approaches saturation. At saturation, soil strength begins to decrease with increasing moisture content. Cellular and laminar cryogenic texture that is oriented with respect to the applied load tends to have a strengthening effect, and is likened to basic notions for composite materials. Finally, salinity tends to weaken strength and increase creep deformation rates, most likely due to the freezing point depression which increases the expected moisture content relative to fresh pore fluid for a certain temperature.

Sayles & Carbee [1981] applied unconfined axial compressive stress at a rate of 0.005 per second to 45 samples of frozen silt from the Fairbanks permafrost tunnel at a temperature of -1.67°C. The test specimens appeared to fail plastically, where no visible evidence of cracking occurred until large strains had occurred. *Sayles & Carbee* [1981] found that there was a non-linear increase in axial compressive stress at the point of initial fracture with increasing volume of ice per unit volume of soil. They also found that there was a non-linear decrease in the axial compressive stress at the point of initial fracture with increasing dry unit weight of the samples. In general, the authors concluded that stress resistance of a saturated frozen silt with a range of total water content should be considered as consisting of the cohesion of the ice matrix, the frictional resistance of the soil grains, and the frictional resistance of the fractured ice crystals.

Agergaard & Ingeman-Nielsen [2012] performed laboratory tests on two fine-grained permafrost samples from Greenland to determine the shear strength as a function of temperature. The samples varied in ice content, from virtually no ice (0.1% by volume) to 33.5% by volume, and consisted of silty to very silty marine clays. In the tested temperature range (1°C to 3°C), *Agergaard & Ingeman-Nielsen* [2012] found that the shear strength decreases approximately 20% per degree temperature increase, relative to the shear strength at -3°C.

Kim et al. [2016] prepared two soil types (sand and weathered soil made up of gravel, silt, and clay) and investigated wave propagation and electrical resistivity through each soil sample in a temperature-controlled chamber. Using standard relationships between the compressional and shear wave velocities through the samples, *Kim et al.* [2016] determined the Youngs and shear moduli of the samples as a function of temperature. They found that both the Youngs and the shear modulus increased with decreasing temperature, but the sand samples moduli increased more rapidly than the weathered soil samples did.

Much knowledge has been accumulated on the strength of frozen ground through cold regions engineering projects, construction of infrastructure on permafrost ground, and mining operations involving artificially frozen ground. While the literature is vast, very few mathematical relationships exist that describe the changes in tensile strength, shear strength, and cohesion of ice and/or of frozen ground, with changes in temperature. Instead, relationships are described in terms of trends. This overwhelming limitation in our understanding may be due to site-specificity issues. Making the additional leap of applying temperature-strength relationships to the Arctic coastal erosion problem has not been accomplished to date, but intuitively shows promise to improve predictions of coastal erosion rates.

Observed Links Between Erosion Rates and Geomorphology

To date, no definitive set of geologic or geomorphic rules linked to coastal erosion rates has been developed and rigorously tested for the Arctic. *Lantuit et al.* [2011] suggest that the spatial variability of coastal erosion in the Arctic may be related to geomorphic conditions (Figure 4.14) and the temporal variability more related to hydrologic, thermal, and mechanical forcings. The wide variety of erosional processes confounds attempts to neatly correlate geologic/geomorphic conditions and erosion rates. Researchers agree that bedrock-lined coastlines in the Arctic erode more slowly than those comprised of unconsolidated sediment or permafrost (e.g., *Overduin et al.* [2014]). Furthermore, it is not uncommon for studies to suggest that ice-bonded fine-grain (e.g., silt and clay) bluffs are more susceptible to rapid erosion than ice-bound coarse-grain (e.g., sand and gravel) bluffs (e.g., *Harper* [1978]). Bluffs comprised of fine-grained materials commonly have narrow beaches because the eroded material will stay in suspension longer than coarse-grained material. The narrower beach may afford a greater opportunity for the ocean to reach the base of the cliff. Some studies suggest that tall bluffs are less susceptible to high erosion rates than short bluffs because of the greater (and more infrequently available) energies needed to transport the sediment (e.g., *Jones et al.* [2009]). Steep slopes also appear to be more susceptible to high erosion rates than shallow slopes due to the influence of gravity. The relative youth of a surface has been correlated to greater erosion rates. For example, *Mars & Houseknecht* [2007] found that recently exposed surfaces, such as a breached lake, exhibit higher erosion rates than those with mature vegetation. The presence or absence of offshore barrier islands has also been discussed relative to Arctic erosion (e.g., *Jorgenson & Brown* [2005]). Offshore islands reduce the wave energy available to erode the mainland compared to areas completely exposed to the open ocean. Similarly, coastlines oriented toward the prevailing direction of storm waves are expected to experience greater erosion rates than those in more sheltered areas (e.g., bays or lagoons).

Some studies have attempted to correlate observations of coastal erosion rates with permafrost properties or characteristics of the coastal geomorphology. *Hequette & Barnes* [1990] show only a weak correlation between retreat rate and the ground ice content ($r = 0.30$, see Figure 4.15) along the Canadian Beaufort Sea coast. They note, however, that if they included the cliffs along the Tuktoyaktuk Peninsula that contained massive ice, the correlation improved ($r = 0.62$). Interestingly, these authors did not feel it was justified to include cliffs which contained massive ice, because "they are virtually melting away," and therefore are not directly comparable to cliffs composed of sediments. Later studies do not make this distinction. *Hequette & Barnes* [1990] also show poor correlation between sediment grain size and retreat rate ($r = 0.08$) and between cliff height and retreat rate ($r = 0.29$). In general, the observation that erosion rate does not strongly depend on the sediment type or ice content within unlithified permafrost coastlines is because sediment cohesion is virtually null; the strength of the material comes almost exclusively from the ice bonding. Once the unlithified material has thawed, vulnerability to erosion increases dramatically.

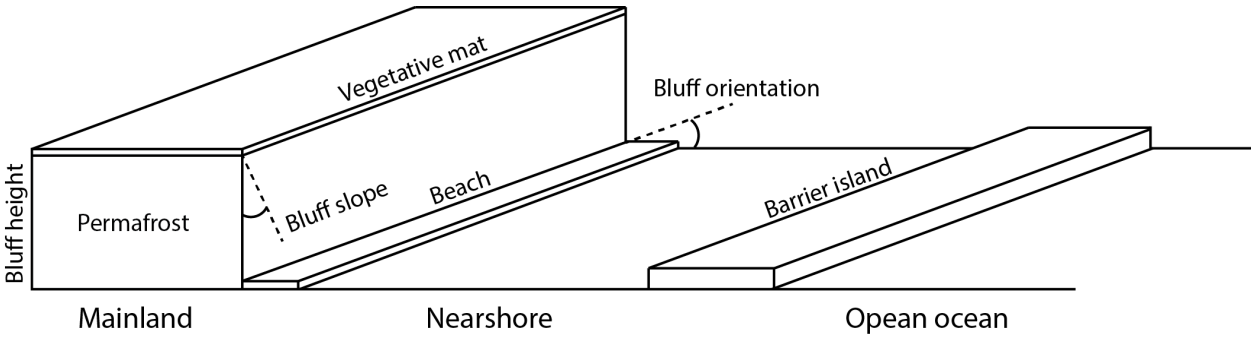

Figure 4.14. Schematic of geomorphic features for a frozen bluff considered relevant to the rate of coastal erosion in the Arctic. The primary factors include: presence/absence of a vegetative mat, permafrost texture, bluff height, bluff slope, bluff orientation, presence/absence of a beach, and presence/absence of a barrier island. Note: the active layer and ice wedging is not illustrated here because these characteristics have not yet been closely associated with erosion rates.

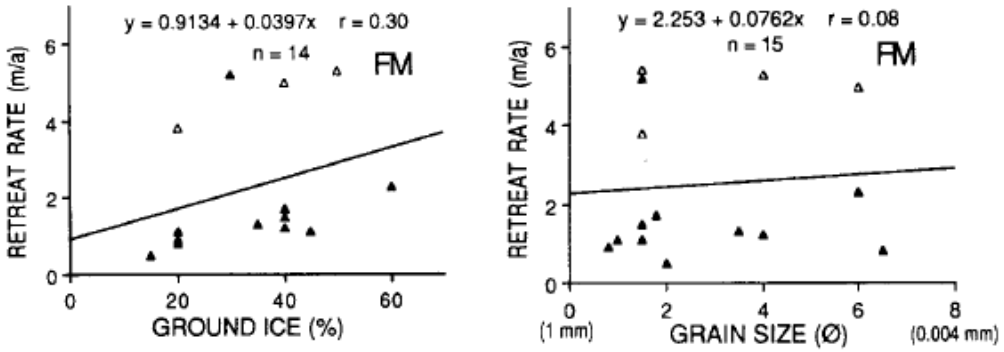

Figure 4.15. Weak correlations are observed between erosion rate with ground ice content, and erosion rate with grain size. Adapted from [*Hequette & Barnes*, 1990].

A study by *Dupeyrat et al.* [2011] located inland along the Lena River, which cuts into permafrost, quantified the effects of ice content and water flow on thaw and erosion of non-cohesive permafrost banks made of sand with laboratory experiments. While the study may not directly apply to coastal bluffs that contain clay or silt (because cohesion increases with increasing clay content), the study showed that erosion occurred episodically, with phases of thaw (where thaw thickness could be predicted by a thermal conduction model), and phases of ablation, where water mechanically removed the non-cohesive thawed sand. At

high ice content, the study found erosion rates depended very little on ground temperature, but strongly on water temperature.

Coastal type	Rate (m/yr)	Standard deviation	Site count	Lower quartile (m/yr)	Higher quartile (m/yr)
Accretional sand bar	0.40	0.56	22	0.00	0.60
Alas	1.02	1.38	115	0.35	1.10
Ice Complex cliff	0.47	0.46	255	0.00	0.69
Lagoon barrier	0.47	0.35	41	0.16	0.80
Retrogressive thaw slumps	0.91	0.75	60	0.28	1.35
Total	0.65	0.84	493	0.16	0.86

Figure 4.16. Erosion rates and geomorphology at Bykovsky Peninsula. Adapted from [*Lantuit et al.*, 2011].

In Siberia, at the Bykovsky Peninsula, erosion rates were found to be highly influenced by the geomorphology. Regions with alases (large depressions of the ground surface produced by thawing of very thick and exceedingly ice-rich permafrost) and retrogressive thaw slumps had the largest erosion rates (> 2 m yr^{-1}), while coastal cliffs, lagoons, and sand bars had decreasing erosion rates, respectively [*Lantuit et al.*, 2011]. The table in Figure 4.16 summarizes the observations at Bykovsky Peninsula. Because retrogressive thaw slumps and alases have already been affected by thermal denudation and have a lowered shore profile, these coastal geomorphologies were more susceptible to mechanical hydrodynamic erosional processes. *Günther et al.* [2013] found a correlation between mean daily air temperature and coastal erosion rate for a site in the central Laptev Sea that suggests coastal erosion rates increase 1.2 m yr^{-1} per degree Celcius increase in the mean.

At Simpson Point on Herschel Island, Canada, *Radosavljevic et al.* [2016] found erosion rates were highest in regions with the highest wave exposure and ice content, but also found very high retreat rates where soils were water logged in active drainage areas.

Chapter 5

Review of Existing Models

Numerical modeling is commonly used to simulate oceanographic conditions for use for the hindcast, nowcast, and forecast of coastal hazards (e.g., erosion), as well as the thermal state of permafrost ground. This section discusses wave, sea-ice, near-shore circulation, permafrost thermal, and permafrost erosion models. Many of these models are well established, but some highly parameterized models require simplifying assumptions that must be well understood that are discussed in the following sections.

Hydrodynamic Modeling

Wave Modeling: WAVEWATCH III®

Wave evolution, and thus the development of a sea state, is described by the radiative transfer equation, or the Boltzman equation, as follows [*Thomson et al.*, 2013],

$$\frac{\partial E(f,\theta)}{\partial t}\nabla \cdot (c_g E(f,\theta)) = S_{wind} - S_{brk} + S_{nl} - S_{ice} \tag{5.1}$$

where $E(f,\theta)$ is the two-dimensional wave energy spectrum dependent upon frequency f and direction θ, and c_g is the group velocity.

WAVEWATCH III® [*Tolman et al.*, 2013] is a community based spectral wave model that describes wave evolution at the desired spatial and temporal resolution in order to provide a frequency-direction spectrum that details the full sea state. This program is used by National Oceanic Atmospheric Administration (NOAA), the National Weather Service, National Centers for Environmental Prediction, and the U. S. Navy to predict future wave conditions four times per day. Each run starts with a 9-, 6-, and 3-hour hindcast and produces forecasts every 3 hours from the initial time out to 180 hours past the initial time. The wave model suite consists of global and regional nested grids.

The Naval Research Laboratory (NRL) has provided upgrades to the system to include curvilinear gridded domains to cover the Arctic Ocean. The multi-grid (or mosaic grid)

feature of WAVEWATCH III® allows for the two-way communication of energy across domain boundaries. With two-way communication, the predictions from the high-resolution model, potentially using better winds and better bathymetry, are shared with what could be considered the host domain and other high-resolution domains. In a recent version developed at NRL, it is now possible that domains with dissimilar grid types (e.g., curvilinear grids and regular grids) can be run together, passing wave energy across the boundaries in both directions.

Model features in WAVEWATCH III® include modular Fortran90 and highly scalable parallel programming, dynamic time-stepping, third-order propagation schemes, irregular grids, triangular grids, and two-way communication between domains. Model input mainly consists of wind and current fields combined with local bathymetry. Within the model, winds and currents are updated at every time step Δt_g and represent values at the end of the time step considered.

The model inputs include:

- wind
- current
- bathymetry (setting the water depth)
- sea surface temperature (air-sea temperature difference)
- ice concentration
- sediment median grain size

The model outputs include:

- Waves: Directional wave energy spectrum and parameters
- Atmosphere-Waves Layer: wind to wave energy and momentum flux
- Wave-Bottom Layer: energy dissipation and momentum loss at the bottom layer
- Wave-ocean Layer: energy and momentum flux between the ocean and wave layer

The model currently includes dynamically updated ice coverage, but ice covered sea is considered as land, assuming zero wave energy and boundary conditions at ice edges are identical to boundary conditions at shore lines. Given the prominence of this predictive code for short-term forecasts of ocean waves, it holds strong potential to additionally forecast ice concentration, thickness, and location of the ice edge.

Circulation Modeling: Delft3D

Delft3D-FLOW is an open source modular suite of numerical models written in Fortran and C programming languages for performing 2D and 3D hydrodynamic simulations of coastal, river, and estuarine environments. Being modular, it can be easily coupled with other Delft3D programs that simulate sediment transport, waves, morphological changes, and ice. A conceptual diagram of the components of the Delft3D modular package are shown in Figure 5.1. Since the Delft3D suite is open source, the scientific community is always applying new techniques to solve challenging problems and have incorporated the ability to track oil spills and even analyze the growth and effect of hydrodynamics on free floating ice forms. The general flow of a Delft3D-FLOW simulation with included modules is shown in Figure 5.2.

Figure 5.1. Delft3D suite of open source model components. Adapted from [*Deltares*, 2014].

Delft3D-FLOW is a free surface, terrain following, primitive equation model that solves the Navier-Stokes equation of motion, continuity equation, and the conservative tracer transport equations to simulate non-steady flow and transport on a rectangular or curvilinear boundary fitted grid. Delft3D-FLOW uses the Boussinesq approximation where the effect of variable water density is only used in the pressure term of the governing equations. Delft3D-FLOW applies the hydrostatic pressure equation where vertical accelerations are ignored. Delft3D-FLOW uses a staggered numerical grid that allows for simpler boundary conditions and prevents water level oscillations in the shallow water solvers. Delft3D-FLOW has the capability for domain decomposition. This allows for a multiple grids of varying spatial resolution to be used to limit the number of computational cells when high spatial resolution is required in an area of interest. Simulations can be performed in serial or parallel on PC or Linux computer architectures.

Delft3D-FLOW can simulate forcing from free surface gradients, Coriolis force, variable water density, horizontal density gradients, turbulence, head flux, tidal forcing, wind, atmospheric pressure, volumetric sources, radiation shear stresses, and wetting/drying, all of which are critical to Arctic coastal modeling applications. Sediment transport (Delft3D-SED) and morphology (Delft3D-MOR) modules, which are coupled to Delft3D-FLOW, simulate bed load transport of non-cohesive sediments, and suspended load transport of non-cohesive and cohesive sediments by solving the three dimensional advection-diffusion

equation. Burial of sediment and digging, the transfer of sediment upward in the bed, are in included in Delft3D-SED. The equation of state is updated to include the sediment concentration in the water column to compute density that can create horizontal density gradient driven flow due to sediment concentration gradients. The suspension, deposition, and advection of non-cohesive and cohesive sediments in Delft3D-SED is controlled by various user input sediment properties, dispersive transport, wave induced bed shear stress, and burial. The Delft3D sediment and morphology modules take inputs of sediment concentration at open boundaries and/or volumetric sources, grain size distributions, and strength properties of the sediment bed. Delft3D-MOR differs from Delft3D-SED in that as bed erosion or deposition takes place, the bathymetry is updated for the Delft3D-FLOW calculations. This is advantageous for simulations of sediment transport of longer time scales where bed changes would occur.

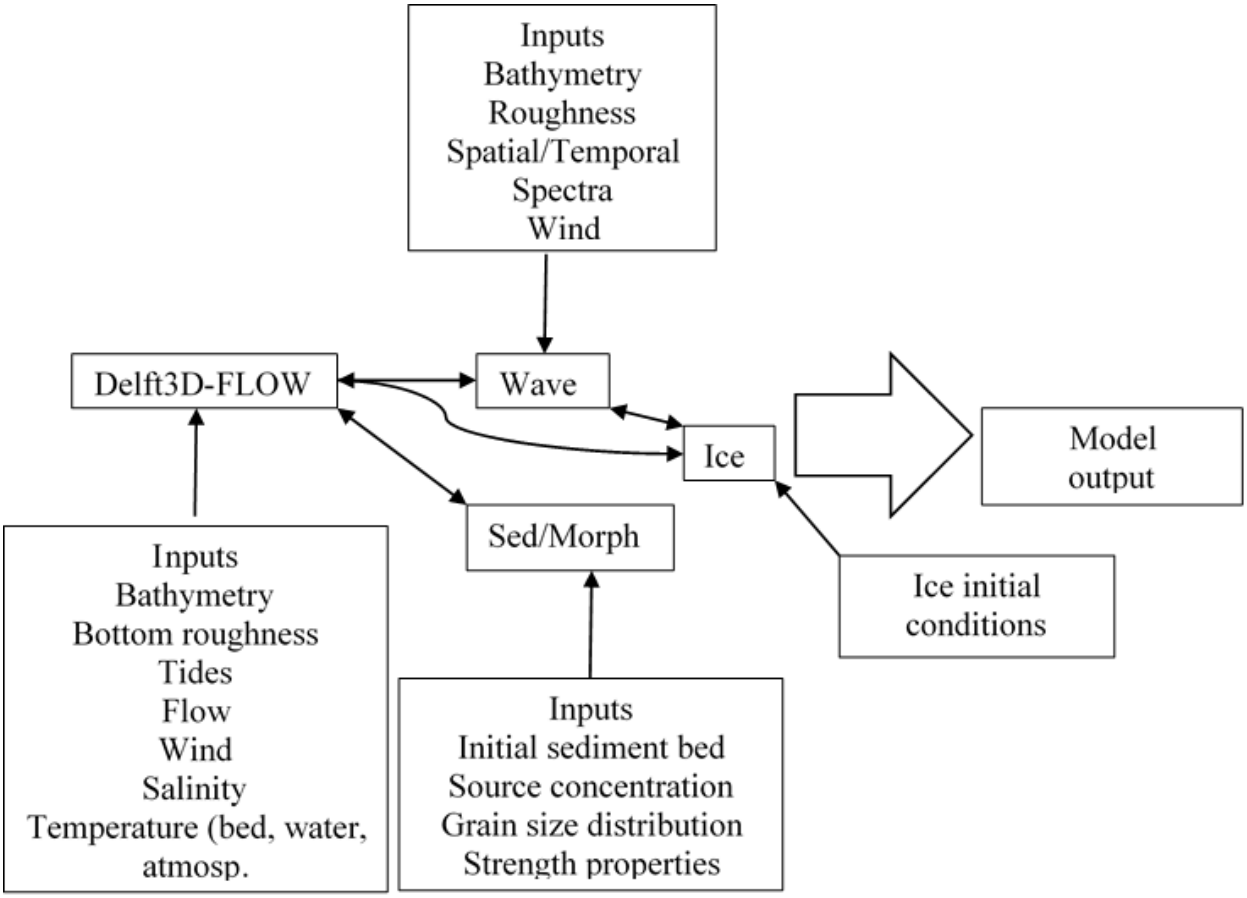

Figure 5.2. Conceptual flow chart of Delft3D-FLOW with wave, sed/morph, and ice modules.

Delft3D-WAVE uses SWAN (Simulating Waves Nearshore) as the wave model. SWAN is fully spectral and based on the discrete spectral action balance equation. SWAN computes refractive propagation and wave generation from wind, dissipation due to white-capping,

bottom friction and depth-induced wave breaking and non-linear wave-wave interactions explicitly with state-of-the-art formulations. SWAN uses a curvilinear grid and allows for better coupling with Delft3D-FLOW curvilinear grids. Radiation stresses computed in SWAN are fed back to the Delft3D-FLOW model by creating wave-induced currents and set up. These features of SWAN make it a very good tool for simulating waves in the nearshore environment while being coupled with a nearshore flow and sediment transport model.

The Delft3D modeling suite is uniquely suited to deal with the complex environmental features found in the Arctic. The investigation of circulation patterns, influence of stream runoff during ice melt, changes in sediment transport due to increased wave and storm activity can all be enhanced using the Delft3D suite of models.

The ability to couple models is extremely important when considering circulation. The effect of waves on circulation patterns and vice versa is an important process. This is especially true in the Arctic where decreasing levels of sea ice expose more ocean surface to the effect of wind, causing an increase in wave activity. The domain decomposition of Delft3D allows for the physical dynamics of the region around the study site to be accurately represented.

The increase in seasonal runoff from ice melt can affect coastal circulation patterns as well as sediment transport patterns. The Delft3D model suite was successfully applied to Tuktoyaktuk Harbor in the western Canadian Arctic to investigate sediment transport patterns due to the reduction in sea ice and increase in storm surge, wave height, and runoff [*Manson*, 2015]. Delft3D-SED can model the transport of both cohesive and non-cohesive sediments which is important in ensuring the erodibility and deposition of sediment is accurately represented. As more coastline becomes exposed and unfrozen, the erosion potential may increase causing exposure or burial of manmade structures. Understanding the sediment dynamics of the system is crucial to long term viability of Arctic development. Delft3D is well-equipped to address these questions.

An important feature of Delft3D is the ongoing development and incorporation of new techniques to solve unique problems. One example of this is the ongoing integration of an ice modeling module. Used for the estimation of ice flow movements, coverage extent, and thickness; the module can be linked to other models to investigate long term movements, growth, and potential effect on a study area. An example of this is shown by coupling the ice model and Delft3D-FLOW to investigate the movement of a free floating ice sheet in the coastal North Sea (Figure 5.3). The modeled ice sheet was forced by winds and currents, and its movement within the study area was tracked. This application is extremely useful in determining potential hazards for ship traffic, offshore structures such as exploratory wells, and existing or planned man-made structures.

The suite of Delft3D modeling packages are continually being developed and improved for use in the scientific community. This open source benefit and being modular makes Delft3D useful for modeling currents, waves, sediment transport, morphologic changes, water quality, and ice in a broad range of environments, including the Arctic.

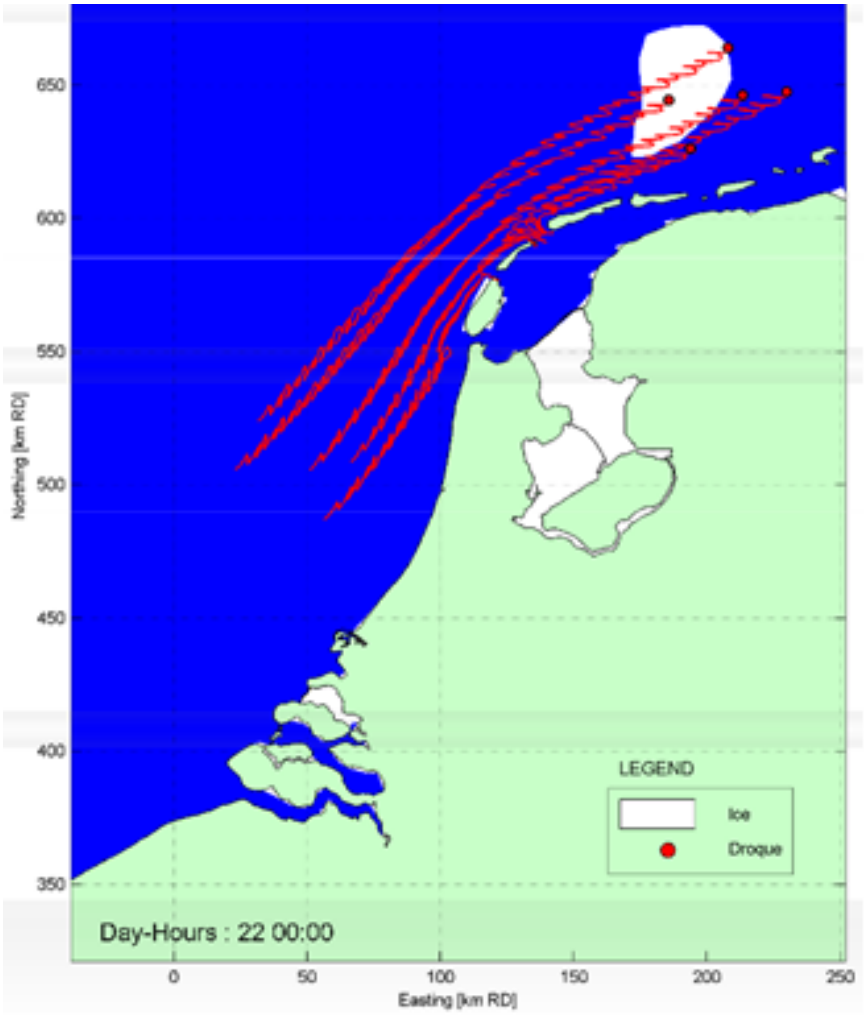

Figure 5.3. Path of modeled free floating ice-form and associated model drogues in the North Sea.

Sea-Ice Modeling

There are two fundamental categories of sea-ice: continuous sea-ice and assemblies of ice floes and cakes. Continuous sea-ice, or pack-ice, includes shore fast ice and is a large (semi-infinite) sheet, possibly with flaws (pressure ridges, cracks, or leads). The assembly of ice floes, or the marginal ice zone (MIZ), is a group of independent floating ice bodies that when evaluated as a whole represent a flexible ice system.

In the case of pack-ice, the distance the ice sheet covers is many orders of magnitude larger than typical incoming wavelengths, while the ice thickness is many orders of magnitude smaller. This geometrical relationship allows for plate theories to be the mathematical basis of sea-ice models. In plate models, the strain and deformations induced by passing waves is

modeled using a thin elastic sheet. The internal stresses are the most important forcing terms on the integrity of the pack-ice. Discontinuities within the sheet (pressure ridges, cracks, leads, or changes in ice thickness) result in increased dissipation and scattering [*Squire*, 2007]. Further, incorporation of draft and changes in draft is quite important, yet there is a dearth of three dimensional treatment in the scientific literature [*Squire*, 2007] as compared to a zero-draft treatment. Hence, accurate knowledge of the ice sheet geometry is needed to accurately model the interactions between waves and pack-ice.

The assemblies of ice floes are often the portion of ice cover that is closest to the open ocean, hence their designation as the marginal ice zone. This is a very dynamic region in which the spatial and temporal ice distribution changes dramatically by shifts in waves, wind, and current. In the case of the ice floes in the MIZ, their sizes are on the order of wavelengths, or smaller, due to wave-induced ice breakage. Since ice floes can move when forced by waves, internal stresses tend to be of less importance unless there are floe-floe contact forces. Modeling of wave effects in the MIZ has taken two tracks: (i) modeling of discrete ice blocks, or (ii) modeling the ice as a continuum with particular rheological properties [*Squire*, 2007]. Regardless of the modeling track, knowledge of the floe size distribution (FSD) is needed.

There are three types of mathematical treatments that are currently being developed to model sea-ice for distinct purposes (see Figure 3.6):

- Wave-ice interaction models that capture the ice geometry dependent scattering and dissipation accompanying wave propagation
- Weather and storm ocean-ice models that couple atmospheric forcing with wave development in the presence of ice with non-specific geometries, and rough scattering and dissipation estimates of the wave propagation within the non-specific ice geometries
- Earth system models that couple atmospheric forcing with ice pack velocities and heat flux changes over years to understand gross effects of sea-ice on climate

Wave-ice interaction models focus on the underlying physics of waves interacting with rigid structures. These interactions form the fundamental basis for all other models, but due to computational and geometric initialization requirements, these models have yet to be incorporated into more comprehensive models. The weather and storm models are needed for predictive short term forecasts that can assist in shipping, search and rescue operations, and other operations. Given the strong interplay between sea-ice and waves, accurate models offering short term forecasts must include wave-ice interactions on an aggregated level. Finally, climate based modeling is governed primarily by heat fluxes, namely, radiative, reflective, or capacitive in nature. The sea-ice in the Arctic plays a major role in the overall radiation budget of the Earth. And although the wave-ice interaction models are fundamental to the evolution of sea-ice coverage and temperatures of the water in the Arctic, the only parameters that climate scale models utilize are based around ice thickness and pack ice dynamics (velocity and heat flux).

Wave-Ice Interaction Models

Energy exchange between waves and ice involves the scattering and dissipation of wave energy and excitation of the ice into oscillation modes. Scattering is an energy conserving event in which direction and amplitude are altered without depleting the mean wave energy. Dissipation is non-energy conserving and identifies the alteration of the group velocity (wave number). *Rogers et al.* [2011] suggests there are four classes of wave-ice interaction theories as detailed below.

Viscous In the viscous model, the ice layer is composed of many small ice floes and is treated as a liquid suspension. The liquid suspension has an effective viscosity much greater than that of water and a density slightly less than that of water. In this manner, a finite depth, two-layer model, was developed by *Keller* [1998]. The upper layer (grease ice) has a constant viscosity, and represents an immiscible fluid overlying a denser but inviscid lower layer (seawater). Solution of this system yields a dispersion equation that exhibits dispersion and attenuation that is dependent upon the effective viscosity of the suspension (water is modeled as inviscid). The large viscosity of the upper layer, as fit experimentally by *Newyear & Martin* [1999], causes wave damping that increases with wave frequency. Hence the ice, through the viscous term, acts as a low pass filter for waves in this model.

The viscous model is not dependent upon a geometric description of the upper layer - only that the upper layer is homogeneous in its viscosity. This homogeneity in viscosity arises from the interaction on the underside of the ice floes in which bonds between crystals are mechanically agitated by the waves [*Martin &Kauffman*, 1981] and the roughness increases due to clumping of ice crystals.

Viscoelastic In the viscoelastic model, the ice layer is again viewed as a liquid suspension, with an effective viscosity much greater than that of water and a density slightly less than that of water. However in the viscoelastic case, elasticity is introduced to acknowledge that an ice floe field can encompass a distance that is much greater than a wavelength [*Wang & Shen*, 2010]. In this manner, the viscoelastic model is comprehensive in that it can describe wave propagation into all types of ice cover and allowing for a smooth transition from ice edge to interior pack ice.

Similarly, the viscoelastic model yields a dispersion relation which now contains several propagating wave modes under the ice cover [*Wang & Shen*, 2010]. A dominant wave mode can be selected with the following criteria: (1) the wave number is the closest to the open water value and (2) attenuation rate is the least among all modes.

Scattering Superposition of individual scattering events off geometrically identified ice floes form the basis of the scattering model [*Perrie & Hu*, 1996]. Scattering is determined by ice floe diameter, thickness, and distribution of individual elements within an area. At-

tenuation in the scattering model is determined by the decay rate of the spectral wave energy as waves propagate from the open ocean into ice covered waters. Attenuation is based on wave frequency, ice cover concentration, ice floe diameter, floe thickness, distance from the ice edge, wind speed, and wave age. When ice is absent, attenuation is negative and waves are generated and grow in this model as one would expect. However when ice is present, this model shows strong attenuation for high frequency waves, small floe diameter, and large ice concentration.

Turbulence The last method identified by *Rogers et al.* [2011] for representing wave-ice interaction is based on the work by *Liu & Mollo-Christensen* [1988] and *Liu et al.* [1991]. This is a model for attenuation by a sea-ice cover, derived on the assumption that dissipation is caused by turbulence in the boundary layer between the ice floes and the water layer. Here again, the ice is modeled as a continuous thin elastic plate. Input ice parameters are ice thickness (in meters) and an eddy viscosity in the turbulent boundary layer beneath the ice, ν.

These fundamental physical models are generally developed using the support of the National Science Foundation or the Office of Naval Research (or their equivalents in other countries), and tend to be focused on basic research themes.

Ocean-Ice Models (Weather and Storms)

The transference from an wave-ice interaction model to an ocean-ice interaction model is primarily dependent upon the spatial and time scales involved. The ocean-ice model includes the forcing effects that generate waves as well as the propagation characteristics of the resulting waves. These spatial scales are larger (kilometers to tens of kilometers) and the time scales over which they propagate are on the order of hours. Given these new scales, it may not be possible to have direct knowledge of many of the parameters that are needed in wave-ice interaction models like ice floe distribution, ice floe diameter, ice flow thickness, etc.

Model development is actively being pursued in this area. The Office of Naval Research‘s Arctic and Global Prediction Program has supported two complimentary five year Departmental Research Initiative (DRI) programs. The first DRI is focused only on the marginal ice zone [*Lee et al.*, 2012] and the second is focused on the evaluation of the full physics of the problem [*Thomson et al.*, 2013]. These programs are being specifically developed with the intention of bringing the appropriate sea-ice modeling techniques into Arctic system models, which include operational based wave models. As mentioned previously, NOAA, the National Weather Service, the National Centers for Environmental Prediction, and the U. S. Navy all use WAVEWATCH III® as their operational wave model. Therefore, focusing efforts on including ice into ice-ocean models is preferential. The physics program is focusing on developing an understanding of the following four key areas [*Thomson et al.*, 2013]:

- Identifying factors affecting the spatial and temporal variability of the sea state and improving forecasting of waves on the open ocean and in the marginal ice zone
- Improving the theory of wave attenuation and wave scattering in the sea-ice cover
- Using wave scattering theory directly in integrated Arctic system models, and indirectly to define an ice rheology for use in Arctic system models
- Better understanding the physics of heat and mass transfer from the ocean to the atmosphere, and the seasonal variability of fluxes during summer ice retreat and autumn ice advance

In ocean-ice models, an aggregated approach has thus far been taken in which proxies for the ice floe distribution, floe diameter, and thickness can be employed. Ice concentration measurements are a main driver in these models and mathematical attempts have been made to integrate some of the less geometry dependent wave-ice interactions models. For instance, nonconservative source terms have been developed for both the turbulence model by *Liu et al.* [1991] and the viscoelastic model by *Wang & Shen* [2010]. These have been integrated into WAVEWATCH III®, but scattering, a conservative process, is not yet considered. By including multiple viscosities based on ice floe distribution, the viscoelastic model by *Wang & Shen* [2010] may be empirically improved to produce realistic interactions [*Thomson et al.*, 2013].

Since *Stopa et al.* [2016] have identified that wave attenuation in the Arctic may be dominated by other processes than under-ice friction (i.e. attenuation), it is important that a more physical approach to modeling wave-ice interactions is taken at the ocean-ice scale. Thus, while there is active research in this area, and attempts have been made to integrate some of the wave-ice interaction models, there is still much work to be done and many contributions to be made.

Research in the following areas could have a large impact on Arctic sea-ice prediction:

- Understanding the influence that the marginal ice zone (i.e. partially ice covered waters) has on fetch and hence the ability to generate waves
- Understanding wave dissipation and scattering due to interactions with ice
- Understanding of the influence of wave energy on the break-up of ice both at the marginal ice zone (wind waves) and deep within ice-sheets (swell waves).

As identified by *Thomson et al.* [2013], the primary shortcoming of all models developed so far is that they either assume that the energy is conserved or they impose an arbitrary dissipation based on a non-measurable parameter. The most significant unanswered question is to determine the process or processes by which energy is dissipated as it propagates through a field of broken ice.

These coupled ocean-ice models are extremely important for anyone working in the Arctic: U. S. Coast Guard, U.S. Navy, industrial workers, the tourist industry, shipping industry, and indigenous communities. Coupled ocean-ice models are needed to accurately forecast the magnitudes of storms and the probabilistic sea-ice concentration to be encountered.

Sea-Ice in Earth System Models

Sea-ice models used in coupled Earth system models treat the ice as a continuum and solve a momentum equation that predicts the ice motion due to forcing by atmospheric winds, ocean current, and Coriolis forces. Additional equations solved include the heat equation, which governs water-ice phase change due to ocean and atmospheric heat fluxes, and an equation for the evolution of a sub-grid-scale ice thickness distribution. The Los Alamos National Laboratory sea-ice model, *CICE* [*Hunke & Lipscomb*, 2006], is a state-of-the-art model developed as the sea-ice component in the Community Earth System Model (CESM), and is also the foundation of the *MPAS-CICE* model developed for the ACME project. It has also been used as part of the Regional Arctic System Model (*RASM*), funded by DOE and developed to look at interactions between ice-ocean-atmosphere in the Arctic on decadal time scales.

Pack-ice typically consists of rigid plates, which may drift freely in areas of relatively open water, or be closely packed together in regions of high ice concentration. A model of sea-ice dynamics predicts the movement of the ice-pack based on winds, ocean currents, and a model of the material strength of the ice. As the age or thickness distribution has shifted towards lower values, sea-ice drift speed increases and the ice cover becomes more mobile [*Rampal et al.*, 2009]. The model treats the ice-pack as a viscoplastic material that flows plastically under typical stress conditions but behaves as a linear viscous fluid where strain rates are small and the ice becomes nearly rigid. The continuum mediates stress transfer between the atmospheric boundary layer above and the oceanic boundary layer below the ice with ridging and snowdrifts determining the turbulent roughness of the ice surface. Nonuniform motion of the ice is responsible for the thickness and extent of the ice pack, which in turn influences the exchange of energy between the atmosphere and polar oceans.

The success of *CICE* in climate modeling studies has led to the model being adopted for use in shorter term ice forecasting. In the Naval Research Lab (NRL) Arctic Cap Nowcast/Forecast System (*ACNFS*), *CICE* is coupled with the Hybrid Coordinate Ocean Model (*HYCOM*) for nowcast and five data forecast predictions [*Posey et al.*, 2015]. *CICE* is also the main component of the Canadian Regional Ice Prediction System (*RIPS*), which uses the internal *CICE* simple mixed-layer ocean model, rather than coupling to a full ocean model for computational efficiency [*Lemieux et al.*, 2016]. In both of these forecasting models, ice concentration is assimilated using the 3D-Var method and lower skill is seen during the melt period particularly near the ice edge. The lower skill of models near the ice edge is primarily due to processes, particularly the effects of wave-ice interactions, that are not well-represented in the models. One possible way to introduce the effects of wave-ice interactions into a continuum model like *CICE* would be to incorporate an ice floe size distribution

similar to an ice thickness distribution. A theory for an ice floe distribution has recently been developed that includes redistribution of floe size due to wave induced breakup by *Zhang et al.* [2015].

CICE and other continuum sea-ice models also have limitations in the rheology used to determine ice internal forces, which is typically assumed to be isotropic. Satellite data indicate that sea-ice deformation is focused into narrow linear bands and overall the ice behaves anisotropically *Coon et al.* [2007]. There have been a number of anisotropic rheologies developed in recent years *Wilchinsky & Feltham* [2004]; *Schreyer et al.* [2006]; *Girard et al.* [2011], but they have not shown significant improvement over the standard isotropic rheology for low-resolution Arctic basin wide simulations. It is possible that the anisotropic deformation focused into narrow leads dominates the behavior, particularly at high resolution. Therefore, it may be more important for forecasting, where lead size and location can be important, than for climate simulations. A Lagrangian particle ice model that includes an anisotropic rheology has shown some promise in modeling sea-ice leads in a relatively high resolution simulation in the Beaufort Sea *Sulsky & Peterson* [2011].

Earth system models are extremely important in determining long term trends like sea level rise, average temperature changes in given regions, and changes in global circulation patterns that determine precipitation and other characteristics. For these reasons, NASA, the Department of Energy, and the military are all invested in Earth system models.

Permafrost Thermal Models

Current numerical permafrost models generally fall into one of two groups. The first group of models are subsurface heat and mass transfer models that can simulate freeze-thaw processes and are based on mathematical, first-principle, physical equations (i.e. the energy equation, Darcy's Law, etc.). The most advanced of this first group of models couples phase change with fluid flow, or so called *thermo-hydro* modeling. Owing to their complexity, this first group of models is limited to small domains, simulating at the regional scale ($\sim$km^3), and predictions are of high quality when compared to local observations. The second group of models are called Earth system models. These types of models are large in scale, often able to simulate processes over an entire continent, or the entire circum-Arctic. The grid cells tend to be very large (at minimum, regional scale), making up a coarse grid. The physical equations tend to be parameterized due to the vast scale Earth system models simulate, and they are directed towards adequately providing the lower boundary for atmospheric transfer schemes (i.e., the surface fluxes of radiation, momentum, and sensible and latent heat) in global climate models [*Westermann et al.*, 2016]. More error is expected with Earth system models when compared to local observations, but predictions or trends can be appreciated over wide areas, on a global perspective.

Because permafrost is solely defined by the ground temperature, the energy equation is the typical mathematical model used. The three dimensional equation for heat flow under

transient conditions is,

$$C\left(\frac{\partial T}{\partial t} + \nabla \cdot (uT)\right) = \nabla \cdot (\mathbf{K} \cdot \nabla T) \tag{5.2}$$

where K is the thermal conductivity of the ground (typically a mixture model of conductivity for rock, ice, and liquid water), T is temperature, and u if fluid velocity. The parameter C accounts for phase change when the ground undergoes freezing and thawing (important in the active layer, for example),

$$C = \sum x_i \rho_i c_i + L\left(\frac{\partial \Theta_u}{\partial T}\right) \tag{5.3}$$

where the subscript i indicates the component changing phase, x is the volume fraction, ρ is the density, c is the specific heat, L is the volumetric latent heat of fusion, and Θ_u is the volumetric unfrozen water content. A review of recent modeling advances is provided by *Riseborough et al.* [2008].

Typically, an energy balance helps formulate the boundary conditions applied. The parameters often specified at the boundaries include: the local geothermal heat flux from below, the mean annual air temperature from above, and incoming and outgoing shortwave radiation [*Westermann et al.*, 2016]. If temperature evolution is studied on a shorter-term, seasonal or daily temperature and radiation boundary conditions can be applied at the surface. Snow depth is typically considered as well, because of its insulation properties between the ground and the atmosphere. More complicated models may include the effects of differing ground conditions, such as vegetation, forest floor, moss, or peat layers [*Zhang et al.*, 2006]. As modeling advances, some researchers have included hydrologic effects as well [*Walvoord & Kurylyk*, 2016; *Westermann et al.*, 2016], although this is less common.

The InterFROST Model Inter-comparison Study

The InterFROST Project is a numerical model inter-comparison study which benchmarks several thermo-hydro coupled codes [*Grenier et al.*, 2016]. It provides an excellent overview of the currently available models which can simulate freeze-thaw processes specifically designed to model permafrost, with or without considering fluid flow effects. To date, a total of fourteen codes (and their development teams) have participated, including: Cast3M (Laboratoire des Sciences du Climat et de l'Environnement, France), permaFOAM (with OpenFOAM®, Gosciences Environnement Toulouse, France), GINETTE (Sorbonne Universités and Mines de Paris Paristech, France), HydroGeosphere (Université Laval, Canada), Smoker/Heatflow3D (Université Laval, Canada), SUTRA (Université McGill, Canada and USGS), DARCYTOOLS (SKB, Sweden), MARSFLO (Stockholm University, Sweden), MELT (Desert Research Institute, USA), PFLOTRAN (Oak Ridge National Lab and Sandia National Laboratories, USA), FEFLOW (Technische Universität

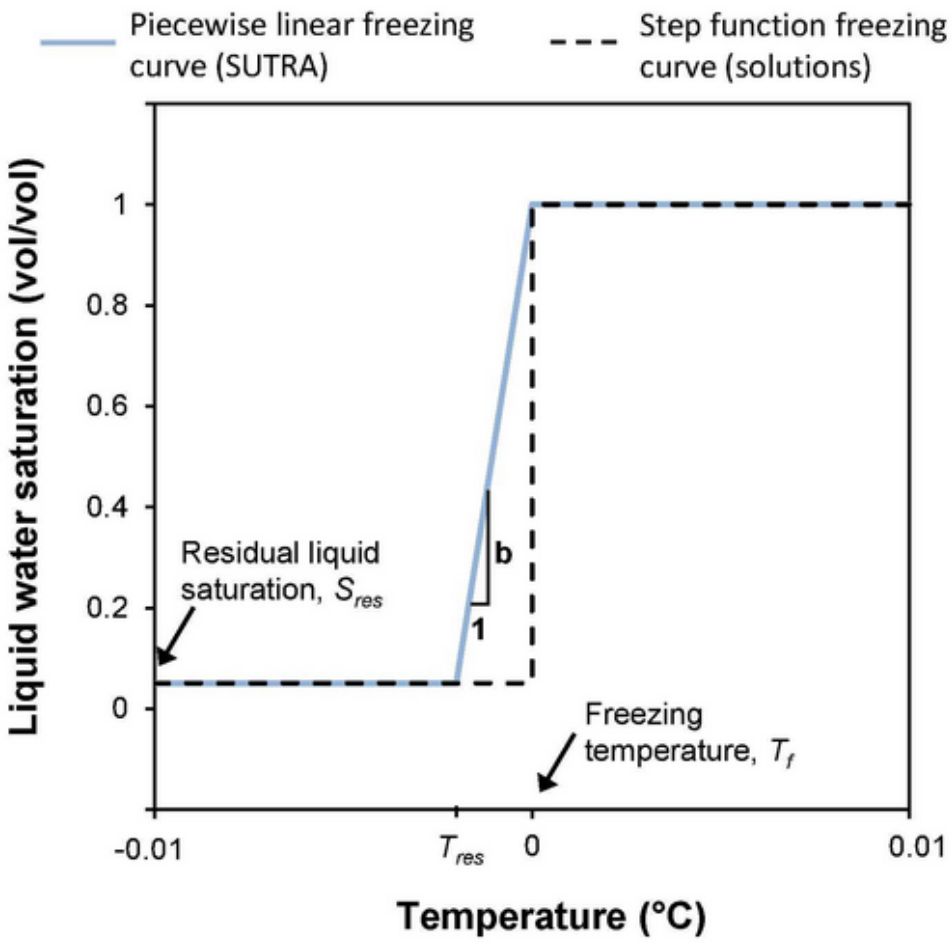

Figure 5.4. A simple linear freezing curve which describes how the unfrozen water content changes with temperature during phase change. [*Grenier et al.*, 2016].

Darmstadt, Germany), COMSOL (as implemented by the British Geological Survey, Great Britain), FlexPDE (Wageningen University, Netherlands), and ATS (Los Alamos National Laboratory, USA).

All of the models included in the InterFROST Project solve for the temperature according to (5.2), and fluid flow according to Darcy's Law, assuming saturated conditions. Specific, but typical, freeze-thaw curves are given to all participants to implement, and define the term $\frac{\partial \Theta_u}{\partial T}$ in (5.3). For example, many models use a simple linearly deceasing unfrozen water content between a narrow temperature range in which phase change occurs, accounting for a residual or minimum unfrozen water content (Figure 5.4). More complex freezing curves can also be used (see the parameter Water Saturation in Figure 5.5) that bias phase change towards a subset of the freezing interval.

Symbol	Description	Value or expression	Unit
ϵ	Porosity	0.37	$(-)$
β	Compressibility	10^{-8}	Pa^{-1}
g	Acceleration of Gravity	9.81	$m.s^{-2}$
λ_w	Water thermal conductivity	0.6	$W.m^{-1}.K^{-1}$
λ_i	Ice thermal conductivity	2.14	$W.m^{-1}.K^{-1}$
λ_s	Solid matrix thermal conductivity	9	$W.m^{-1}.K^{-1}$
λ_{eq}	Equivalent thermal conductivity	$\epsilon\big(S_w\lambda_w + (1-S_w)\lambda_i\big) + (1-\epsilon)\lambda_s$	$W.m^{-1}.K^{-1}$
C_w	Water Heat capacity	4182	$J.kg^{-1}.K^{-1}$
C_i	Ice Heat capacity	2060	$J.kg^{-1}.K^{-1}$
C_s	Solid matrix heat capacity	835	$J.kg^{-1}.K^{-1}$
ρ_w	Water volumetric mass	1000	$kg.m^{-3}$
ρ_i	Ice volumetric mass	920	$kg.m^{-3}$
ρ_s	Solid matrix volumetric mass	2650	$kg.m^{-3}$
$(\rho C)_{eq}$	Equivalent volumetric Heat capacity	$\epsilon\big(S_w\rho_w C_w + (1-S_w)\rho_i C_i\big) + (1-\epsilon)\rho_s C_s$	$J.m^{-3}.K^{-1}$
μ	Water dynamic viscosity	$1.793\,10^{-3}$	$kg.m^{-1}.s^{-1}$
L	Latent heat	$3.34\,10^{5}$	$J.kg^{-1}$
$S_w(T)$	Water saturation for $T \geq 273.15$	1	$(-)$
$S_w(T)$	Water saturation for $T < 273.15$	$(1-S_{wres})e^{-((T-273.15)/W)^2} + S_{wres}$	$(-)$
S_{wres}	Residual saturation in $S_w(T)$	0.05	$(-)$
W	Parameter in $S_w(T)$	0.5	K
K_w	Permeability	$k_r k_{int}\rho_w g/\mu$	$m.s^{-1}$
k_{int}	Intrinsic permeability	$1.3\,10^{-10}$	m^2
$k_r(S_w)$	Relative permeability	$10^{-\Omega\epsilon(1-S_w)}$ if $k_r(S_w) > 10^{-6}$	$(-)$
$k_r(S_w)$	Relative permeability	10^{-6} if $k_r(S_w) \leq 10^{-6}$	$(-)$
Ω	Impedance factor	50	$(-)$

Figure 5.5. A table of required parameters for the InterFROST Project permafrost models. [*Grenier et al.*, 2016].

The numerical method and algorithms used to solve the energy equation for temperature and/or Darcy's Law for fluid flow vary among the InterFROST Project models. Based on a questionnaire collected from most project participants, some codes implemented the finite volume method (MELT, PFLOTRAN, DARCYTOOLS, GINETTE, permaFOAM), while others used the finite difference method (ATS, COMSOL), the finite element method (Heatflow3D), or a hybrid approach of finite element and integrated finite difference methods (SUTRA). All of the models can represent either two dimensions (GINETTE, MELT) or up to three dimensions (Heatflow3D, PFLOTRAN, permaFOAM, COMSOL, ATS, DARCYTOOLS, SUTRA). These models typically simulate regional scale domains ($\sim$km^2-km^3) or smaller. Grid cell sizes are on the order of ($\sim$cm^2-cm^3 to $\sim$m^2-m^3).

As shown in Figure 5.5, several parameters are required to run these models. Many of these parameters are difficult to measure without detailed and extensive field work, such as the porosity, or the thermal conductivity values for the ground. If it is suspected that fluid flow may be significantly affecting the thermal regime, one additionally needs flow boundary conditions, fluid properties, as well as permeability values for the ground. How permeability

changes with ice content is highly parameterized, and depends greatly on the distribution of ground ice. While such models can provide very accurate predictions of the thermal and flow regimes, the ground conditions must be known (or reasonable guesses must be provided). This is difficult, if not impossible, except for very well studied sites. Therefore, an alternative approach may be to use parameterized models on a larger scale, such as Earth system models.

Earth System Permafrost Models

Much effort has been put towards permafrost modeling on a large, global scale through the coupling of atmosphere-ocean-land surface models. The Coupled Model Intercomparison Project phase 5 (CMIP5) described in *Koven et al.* [2013] provides another excellent review of the existing Earth system permafrost models. A table of each model that participated in the project is shown in Figure 5.6. These models make up a representative set of global coupled models that are being used as an integral component of the Intergovernmental Panel on Climate Change Fifth Assessment Report.

The table in Figure 5.6 reveals many differences between the Earth system permafrost models. For example, some account for snow cover, while others do not. Of the models that account for snow cover, some consider multiple snow layers, while others have a single layer. Organic matter in the ground is treated differently among models, while some do not consider organic matter at all. Most account for the latent heat during phase change, but a few models do not. Similarly, most models assign a different thermal conductivity to frozen vs. unfrozen ground. Beyond this table, *Koven et al.* [2013] do not further distinguish similarities or differences among the models; rather, the authors inter-compare the model results and predictions. Figure 5.7 provides a comparison of the permafrost extent predicted by each of the CMIP5 models using the current climate forcing (years 2005-2015 from the RCP4.5 scenario). The last plot shown is the observed permafrost extent. Also shown in thick blue lines are the 0° C isotherm in mean annual air temperature for each of the models over the same time period. The isotherm differs in each model, which lead *Koven et al.* [2013] to conclude that differences in the permafrost extent lie fundamentally in the modeled soil thermal regimes or in the atmosphere to soil energy exchanges.

Developed at the Vrije University Amsterdam, VAMPERS [*Kitover et al.*, 2015] is a permafrost model which calculates deep one-dimensional heat conduction with phase change to predict permafrost and active layer thickness and temperature. It has been designed to couple with iLOVECLIM, an Earth system climate model described in *Goosse et al.* [2010]. iLOVECLIM is built up of five coupled components, including an atmosphere, vegetation, carbon and geochemical cycle, ocean and sea-ice, and ice sheet models. VAMPERS is coupled to the atmosphere component of iLOVECLIM and runs on 4 hour time steps to parallel the time discretization of the atmospheric component's timescale.

VAMPERS also considers snow cover. In the VAMPERS model, each snowfall event adds to the current snow thickness, which is subsequently compacted. The compacted snow composes several layers in the model, and becomes integrated into the heat conduction

TABLE 1. List of models used in this analysis, the modeling groups that developed them, model attributes, and references. The model attributes listed here are relevant to soil physics at high latitudes, including whether the model includes a multilayer snow model, whether the snow acts to insulate between the soil and atmosphere, the inclusion of soil water latent heat and differing frozen- and unfrozen-soil thermal conductivity, and whether soil physical properties are effected by geographically varying soil organic matter.

Model name	Modeling group	Land model	Multiple snow layers	Snow between soil and atmosphere	Latent heat of soil water	Differing frozen/unfrozen soil thermal conductivity	Organic matter	Reference
BCC-CSM1-1	BCC	BCC Atmosphere-Vegetation Interaction Model (BCC_AVIM1.0)	Yes	Yes	Yes	Yes	No	Ji (1995)
CCSM4.0	NCAR	CLM4	Yes	Yes	Yes	Yes	Yes	Lawrence et al. (2011)
CESM1-CAM5	NCAR	CLM4	Yes	Yes	Yes	Yes	Yes	Lawrence et al. (2011)
CanESM2	Canadian Centre for Climate Modelling and Analysis (CCCMA)	Canadian Land Surface Scheme (CLASS)	No	Yes	Yes	Yes	No	Verseghy (1991)
GFDL-ESM with GOLD ocean component (2G)	GFDL	GFDL Land Model 3.0 (LM3.0)	Yes	Yes	Yes	Yes	No	Dunnea et al. (2012)
GFDL-ESM with MOM4 ocean component (2M)	GFDL	GFDL LM3.0	Yes	Yes	Yes	Yes	No	Dunnea et al. (2012)
GISS Model E coupled with Russell ocean model (E2-R)	Goddard Institute for Space Studies (GISS)	GISS Land Surface Model	Yes	Yes	Yes	Yes	Yes	Rosenzweig and Abramopoulos (1997)
HadCM3	Met Office Hadley Centre (MOHC)	MOSES	No	No	Yes	Yes	No	Cox et al. (1999)
HadGEM2-CC	MOHC	MOSES2	No	No	Yes	Yes	No	Essery et al. (2003)
HadGEM2 Earth System (ES)	MOHC	MOSES2	No	No	Yes	Yes	No	Essery et al. (2003)
INM-CM4	INM	INM-CM4	Yes	Yes	Yes	Yes	Yes	Volodin et al. (2010)
IPSL-CM5 Coupled with NEMO (A) Low Resolution (LR)	IPSL	ORCHIDEE	Yes	No	No	No	No	Krinner et al. (2005)
IPSL-CM5A Medium Resolution (MR)	IPSL	ORCHIDEE	Yes	No	No	No	No	Krinner et al. (2005)
MIROC-ESM Chemistry Coupled (CHEM)	Japan Agency for Marine-Earth Science and Technology (JAMSTEC)	Minimal Advanced Treatments of Surface Interaction and Runoff (MATSIRO)	Yes	Yes	Yes	No	No	Takata et al. (2003)
MIROC-ESM	JAMSTEC	MATSIRO	Yes	Yes	Yes	No	No	Takata et al. (2003)
MIROC5	JAMSTEC	MATSIRO	Yes	Yes	Yes	No	No	Takata et al. (2003)
MPI-ESM-LR	Max Planck Institute for Meteorology	JSBACH	Yes	No	No	No	Yes	Raddatz et al. (2007)
MRI-CGCM3	MRI	Hydrology, Atmosphere and Land (HAL)	Yes	Yes	Yes	Yes	No	Yukimoto et al. (2012)
NorESM1-M	Norwegian Climate Centre (NCC)	CLM3	Yes	Yes	Yes	Yes	Yes	Lawrence et al. (2011)

Figure 5.6. The Earth system permafrost models compared by [*Koven et al.*, 2013].

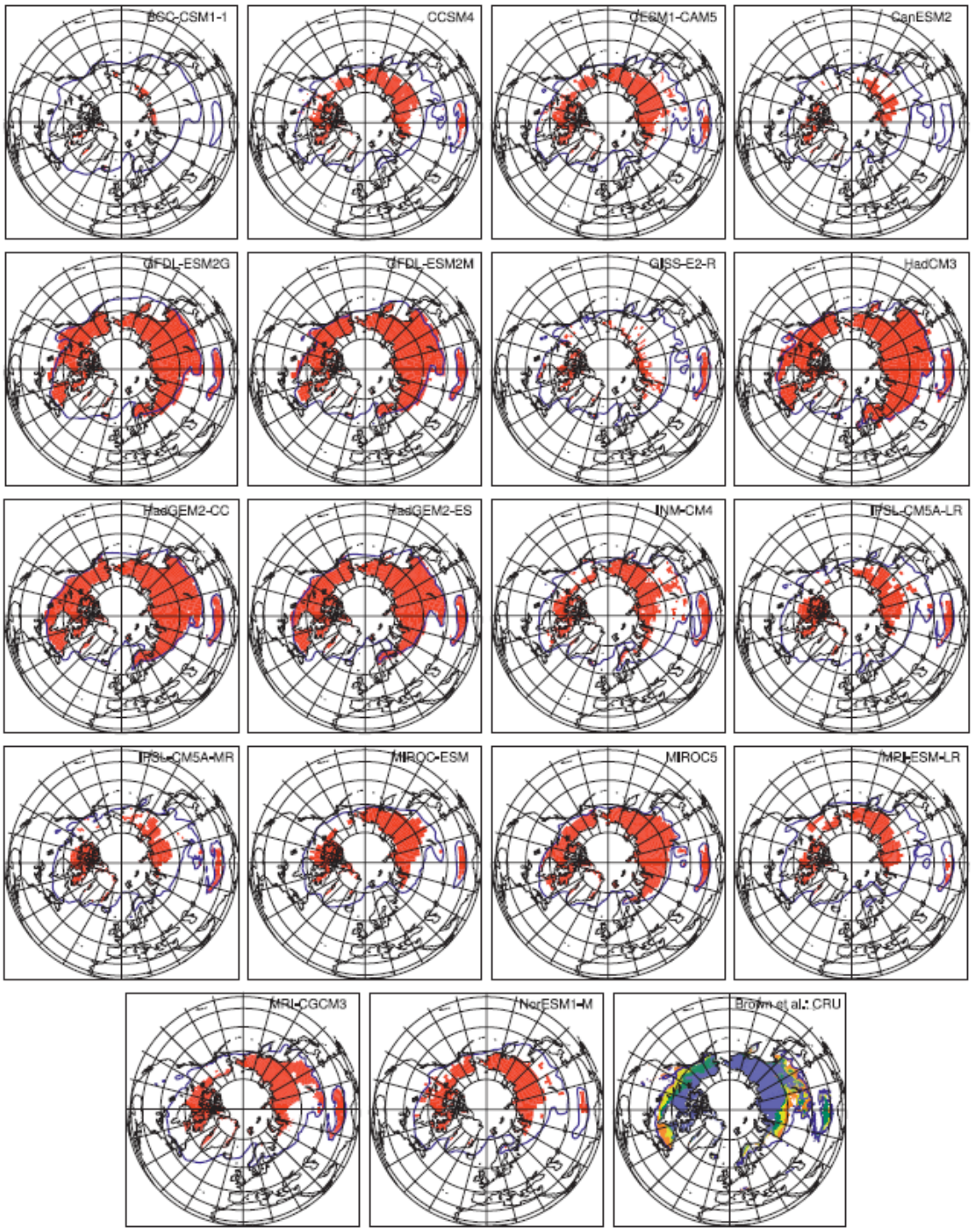

Figure 5.7. The permafrost extent for each of the Earth system permafrost models compared by [*Koven et al.*, 2013] is shown in red, under the current climate using years 2005-2015 from the RCP4.5 scenario. The observed permafrost extent is the last plot shown.

calculations. A surface heat balance is calculated as a boundary condition between sensible heat flux, latent heat flux, shortwave radiation, long-wave radiation, and ground heat flux. At the lower boundary, the geothermal heat flux is applied, which can be spatially variable. The porosity of the ground in the VAMPERS model varies with depth and rock or sediment type. This was necessary to consider because *Kitover et al.* [2015] found that porosity had a noticeable effect on the equilibrium permafrost thickness calculated by the model (up to 50 m) given a porosity range between 0.30 and 0.50.

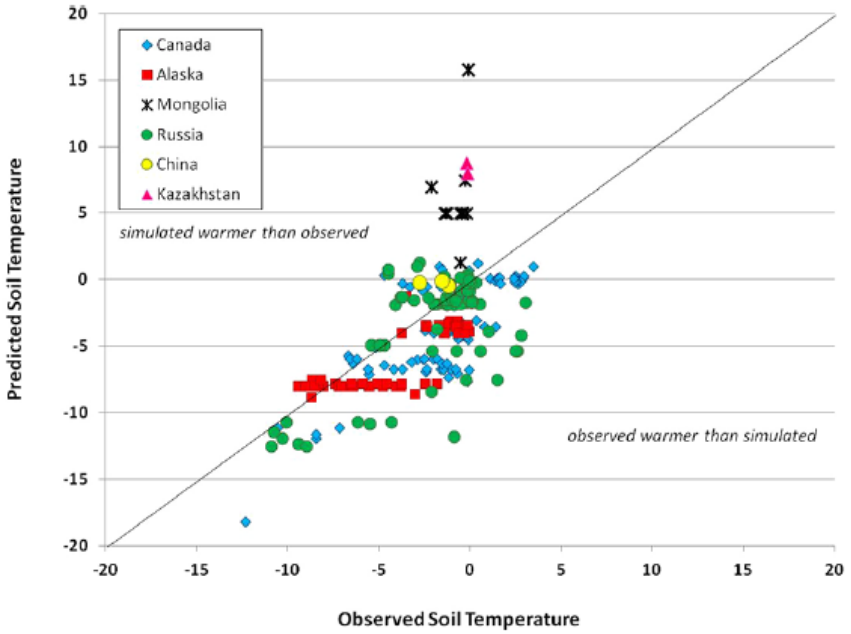

Figure 5.8. A scatter plot of the VAMPERS predicted ground temperature vs. the observed ground temperature at several borehole locations. Adapted from [*Kitover et al.*, 2015].

Kitover et al. [2015] believe that the VAMPERS model does a reasonable job of predicting shallow subsurface temperatures for most locations. Figure 5.8 shows that the observed temperature vs. the modeled temperature have a correlation of 0.64. The authors believe this is satisfactory because point values are being compared to grid cell based values, where the grid cells were very large (5.6° latitude by 5.6° longitude). The authors also offer several reasons why certain sites in Figure 5.8 are outliers, such as Kazakhstan and Mongolia. Besides the issue of grid coarseness, cooler temperatures due to higher elevation is not accounted for in the iLOVECLIM climate model, thus the simulated ground temperature is warmer than the observed at high elevation sites. Another possibility is that some of the observed permafrost depths are not a function of the present climate, but rather a relict presence from previous cold periods. Therefore, when comparing measured to simulated results, some underestimations may occur.

CryoGrid 3 is another one-dimensional thermal model which simulates vertical heat conduction and freeze-thaw processes in the subsurface, and calculates a surface energy balance which includes a snow scheme [*Westermann et al.*, 2016]. Because CryoGrid 3 specializes in providing the lower boundary for atmospheric transfer schemes, like many Earth system models, the primary driving forces are atmospheric: air temperature, relative or absolute humidity and wind speed at a known height h above ground, incoming shortwave and long-wave radiation, air pressure, and rates of snowfall and rainfall. From below, a geothermal heat flux is applied.

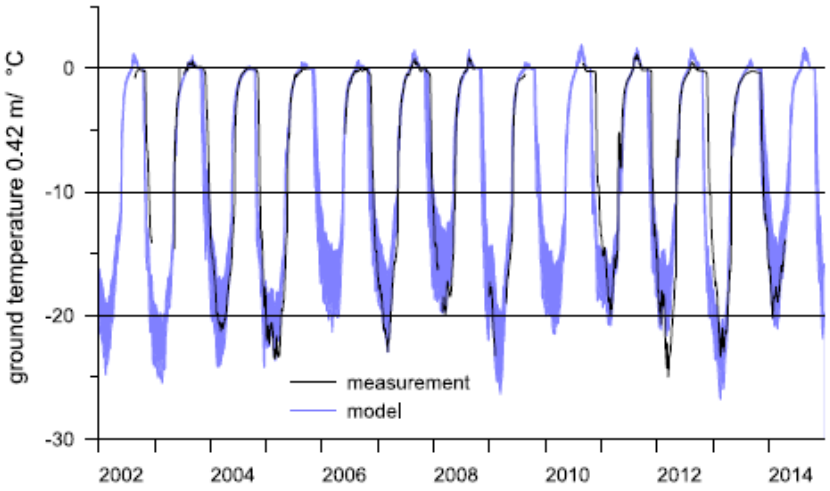

Figure 5.9. The modeled vs. measured ground temperature at a depth of 0.4 m at a wet polygon center on Samoylov Island using the CryoGrid 3 model. The model spread depicts runs with snow densities between 200 and 250 kg m^3. Adapted from [*Westermann et al.*, 2016].

In CryoGrid 3, the surface energy balance provides the top boundary condition (i.e., the fluxes of shortwave radiation and long-wave radiation) as well as the sensible, latent, and ground heat fluxes. Where the surface is covered in snow, the surface energy balance accounts for the effect of snow by dampening the penetration of shortwave radiation and changing the surface albedo. Snow accumulation and melt is also accounted for with a snow mass balance algorithm. Snow melt or rainfall allow infiltration into the surface. Re-freezing of infiltrated water is accounted for in the subsurface. The model was tested against ground temperature observations at Samoylov Island, located in the south-central part of the Lena River Delta, Siberia, and showed good agreement (Figure 5.9).

The energy balances in CryoGrid 3 require several parameters to be defined, such as the albedo and roughnesses of certain surfaces, geothermal heat flux, and thermal conductivity of the ground. Many of these parameters are assigned nominal values which are representative of the simulation region (see, for example, Figure 5.10, for model parameters assigned for Samoylov Island).

Model parameters assumed in all CryoGrid 3 and CryoGrid 3 Xice simulations.

Snow density	ρ_{snow}	200–250	kg m^{-3}	Boike et al. (2013)
Albedo snow-free surface	α_{summer}	0.2		Langer et al. (2011a)
Albedo pond/lake	α_{lake}	0.07		Burt (1954)
Albedo fresh snow	α_{max}	0.85		ECMWF (2006)
Albedo old snow	α_{min}	0.50		ECMWF (2006)
Time constant of snow albedo change – non-melting	$\tau_{\alpha,\text{f}}$	0.008	day^{-1}	ECMWF (2006)
Time constant of snow albedo change – melting	$\tau_{\alpha,\text{m}}$	0.24	day^{-1}	ECMWF (2006)
SW-radiation extinction coefficient in snow	β_{SW}	25	m^{-1}	Lei et al. (2011), Järvinen and Leppäranta (2011)
New snowfall threshold	SWE_{SF}	0.0025	m	ECMWF (2006)
Surface resistance snow-free surface	r_{s}	50	sm^{-1}	Langer et al. (2011a)
Roughness length snow-free surface	$z_{0,\text{summer}}$	10^{-3}	m	Langer et al. (2011a)
Roughness length snow	$z_{0,\text{winter}}$	5×10^{-4}	m	Langer et al. (2011b)
Emissivity snow-free surface	$\varepsilon_{\text{snow}}$	0.97		Langer et al. (2010)
Emissivity snow	$\varepsilon_{\text{snow}}$	0.99		Langer et al. (2011b)
Geothermal heat flux	F_{lb}	0.05	Wm^{-2}	Langer et al. (2013)
Thermal conductivity mineral soil fraction	k_{mineral}	3.0	$\text{Wm}^{-1}\,\text{K}^{-1}$	Langer et al. (2013)

Figure 5.10. A table of assumed parameters for the CryoGrid 3 model assigned for Samoylov Island. Adapted from [*Westermann et al.*, 2016].

Westermann et al. [2016] encourage users that have the necessary programming skills to modify and extend CryoGrid 3 for their own studies. While the model results presented are satisfactory for the study area the model was created for (i.e., North East Siberian continuous permafrost zone), it may fall short in other regions. Some improvements that are suggested include: increasing the sophistication of the snow scheme to allow for variable snow density, accounting for vegetation and canopy layers, and implementation of soil moisture and a water balance, which may affect the energy balance significantly in some regions.

Coastal Permafrost Erosion Models

The two processes that dominate the coastal erosion problem in the Arctic are thermo-denudation and thermo-abrasion [*Overduin et al.*, 2014]. Thermo-denudation refers to sub-aerial erosion that is triggered by the thawing of permafrost bluffs and proceeds under the influence of gravity in the form of subsidence or landsliding. Active layer detachment and retrogressive thaw slumping (Figure 5.11) are two examples of slope failure associated with thermo-denudation [*Lantuit & Pollard*, 2008]. Both modes involve a temperature-dependent reduction in the strength of the parent media and subsequent increase in erodibility. Thermo-abrasion refers to the combined thermal and mechanical submarine erosion of (typically ice-rich) permafrost bluffs [*Aré*, 1988]. In this process, the parent material at the base of the bluff is warmed by the ocean and eroded by the mechanical action of waves. A recess at the base of the bluff, commonly referred to as a niche, progresses landward until the overhanging

material fails in a shearing or toppling mode known as block failure (Figure 5.12). The fallen ice-bound block can disintegrate in the near-shore environment within a week [*Barnhart et al.*, 2014a]. Although thermo-denudation via slumping has gained attention in recent years (see *Guégan* [2015]), field observation and process-based modeling of coastal erosion in the Arctic (particularly in the United States) has largely focused on block failure.

Conceptual models of block failure include an accounting of resisting and driving forces. For shear-mode failures (Figure 5.13), the resisting forces are the weight component that is perpendicular to the shear plane and the shear strength of the failure plane. The driving forces are the downslope weight components and water pressure in the active layer and ice wedge (if present). For toppling-mode failures (Figure 5.13), the resisting forces are the weight of the landward component of the block and the tensile strength of the permafrost acting across the failure plane. Both modes of block failure tend to preferentially occur along the axis of an ice wedge that is parallel to the coast. It is thought that contraction-based cracks in the ice wedge act as a plane of weakness [*Hoque & Pollard*, 2009]. After thermo-abrasion has developed a niche to a critical depth, the driving forces exceed the resisting forces and failure occurs. The fallen block will often degrade rapidly because of its low position on the beach, exposing it (more frequently than the bluff edge) to the thermal and mechanical components of thermo-abrasion. Time-lapse imagery has revealed that as the fallen block is eroded, it tends to rotate further and further down the beach slope [*Barnhart et al.*, 2014a]. Therefore, fallen blocks typically do little to armor the bluff against further erosion.

Modeling coastal erosion in the Arctic requires an approach different than that typically employed for other locations. Most coastal landscape models have been developed for non-cohesive (i.e., sandy) sediments in temperate climates. The bluffs that front the Arctic coast are commonly cohesive ice-bonded silts or clays [*Lantuit et al.*, 2013]. Unlike non-cohesive bluffs, the erosion of cohesive bluffs is considered irreversible. Process-based understanding of permafrost bluff retreat requires a treatment of thermal and mechanical processes that traditional equilibrium models, nearshore models, and geotechnical models have been unable to integrate.

The framework for the modeling of niche development in frozen bluffs was pioneered by *Kobayashi* [1985]. His model estimates the rate of niche incision along the base of a bluff that is always in contact with a constant level of sea water (Figure 5.14). The three partial differential equations that describe the process, which are based on mass and heat balances, require information about the suspended sediment concentration, salt concentration in the water, water temperature, and cross-shore fluid velocity. Simplifying assumptions about mixing, surf zone diffusivity, and the physical and thermal properties of the bluff and ocean result in an analytical solution:

$$x_m = 2\zeta_m\sqrt{\epsilon t} \tag{5.4}$$

where x_m is the position of the melting front, ζ_m is a temperature-dependent parameter (requires knowing the temperature difference between the water and the melting point of

Figure 5.11. Photographs of retrogressive slump failure (top) and active layer detachment (bottom) along the Arctic coastline. Adapted from [*Lantuit & Pollard*, 2008].

Figure 5.12. Aerial and ground-level photographs of block failure along the Arctic coastline. Black arrows in aerial photograph point to exposed ice wedges for a bluff that is approximately eight meters high. Adapted from [*Hoque & Pollard*, 2009] and [*Ravens et al.*, 2012].

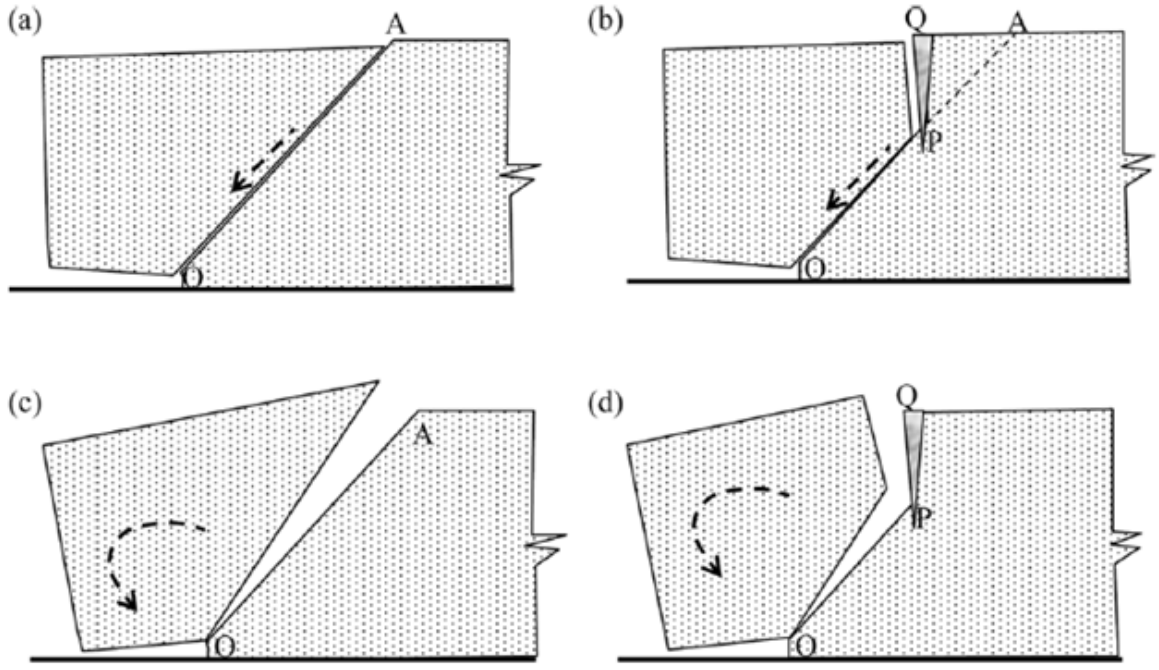

Figure 5.13. Conceptual diagrams of shear-mode block failure in the (a) absence and (b) presence of an ice wedge and toppling-mode block failure in the (c) absence and (d) presence of an ice wedge. Adapted from [*Hoque & Pollard*, 2009].

the bluff ice), ϵ is the surf zone diffusivity (requires knowing the water depth), and t is time.

The *Kobayashi* [1985] model highlights the importance of ambient seawater temperature, the mechanical action of waves, water depth, and storm duration. *Kobayashi & Aktan* [1986] expand upon the *Kobayashi* [1985] work by analyzing heat conduction through frozen sediment exposed to wave action for conditions where a niche does not form. The location of the melting surface for a bluff is determined by solving the heat conduction equation. Like *Kobayashi* [1985], unfrozen sediment is assumed to erode instantaneously. *Kobayashi & Aktan* [1986] find that convective heat flux is strongly influenced by fluid velocity and water temperature. To move toward a fully-coupled thermo-mechanical erosion model, *Kobayashi & Vidrine* [1995] develop an analytical solution for a partially frozen beach. It is linked to an existing beach profile model, COSMOS-2D [*Baird & Associates*, 1995]. While the model shows some success in representing the profile of a partially frozen beach, it does not capture the horizontal retreat of the permafrost bluff. To improve estimates of sediment transport rates from the bluff to the beach, *Kobayashi et al.* [1999] calculates bluff retreat rate as:

$$\frac{dR}{dt} = \frac{l_c h_c \left(T_w - T_m\right)}{L_c \left(H - B_c\right)} \tag{5.5}$$

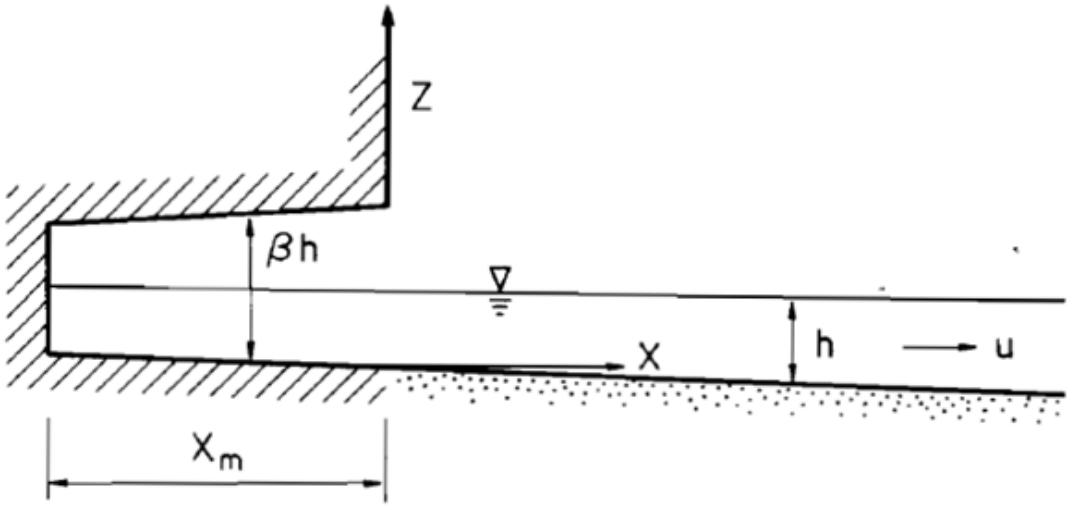

Figure 5.14. Conceptual diagram of a niche extending into a frozen bluff where h is the mean water depth, β is an empirical constant, X and Z are coordinate directions, u is the shore-normal fluid velocity, and X_m is the position of the niche through time. Adapted from [*Kobayashi*, 1985].

where R is the retreat distance, t is time, l_c is the inclined length of frozen cliff sediment exposed to wave action, h_c is the convective heat transfer coefficient, T_w is the temperature of the water, T_m is the surface temperature of the frozen bluff sediment, L_c is the volumetric latent heat of fusion of the frozen bluff sediment, H is the height of the cliff above mean sea level, B_c is the original thickness of unfrozen sediment. The *Kobayashi et al.* [1999] bluff retreat model is calibrated against observed retreat data associated with a single storm surge event along the Canadian Beaufort Sea. The calibrated model, although derived from a limited observation dataset, suggests the retreat rate is most sensitive to storm surge elevation and duration, seawater temperature and salinity, and cliff height.

Following much of the early work of Kobayashi, several Arctic coastal erosion modeling efforts began considering ways to couple niche development with block instability. *Hoque & Pollard* [2009] use the *Kobayashi* [1985] model and formulate Factor of Safety equations to assess the stability of pre-defined failure planes in a permafrost bluff as the niche forms. A Factor of Safety is the ratio of resisting to driving forces along the plane of a shear- or toppling-mode failure. For each simulation, geotechnical properties such as cohesion, internal friction angle, and/or tensile strength are defined for permafrost bluffs in the presence and absence of ice wedges. Although the geotechnical characteristics of permafrost are known to be temperature-dependent, *Hoque & Pollard* [2009] used constant values for simplification. *Ravens et al.* [2012] build upon the *Hoque & Pollard* [2009] work by using wind speed and wind direction data to determine water levels, employing the *Kobayashi* [1985] model for niche development, assuming failure at a critical niche depth (10 m), and estimating the

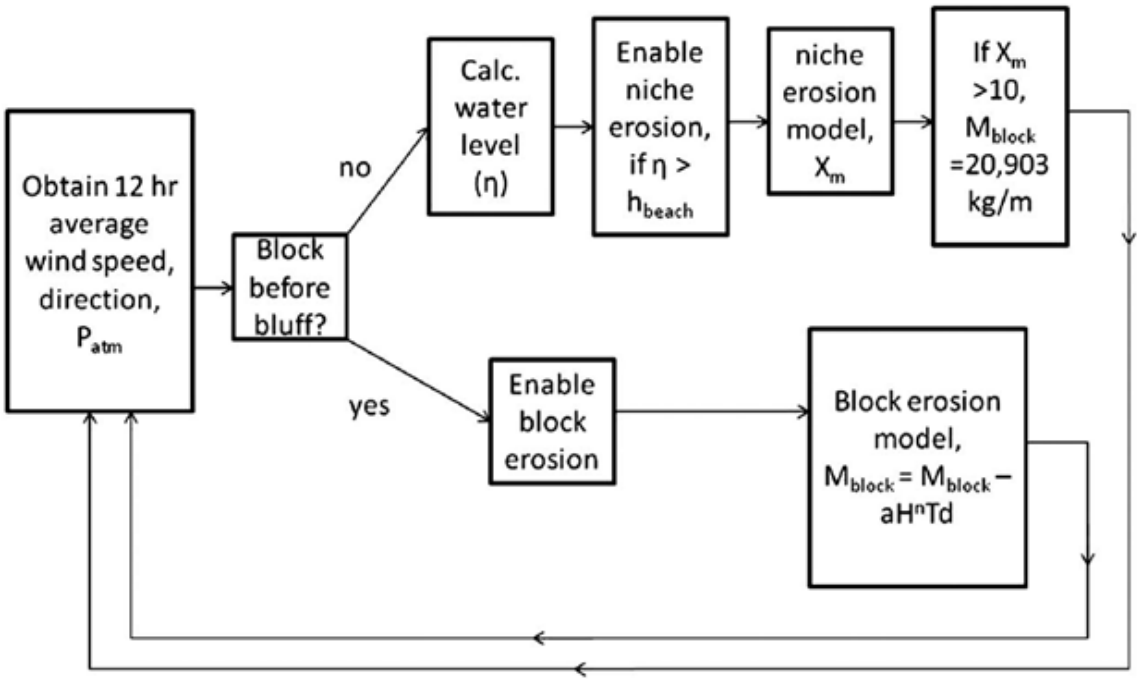

Figure 5.15. Shoreline change modeling work flow employed by *Ravens et al.* [2012]. Ocean conditions are sequentially coupled to bluff conditions. Adapted from [*Ravens et al.*, 2012].

degradation rate of the fallen block (Figure 5.15). Although the storm surge and erosion models in *Ravens et al.* [2012] are simple, the study is noteworthy because of its attempt to couple ocean and bluff processes in a transient mode. After calibrating their model with 24 years of bluff retreat data for the Beaufort Sea coast in Alaska, *Ravens et al.* [2012] calculate erosion rates for a (subsequent) seven-year period within 20%.

A distinct shift in the quantitative treatment of the Arctic coastal erosion problem appears in *Wobus et al.* [2011]. Based on field observations in Drew Point, Alaska, *Wobus et al.* [2011] hypothesize that block failure can be treated as a purely thermal problem (i.e., principally controlled by the interstitial melting of ice) rather than a thermo-abrasion problem. They employ a power-law model and a thermal-wave model that were originally derived to estimate the deterioration of an iceberg in the open sea. The power-law model (see *Holland et al.* [2008]) follows as:

$$M = \alpha \left(T_s - \delta\right)^{\beta} \tag{5.6}$$

where M is the melt rate, T_s is the temperature of the water bath, δ is the freezing point of the water bath, and α and β are empirically-derived constants from *Russell-Head* [1980].

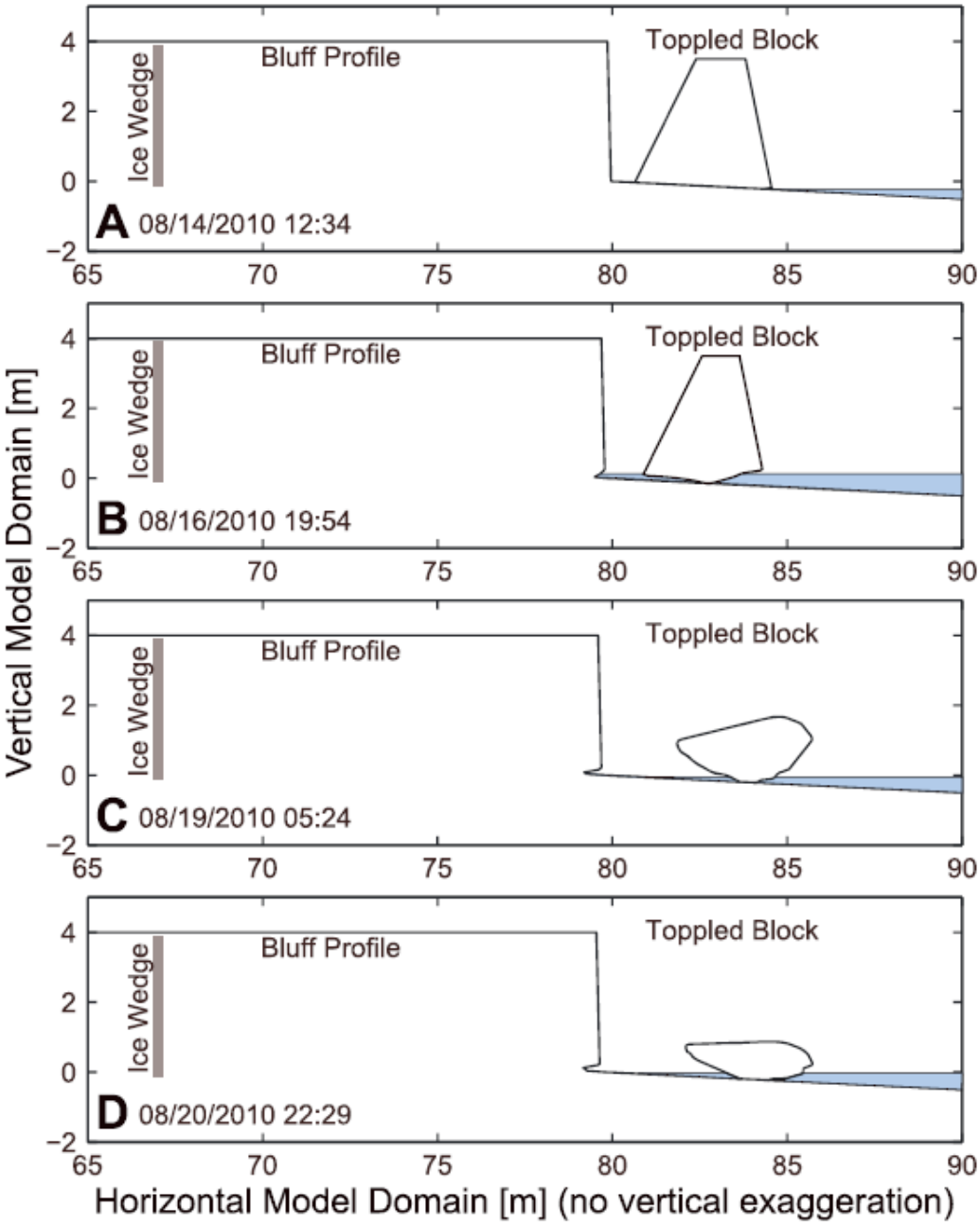

Figure 5.16. Example model output for short-term simulations conducted by *Barnhart et al.* [2014a]. Note: The short-term simulations focus on the degradation rate of the fallen block. Adapted from [*Barnhart et al.*, 2014a].

The thermal-wave model (White et al., 1980) follows as:

$$V_{we} = 0.000146 \left(\frac{R}{H}\right)^{0.2} \left(\frac{H}{\tau}\right) \Delta T \tag{5.7}$$

where V_{we} is the melt rate, R is the roughness height, H is the wave weight, τ is the wave period, and T is the temperature difference between the water and ice. The power-law and thermal-wave models predict coastal erosion rates for Drew Point within 25% of those observed over a one-year period.

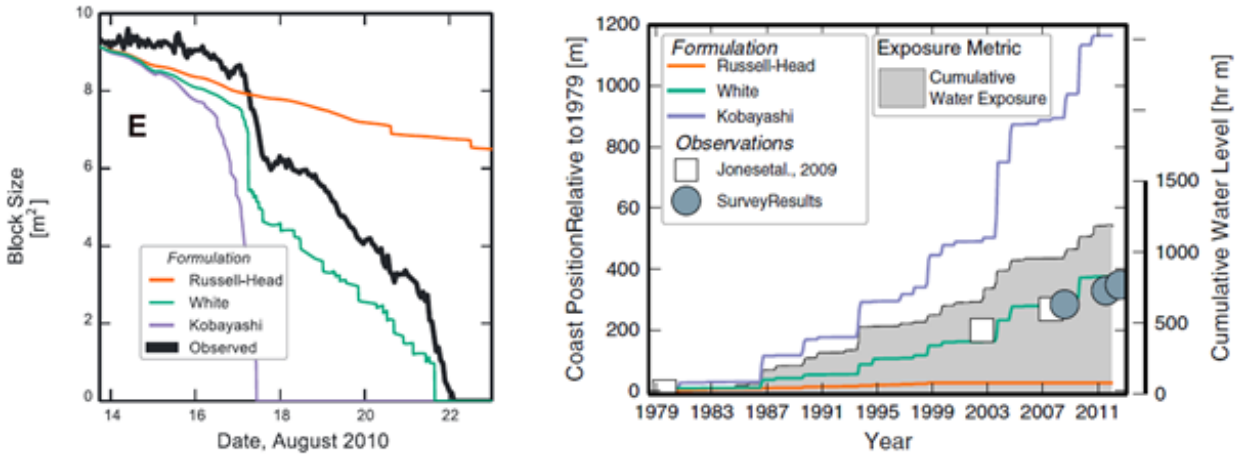

Figure 5.17. Comparison of the three bluff erosion models employed by *Barnhart et al.* [2014a] against short-term (left) and long-term (right) bluff retreat observations. Adapted from [*Barnhart et al.*, 2014a].

Barnhart et al. [2014a] compares the thermo-abrasion and iceberg modeling approaches introduced by *Kobayashi* [1985] and *Wobus et al.* [2011], respectively. The *Kobayashi* [1985] model is modified to allow for time-dependent changes in water level. The *Russell-Head* [1980] and *White et al.* [1980] iceberg melt formulations are modified by a factor to account for the difference in the heat needed to melt pure ice versus the heat needed to melt the bulk permafrost material. Subaerial erosion is also calculated (for all cases) with a simple empirical formulation related to the difference in temperature between the air and the permafrost. The criterion for bluff failure via toppling (i.e., rotation) is satisfied when:

$$T_D > T_R + T_{IW} + T_{pf} \tag{5.8}$$

where T_D is the driving torque per unit length along the coast about a pivot point at the apex of the notch, T_R is the sum of resisting torque, T_{IW} is the torque needed to overcome the cohesive strength on the ice-wedge face, and T_{pf} is the torque needed to overcome the

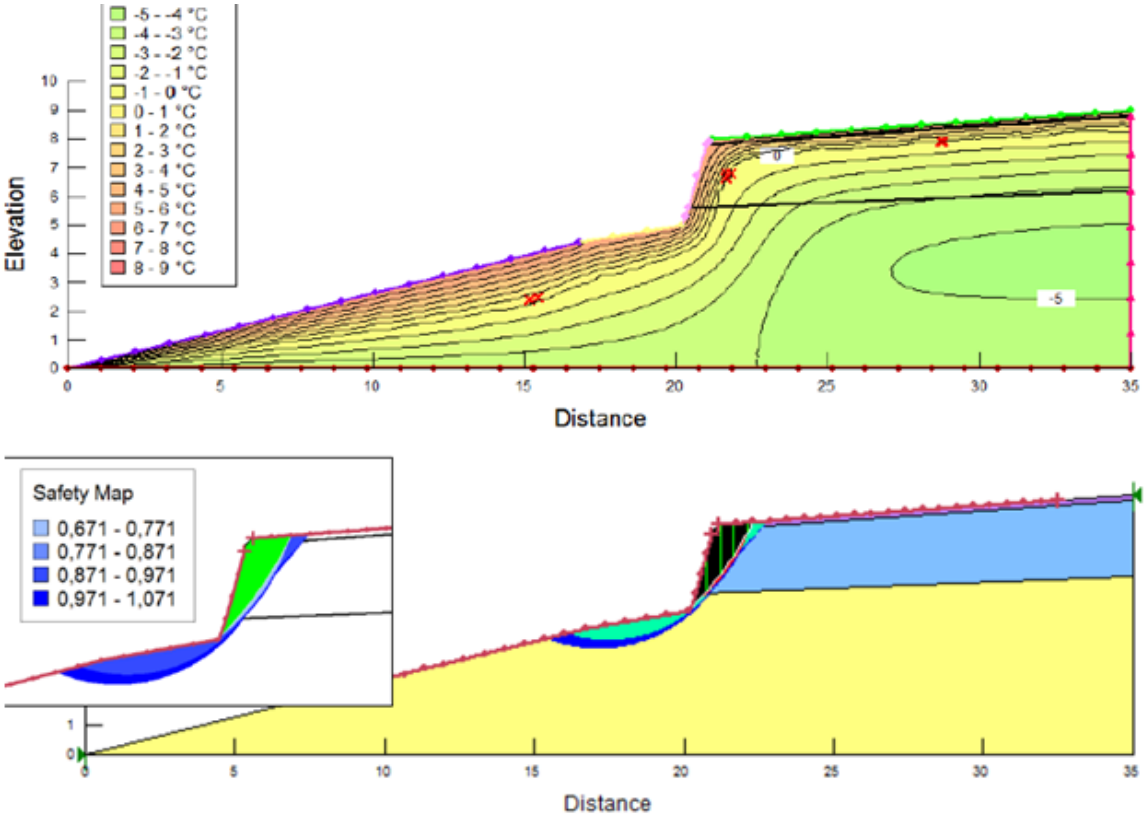

Figure 5.18. Example model outputs from simulations conducted by *Guégan* [2015]. The thermal regime simulation (top) was used to drive the slope stability assessment (bottom) for a slump-type failure. Note: A Factor of Safety less than one indicates unstable conditions. Adapted from [*Guégan*, 2015].

cohesive strength in the permafrost. The stability of a fallen block is assessed similarly, but without T_{IW} and T_{pf}.

Barnhart et al. [2014a] conduct short- (i.e., one week) and long-term (i.e., 33 year) erosion simulations for Drew Point with the modified *Russell-Head* [1980], *White et al.* [1980], and *Kobayashi* [1985] methods. For the short-term simulations (Figure 5.16 and Figure 5.17), the *White et al.* [1980] and *Kobayashi* [1985] models perform the best because they include the effects of the water temperature and the wavefield. Consideration of water temperature alone (i.e., *Russell-Head* [1980]) was not sufficient. For the long-term simulations, the *Kobayashi* [1985] model over-predicts erosion rates, highlighting the limited utility of the method for transient simulation (Figure 5.17). *Barnhart et al.* [2014a] conclude that the length of the sea-ice-free season, water exposure, and water temperature exert the greatest control on the rate of niche formation and coastal erosion, with the *White et al.* [1980] model performing most satisfactorily.

Presently, the *Barnhart et al.* [2014a] study provides the most comprehensive evaluation of block failure for permafrost bluffs along the Arctic coast. Only recently have modeling studies begun to more rigorously evaluate thermo-denudation (as opposed to thermo-abrasion) problems. For example, *Guégan* [2015] develops equations to describe temperature-dependent soil strength characteristics, models the thermal regime along several coastlines, and evaluates temperature-dependent slope stability for slump-type failure (Figure 5.18). This sequential modeling approach can used to estimate the timing of initial failure and the volume of sediment supplied to the beach, but it has not yet been developed to account to the progressive nature of slump failure or linked to cross-shore beach profile development.

A review of the coastal erosion problem in the Arctic reveals that the modeling literature is relatively young. The variability associated with modes of slope failure is reflected in the site-specific character of most studies. Existing permafrost bluff erosion models are typically calibrated to operate within a narrow range of geologic/geomorphic and oceanographic conditions. Most efforts would benefit from more information about the temperature-dependent strength behavior of soils, patterns of ground ice content, and permafrost geomorphology (e.g., cliff height and niche geometry). A common theme that emerges from the literature is that water setup (i.e., depth and duration) and temperature in the vicinity of frozen bluffs is a first-order control on erosion rates. This conclusion is perhaps most clearly realized in work that has been successful in calculating bluff retreat with equations originally derived to describe the melting rate of an iceberg in the open ocean. Although surrogate-type models have shown promise, care should be taken such that the hydrologic, thermal, and mechanical processes associated with the geomorphic system are interrogated. With this approach, models based upon ground truth and physical (as opposed to empirical) parameters will facilitate the process-based understanding needed to inform Arctic stakeholders.

Chapter 6

Putting It All Together to Create a Predictive Tool

As scientific focus has been shifting towards the polar regions, Arctic science is rapidly advancing, increasing our understanding of complex Arctic processes. Our present understanding, as outlined and summarized in this report, allows us to begin to integrate the coupled models necessary for the prediction of coastal erosion in support of Arctic risk assessments. Our current understanding emphasizes the importance of several processes: the state of the coastal permafrost thermal regime and ice content, the changing oceanographic conditions such as sea-ice concentration and seasonality, wave height, sea level rise, or storminess, and the stress state of the coastal permafrost which ultimately succumbs to failure and erosion. We also recognize that the permafrost coastal environment does not exist in isolation. Therefore, influences on the permafrost coastal environment from an Earth system scale are also important to recognize. The flow diagram presented in Figure 6.1 shows the model components and coupling necessary towards the development of a coupled model for Arctic coastal erosion. Many of these models already exist individually, but coupling them together presents a challenge that we believe is possible to accomplish by the end of this decade.

The coupled model consists of four major components. The most general component is the Earth system model, which provides the major boundary conditions to the region of model application. For example, an Earth system model would provide the wind spectra, sea-ice concentration, currents, global sea level, solar flux, atmospheric temperature, ocean temperature, and ocean and land evaporative fluxes. These are important inputs to both the sea-ice-wave model, the ocean circulation model, as well as the permafrost thermal model components.

The sea-ice-wave model component is responsible for calculating the three dimensional wave energy spectra that results from the interaction between ocean waves and the presence of sea-ice. Although large theory gaps exist in how sea-ice and waves interact, this field of study is progressing, and simple relationships do exist. This model requires information that is site specific, such as the ocean water salinity, and the bathymetry, including seafloor roughness. It passes several pieces of information to the ocean circulation model component, such as: the three-dimensional wave spectra, the turbulent wave energy dissipation, radiation shear stresses, orbital velocities, currents, sea surface temperature, and atmospheric

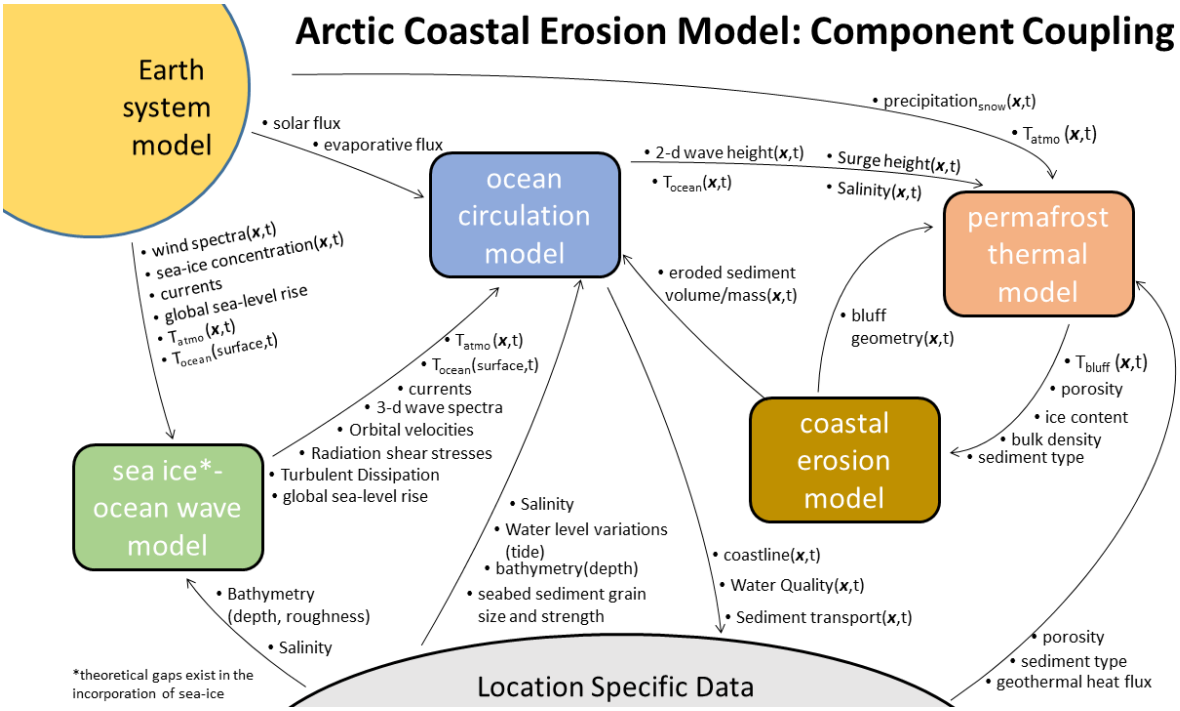

Figure 6.1. A coupled model for Arctic coastal erosion consists of an Earth System model, a sea-ice-ocean wave model, an ocean circulation model, a permafrost thermal model, and a coastal erosion model. Some parameters must be sourced from location-specific data sets.

temperature.

The ocean circulation model component takes the outputs of the sea-ice-wave model described previously, and uses them to calculate region-specific oceanographic conditions at the coast of interest. Because it is designed to be region-specific, it should also make best use of location-specific data for the seabed sediment grain size and strength, the bathymetry, tidal variations, and local ocean water salinity. The oceanographic conditions, such as the wave height, surge height, ocean temperature, and salinity (all as a function of time and space), are given as inputs to the permafrost thermal model component.

It is the main responsibility of the permafrost thermal model component to calculate the unsteady temperature field and the changing ice content of the coastal permafrost. It uses information from the oceanographic conditions as boundary conditions. It also takes the atmospheric temperature and precipitation data from an Earth system model as additional boundary conditions. Location specific-data, such as the geothermal heat flux, permafrost sediment type, porosity, or initial ice content are also crucial for accurate calculations. The permafrost temperature field, porosity, ice content, bulk density, and sediment type are passed into the coastal erosion model component.

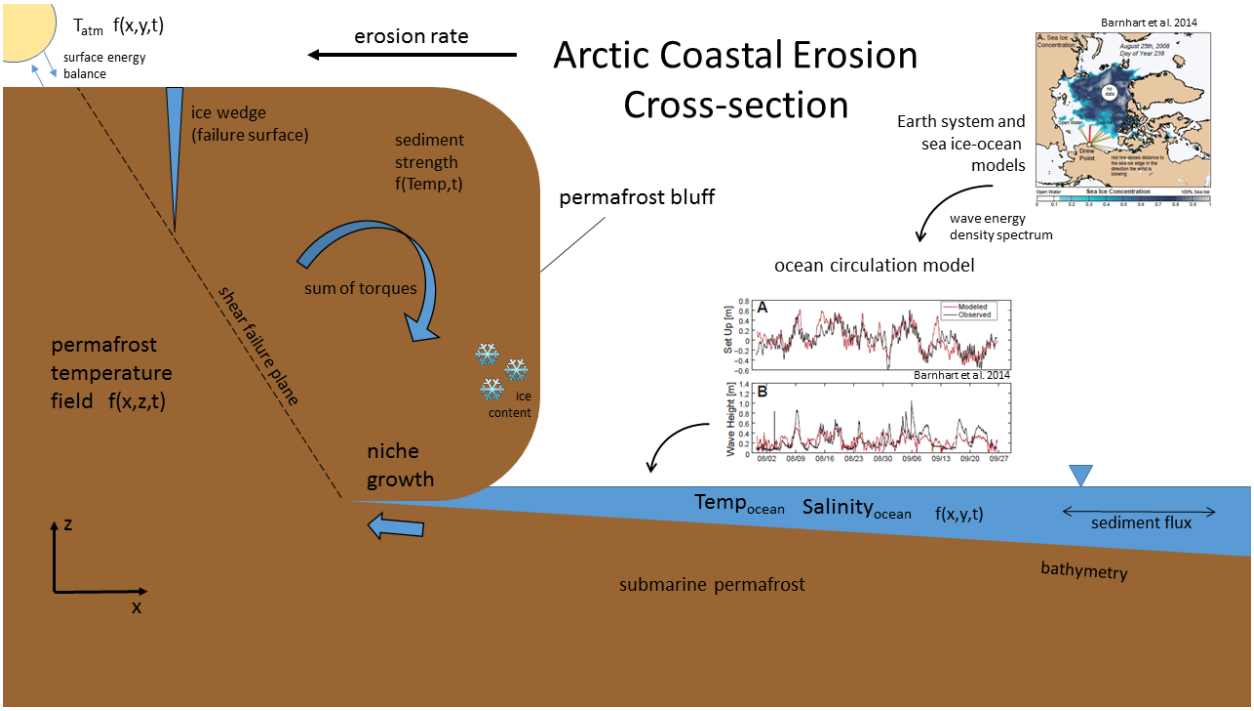

Figure 6.2. A conceptual figure for a coupled model for Arctic coastal erosion.

The coastal erosion model component is primarily responsible for calculating the failure state of the permafrost coast. It ideally would calculate sediment strength properties as a function of the temperature of the permafrost. Once a failure state is encountered, the erosion model component changes the permafrost bluff geometry, and records the eroded sediment volume and mass. The eroded sediment volume as well as the new shoreline geometry information is then passed back to the ocean circulation model component, where it can transport the sediment locally. The new permafrost bluff geometry is also important to pass back to the permafrost thermal model component, so that the locations of the new boundaries are known.

The conceptual diagram in Figure 6.2 illustrates the coupled model components relative to the modeled physical setting.

Through the development of the proposed coupled model for Arctic erosion, several advancements will be made which have not been previously accomplished:

- Closing theory gaps on the influence of sea-ice in wave modeling
- Accounting for time-dependent ocean temperature rather than assuming a single static water temperature
- Treating individual storms throughout their entire duration during the open water

season rather than lumping storm events

- Including detailed bathymetry in wave generation calculations, with large spatial scales for wave propagation
- Calculating the time-dependent, two-dimensional permafrost temperature field rather than assuming a single static ground temperature
- Considering geotechnical permafrost strength properties that vary with temperature and ice content
- Calculating thermal niche geometry in two dimensions according to the temperature field, rather than parameterizing niche propagation in one dimension
- The ability to investigate the entire spectrum between iceberg and frozen sediment models for thermo-erosion with ice content included in the permafrost thermal model component
- Calculating the stress state, allowing several failure types to be considered, rather than relying on pre-defined failure planes of a single mode
- Including sediment transport modeling to understand where eroded sediment moves and including it as a feedback to ocean circulation

These improvements introduce more physical processes into each model component, as well as introduce stronger coupling between model components than previously attempted. Because of the diversity of physical processes involved in coastal erosion in the Arctic, accomplishing such a task will require a diverse set of skills and a team with a broad knowledge base.

Although the fully coupled model will be complex, like any model, it will most likely produce the best predictions for limited regions, where location-specific data is available and representative of the region chosen. Model validation and calibration is also required. Validation and calibration can be most practically performed using hind casts of the required parameters. However, to best understand how current conditions are captured by the model, field sites should also be studied and measured, and should be an integral part of model development.

References

Agergaard, F. A., and T. Ingeman-Nielsen. 2012. Strength properties of warming fine-grained permafrost. Abstract from 10th International Conference on Permafrost, Salekhard, Russian Federation.

Alaska Department of Environmental Protection. 2016. Department of Defense Sites in Alaska. https://dec.alaska.gov/, accessed 2016.09.20.

Aré, F. 1988. Thermal abrasion of sea coasts (part I). Polar Geography and Geology, 12(2), 87-111.

Arenson, L. U., S. M. Springman, and D. C. Sego. 2007. The rheology of frozen soils. Applied Rheology, 17, 12147-1 12147-14.

Arp, C.D., B.M. Jones, J.A. Schmutz, F.E. Urban, and M.T. Jorgenson. 2010. Two mechanisms of aquatic and terrestrial habitat change along an Alaskan Arctic coastline. Polar Biology, 33, 1629-1640.

Baird & Associates. 1995. Development of a model for the thermal-mechanical erosion on arctic coasts. Final report prepared for Geological Survey of Canada, Oakville, Ontario, Canada.

Barnhart, K. R., R. S. Anderson, I. Overeem, C. Wobus, G. D. Clow, and F. E. Urban. 2014a. Modeling erosion of ice-rich permafrost bluffs along the Alaskan Beaufort Sea coast. Journal of Geophysical Research: Earth Surface, 119, 1155-1179.

Barnhart, K. R., I. Overeem, and R. S. Anderson. 2014b. The effect of changing sea ice on the physical vulnerability of Arctic coasts. The Cryosphere, 8, 1777-1799.

Brown, J., O.J. Ferrians, Jr., J.A. Heginbottom, and E.S. Melnikov. 1998. Circum-arctic map of permafrost and ground ice conditions. Boulder, CO: National Snow and Ice Data Center. Digital media.

Clement, J.P., J.L. Bengston, and B.P. Kelly. 2013. Managing for the future in a rapidly changing Arctic. A report to the President. Interagency Working Group on Coordination of Domestic Energy Development and Permitting in Alaska (D. J. Hayes, Chair), Washington, D.C., 59 p.

Coon, M., R. Kwok, G. Levy, M. Pruis, H. Schreyer, and D. Sulsky. 2007. Arctic Ice Dynamics Experiment AIDJEX assumptions revisited and found inadequate. Journal of Geophysical Research, 112, C11S90.

Deltares. 2014. DELFT3D, Functional Specifications. Version: 2.20.33337. Published and printed by Deltares, http://www.deltares.nl, accessed 2016.09.16.

Dupeyrat, L. F. Costard, R. Randriamazaoro, E. Gailhardis, E. Gautier, and A. Fedorov. 2011. Effects of ice content on the thermal erosion of permafrost: Implications for coastal and fluvial erosion. Permafrost and Periglacial Processes, 22, 179-187.

Farouki, O. T. 1981. Thermal properties of soil. Cold Regions Research and Engineering Laboratory, Monograph 81-1, 155 pp.

Forbes, D. L., and R. B. Taylor. 1994. Ice in the shore zone and the geomorphology of cold coasts. Progress in Physical Geography, 18,1, 59-89.

Gibbs, A. E., and B. M. Richmond. 2015. National assessment of shoreline change-Historical shoreline change along the north coast of Alaska, U.S.-Canadian border to Icy Cape. U.S. Geological Survey Open-File Report 2015-1048, 96 p.

Girard, L., S. Bouillon, J. Weiss, D. Amitrano, T. Fichefet, and V. Legat. 2011. A new modeling framework for sea-ice mechanics based on elasto-brittle rheology. Annals of Glaciology, 52, 57, 123-132.

de Goede, E., T. Wagner, R. de Graaff, and B. Sheets. 2014. Modeling of ice growth and transport on a regional scale, with application to fountain lake, Minnesota, USA. AMSM 2014 33rd International Conference on Ocean, Offshore and Arctic Engineering.

Goosse, H., V. Brovkin, T. Fichefet, R. Haarsma, et al. 2010. Description of the Earth system model of intermediate complexity LOVECLIM version 1.2. Geoscientific Model Development, 3, 603-633.

Gorokhovich, Y. and A. Leiserowiz. 2012. Historical and future coastal changes in Northwest Alaska. Journal of Coastal Research, 28, 1A, 174-186.

Grenier, C., H. Anbergen, V. Bense, E. Coon, N. Collier, F. Costard, M. Ferry, A. Frampton, J. Frederick, J. Holmen, A. Jost, S. Kokh, B. Kurylyk, J. McKenzie, J. Molson, L. Orgogozo, R. Pannetier, A. Riviere, N. Roux, W. Rhaak, J. Scheidegger, J.-O. Selroos, R. Therrien, P. Vidstrand, and C. Voss. 2016. The InterFrost benchmark of Thermo-Hydraulic codes for cold regions hydrology first inter-comparison phase results. 11th International Conference on Permafrost, Potsdam, Germany, 20-24 June.

Grigoriev, M. N. 2008. Cryomorphogenesis and lithodynamics of the East Siberian near-shore shelf zone, Habilitation thesis, SB RAS Permafrost Institute, Yakutsk.

Grigoriev, M. N., V. V. Kunitsky, R. V. Chzhan, V. V. Shepelev. 2009. On the variation in geocryological, landscape, and hydrological conditions in the Arctic zone of East Siberia in connection with climate warming. Geography and Natural Resources, 30, 101-106.

Grigoriev, M. N., S. O. Razumov, V. V. Kunitsky, and V. B. Spektor. 2006. Dynamics of the Russian East Arctic Sea coast: major factors, regularities and tendencies. Kriosfera Zemli (Earths Cryosphere), 10, 7494.

Grosse, G., L. Schirrmeister, C. Siegert, V. V. Kunitsky, E. A. Slagoda, A. A. Andreev, A. Y. Dereviagyn. 2007. Geological and geomorphological evolution of a sedimentary periglacial landscape in Northeast Siberia during the Late Quaternary. Geomorphology, 86, 2551.

Grosse, G., J. E. Robinson, R. Bryant, M. D. Taylor, W. Harper, A. DeMasi, E. Kyker-Snowman, A. Veremeeva, L. Schirrmeister, and J. Harden. 2013. Distribution of late Pleistocene ice-rich syngenetic permafrost of the Yedoma Suite in east and central Siberia, Russia: U.S. Geological Survey Open File Report 2013-1078, 37 p.

Guégan, E. 2015. Erosion of permafrost affected coasts: rates, mechanisms and modelling, thesis, Norwegian University of Science and Technology, Norway.

Guégan, E. and Christiansen H. 2016. Seasonal Arctic coastal bluff dynamics in Adventfjorden, Svalbard. Permafrost and Periglacial Processes, DOI 10.1002/ppp.1891.

Günther, F., P. P. Overduin, A. V. Sandakov, G. Grosse, and M. N. Grigoriev. 2013a. Short and long-term thermo-erosion of ice-rich permafrost coasts in the Laptev Sea region. Biogeosciences, 10, 42974318.

Günther, F., P. P. Overduin, A. Baranskaya, T. Opel, and M. N. Grigoriev. 2015. Observing Muostakh Island disappear: erosion of a ground-ice-rich coast in response to summer warming and sea ice reduction on the East Siberian shelf. The Cryosphere Discussions, 7, 41014176.

Haas, C. 2012. Airborne observations of the distribution, thickness, and drift of different sea ice types and extreme ice features in the canadian beaufort sea, OTC Arctic Technology Conference, 3-5 December, Houston, Texas, USA.

Harper, J.R. 1978. Coastal erosion rates along the Chukchi Sea Coast near Barrow, Alaska. Arctic, 31(4), 428-433.

Harper, J. R. 1990. Morphology of the Canadian Beaufort Sea coast. Marine Geology, 91, 75-91.

Hasselmann, K., T. P. Barnett, E. Bouws, H. Carlson, D. E. Cartwright, et al. 1973. Measurements of wind-wave growth and swell decay during the Joint North Sea Wave Project (JONSWAP). Technical Report, Deutches Hydrographisches Institut.

Hequette, A., and P. W. Barnes. 1990. Coastal retreat and shoreface profile variations in the Canadian Beaufort Sea. Marine Geology, 91, 113-132. Erosion threat at remote military radars decades ahead of schedule

Holland, P.R., A. Jenkins, and D.M. Holland. 2008. The response of ice shelf basal melting to variations in ocean temperature. Journal of Climate, 21, 2558-2572.

Hoque, M. A., and W. H. Pollard. 2009. Arctic coastal retreat through block failure. Canadian Geotechnical Journal, 46, 1103-1115.

Hoque, M. A., and W. H. Pollard. 2016. Stability of permafrost dominated coastal cliffs in the Arctic. Polar Science, 10, 79-88.

Hughes, Z. 2016. Erosion threat at remote military radars decades ahead of schedule. Alaska Public Media. http://www.alaskapublic.org/2016/07/04/erosion-threat-at-remote-military-radars-decades-ahead-of-schedule/

Hunke, E., and B. Lipscomb. 2006. CICE the Los Alamos sea ice model documentation and software user's manual. Los Alamos National Laboratory.

Hume, J.D., M. Schalk M., and P.W. Hume. 1972. Short-term climate changes and coastal erosion, Barrow, Alaska. Arctic, 25(4), 272-278.

Ivey, M. 2010. ARM climate research facilities on the north slope of Alasksa - Barrow, Atqasuk, and Oliktok. Presentation at Climate Experiments in High-Latitude Ecosystems (workshop). International Arctic Research Center, University of Alaska, Fairbanks.

Jones, B. M., C. D. Arp, M. T. Jorgenson, K. M. Hinkel, J. A. Schmutz, and P. L. Flint. 2009. Increase in the rate and uniformity of coastline erosion in Arctic Alaska. Geophysical Research Letters, 36, L03503.

Jordan, J.W., W.F. Manley, D.M. Sanzone, and O.K. Mason. 2006. Field-based measurement of coastal erosion in the Southeast Chukchi Sea, Alaska. Abstract, Arctic Coastal Dynamics Report of the 6th International Workshop, Arctic Centre, University of Groningen, Reports on Polar and Marine Research.

Jorgenson, M.T. and J. Brown. 2005. Classification of the Alaskan Beaufort Sea Coast and estimation of carbon and sediment inputs from coastal erosion. Geo-Marine Letters, 25, 69-80.

Kanevskiy, M., Y. Shur, D. Fortier, M. T. Jorgenson, and E. Stephani. 2011. Cryostratigraphy of late Pleistocene syngenetic permafrost (yedoma) in northern Alaska, Itkillik River exposure. Quaternary Research, 75, 584-596.

Kanevskiy, M., Y. Shur, M. T. Jorgenson, C.-L. Ping, G. J. Michaelson, D. Fortier, E. Stephani, M. Dillon, and V. Tumskoy. 2013. Ground ice in the upper permafrost of the Beaufort Sea coast of Alaska. Cold Regions Science and Technology, 85, 56-70.

Keller, J. B. 1998. Gravity waves on ice-covered water. Journal of Geophysical Research Oceans, 103, C4, 7663-7669.

Kim, Y., D. Chae, K. Kim, and W. Cho. 2016. Physical and mechanical characteristics of frozen ground at various sub-zero temperatures. KSCE Journal of Civil Engineering, 20, 2365.

Kitover, D., R. Van Balen, D. M. Roche, and H. Renssen. 2015. Advancement toward coupling of the VAMPER permafrost model within the Earth system model ILOVECLIM (version 1.0): Description and validation. Geoscientific Model Development, 8(5), 1445-1460.

Kobayashi, N. 1985. Formation of thermoerosional niches into frozen bluffs due to storm surges on the Beaufort Sea Coast. Journal of Geophysical Research, 90(C6), 11983-11988.

Kobayashi, N. and D. Aktan. 1986. Thermerosion of frozen sediment under wave attack. Journal of Waterway, Port, Coastal, and Ocean Engineering, 112(1), 140-158.

Kobayashi, N. and J. Vidrine. 1995. Combined thermal-mechanical erosion processes model. Research Report No. CACR-95-12, Center for Applied Coastal Research, University of Delaware, Newark Delaware.

Kobayashi, N., J. C. Vidrine, R. B. Nairn, and S. M. Solomon. 1999. Erosion of frozen cliffs due to storm surge on Beaufort Sea coast. Journal of Coastal Research, 15, 2, 332-344.

Koven, C. D., W. J. Riley, and A. Stern. 2013. Analysis of permafrost thermal dynamics and response to climate change in the CMIP5 Earth system models. Journal of Climate, 26, 1877-1900.

Kwok, R., G. F. Cunningham, M. Wensnahan, I. Rigor, H. J. Zwally, and D. Yi. 2009. Thinning and volume loss of the Arctic Ocean sea ice cover: 2003–2008. Journal of Geophysical Research Oceans, 114, C7.

Lantuit, H., P. P. Overduin, N. Couture, R. S. Odegård. 2008. Sensitivity of coastal erosion to ground ice contents: An Arctic-wide study based on the ACD Classification of Arctic Coasts. In Ninth International Conference on Permafrost, Kane DL, Hinkel KM (eds). Institute of Northern Engineering, University of Alaska Fairbanks: 1, 10251029.

Lantuit, H. and W.H. Pollard. 2008. Fifty years of coastal erosion and retrogressive thaw slump activity on Herschel Island, southern Beaufort Sea, Yukon Territory, Canada. Geomorphology, 95, 84-102.

Lantuit, H., D. Atkinson, P. P. Overduin, M. Grigoriev, V. Rachold, G. Grosse, H.-W. Hubberten. 2011. Coastal erosion dynamics on the permafrost-dominated Bykovsky Peninsula, north Siberia, 1951-2006. Polar Research, 30, 7341.

Lantuit, H., et al. 2012. The Arctic coastal dynamics database: A new classification scheme and statistics on Arctic permafrost coastlines. Estuaries and Coasts, 35(2), 383-400.

Lantuit, H., P. P. Overduin, and S. Wetterich. 2013. Recent progress regarding permafrost coasts. Permafrost and Periglacial Processes, 24, 120-130.

Lee, C. M., S. Cole, M. Doble, L. Freitag, et al. 2012. Marginal Ice Zone (MIZ) Program: Science and Experiment Plan. Applied Physics Laboratory, University of Washington.

Lemieux, J.-F., C. Beaudoin, F. Dupont, F. Roy, G. C. Smith, et al. 2016. The Regional Ice Prediction System (RIPS): verification of forecast sea ice concentration. Quarterly Journal of the Royal Meteorolgical Society, 142, 632-643.

Lisiecki, L. E., and M. E. Raymo (2005), A Pliocene-Pleistocene stack of 57 globally distributed benthic δ^{18}O records, *Paleoceanography, 20*, PA1003.

Liu, A. K., and E. Mollo-Christensen. 1988. Wave propagation in a solid ice pack. Journal of Physical Oceanography, 18, 1, 702-712.

Liu, A. K., B. Holt, and P. W. Vachon. 1991. Wave propagation in the marginal ice zone: model predictions and comparisons with buoy and synthetic aperture radar data. Journal of Geophysical Research, 96, C3, 4605-4621.

Manson, G. K. 2015. Coastal mapping and modelling of Tuktoyaktuk Harbour, Western Arctic, Canada. Abstract EP23A-0946 presented at the American Geophysical Union, Fall Meeting, San Francisco, CA, 14-18 Dec.

Mars, J.C. and D.W. Houseknecht. 2007. Quantitative remote sensing study indicates doubling of coastal erosion rate in past 50 yr along a segment of the Arctic coast of Alaska. Geology, 35(7), 583-586.

Martin, S., and P. Kauffman. 1981. A field and laboratory study of wave damping by grease ice. Journal of Glaciology, 27, 96, 283-313.

Martin, P.D., J.L. Jenkins, F.J. Adams, M.T. Jorgenson, A.C. Matz, D.C. Payer, P.E. Reynolds, A.C. Tidwell, and J.R. Zelenak. 2009. Wildlife Response to Environmental Arctic Change: Predicting Future Habitats of Arctic Alaska. Report of the Wildlife Response to Environmental Arctic Change (WildREACH): Predicting Future Habitats of Arctic Alaska Workshop, 17-18 November 2008. Fairbanks, Alaska: U.S. Fish and Wildlife Service. 138 pp.

McKie, R. 2016. *Next year or the year after, the Arctic will be free of ice.* UK Guardian, published August 21 2016, https://www.theguardian.com/environment/2016/aug/21/arctic-will-be-ice-free-in-summer-next-year, accessed 2016.09.11.

NASA 2016. Multi-year Arctic Sea Ice with Date Overlay, NASA/Goddard Space Flight Center Scientific Visualization Studio, http://svs.gsfc.nasa.gov/cgi-bin/details.cgi?aid=3915, accessed 2016.09.02.

Newyear, K., and S. Martin. 1999. Comparison of laboratory data with a viscous two-layer model of wave propagation in grease ice. Journal of Geophysical Research Oceans, 104, C4, 7837-7840.

Overduin, P. P., M. C. Strzelecki, M. N. Grigoriev, N. Couture, H. Lantuit, D. St.-Hilaire-Gravel, F. Gunther, and S. Wetterich. 2014. Coastal changes in the Arctic. From: Martini, I. P. and Wanless, H. R. (eds) Sedimentary Coastal Zones from High to Low Latitudes: Similarities and Differences. Geological Society, London, Special Publications, 388.

Perrie, W., and Y. Hu. 1996. Air-ice-ocean momentum exchange. Part 1: Energy transfer between waves and ice floes. Journal of Physical Oceanography, 26, 9, 1705-1720.

Pierson, W. J. and L. Moskowitz. 1964. A proposed spectral form for fully developed wind seas based on the similarity theory of SA Kitaigorodskii. Journal of Geophysical Research, 69, 24, 5181-5190.

Pizhankova, E. I. and M. S. Dobrynina. 2010. The dynamics of the Lyakhovsky Islands coastline (results of aerospace image interpretation). Kriosfera Zemli (Earths Cryosphere), 14, 6679.

Posey, P. G., E. J. Metzger, A. J. Wallcraft, D. A. Hevert, R. A. Allard, et al. 2015. Improving Arctic sea ice edge forecasts by assimilating high horizontal resolution sea ice concentration data into the U.S. Navy's ice forecast systems. The Cryosphere, 9, 1735-1745.

Radosavljevic, B., H. Lantuit, W. Pollard, P. P. Overduin, N. Couture, T. Sachs, V. Helm, and M. Fritz. 2016. Erosion and flooding Threats to coastal infrastructure in the Arctic: A case study from Herschel Island, Yukon Territory, Canada. Estuaries and Coasts, 39, 900-915.

Rampal, P., J. Weiss, and D. Marsan. 2009. Positive trend in the mean speed and deformation rate of Arctic sea ice, 1979–2007. Journal of Geophysical Research Oceans, 114, C5.

Ravens, T. M., B. M. Jones, J. Zhang, C. D. Arp, and J. A. Schmutz. 2012. Process-based coastal erosion modeling for Drew Point, North Slope, Alaska. Journal of Waterway, Port, Coastal, and Ocean Engineering, 138, 2, 122-130.

Razbegin, V. N., S. S. Vyalov, R. V. Maksimyak, and A. V. Sadovskii. 1996. Mechanical properties of frozen soils. Soil Mechanics and Foundation Engineering, 33, 2, 35-45.

Reimnitz, E., S.M. Graves, and P.W. Barnes. 1988. Beaufort Sea coastal erosion, sediment flux, shoreline evolution, and the erosional shelf profile. U.S. Geological Survey Miscellaneous Investigations Series Map 1182-G, 1-22.

Riseborough, D., N. Shiklomanov, B. Etzelmuller, S. Gruber, and S. Marchenko. 2008. Recent advances in permafrost modelling. Permafrost and Periglacial Processes, 19, 137-156.

Robinson, A. L. 2016. Electronic image, http://haveland.com/share/arctic-death-spiral-1979-201601.jpg, accessed 2016.09.02.

Rogers, W. E., et al. 2011. On use of internal constraints in recently developed physics for wave models. Proc. 12th Int. Workshop on Wave Hindcasting and Forecasting and 3rd Coastal Hazards Symp., Big Island, Hawaii, 30 Oct. - 4 Nov.

Russell-Head, D.D. 1980. The melting of free-drifting icebergs. Annals of Glaciology, 1, 119-122.

Sayles, F. H. and O. L. Carbee. 1981. Strength of frozen silt as a function of ice content and dry unit weight. Engineering Geology, 18, 55-66.

Schreyer, H., L. Monday, D. Sulsky, M. Coon, and R. Kwok. 2006. Elastic-decohesive constitutive model for sea ice. Journal of Geophysical Research, 111, C11S26.

Schweiger, A., R. Lindsay, J. Zhang, M. Steele, H. Stern, and R. Kwok. 2011. Uncertainty in modeled Arctic sea ice volume. Journal of Geophysical Research Oceans, 116, C8.

Schwendeman, M., J. M. Thomson, and J. Gemmrich. 2012. Wave Breaking Dissipation in Fetch-Limited Seas, abstract OS13F-06 presented at American Geophysical Union, Fall Meeting, San Francisco, CA, 3-7 Dec.

Sheppard, K. 2015. Climate change takes a village as the planet warms, a remote Alaskan town shows just how unprepared we are. Huffington Post. http://www.huffingtonpost.com/, accessed 2016.09.20.

Solomon, S. M. 2005. Spatial and temporal variability of shoreline change in the Beaufort-Mackenzie region, northwest territories, Canada. Geo-Marine Letters, 25, 127-137.

Stopa, J. E., F. Ardhuin, and F. Girard-Ardhuin. 2016. Wave climate in the Arctic 1992–2014: seasonality and trends. The Cryosphere, 10, 1605-1629.

Squire, V. A. 2007. Of ocean waves and sea-ice revisited. Cold Regions Science and Technology, 49, 2, 110-133.

Sulsky, D., and K. Peterson. 2011. Towards a new elastic-decohesive model of Arctic sea ice. Physica D: Nonlinear Phenomena, 240, 1674-1683.

Thomson, J., V. Squire, S. Ackley, E. Rogers, A. Babanin, et al. 2013. Sea State and Boundary Layer Physics of the Emerging Arctic Ocean. Technical Report, Applied Physics Laboratory University of Washington.

Thomson, J. and W. E. Rogers. 2014. Swell and sea in the emerging Arctic ocean. Geophysical Research Letters, 41, 3136-3140.

Tolman, H. L., M. L. Banner, and J. M. Kaihatu. 2013. The NOPP operational wave model improvement project. Ocean Modelling, 70, 2-10.

Vasiliev, A., M. Kanevskiy, G. Cherkashov, and B. Vanshtein. 2005. Coastal dynamics at the Barents and Kara Sea key sites. Geo-Marine Letters, 25, 110-120.

Vasiliev, A., I. Streletskaya, G. Cherkashev, and B. Vanshtein. 2006. Coastal dynamics of the Kara Sea. Kriosfera Zemli (Earths Cryosphere), 10, 5667.

Vyalov, S. S. 1959. Rheological bases of soil mechanics [in Russian]. Izdatelstvo Akademii Nauk SSSR.

Wadhams, P. and M. J. Doble. 2009. Sea ice thickness measurement using episodic infragravity waves from distant storms. Cold Regions Science and Technology, 56, 2, 98-101.

Walvoord, M. A. and B. L. Kurylyk. 2016. Hydrologic impacts of thawing permafrostA review. Valdose Zone Journal, 15, 6.

Wang, R., and H. H. Shen. 2010. Gravity waves propagating into an ice-covered ocean: A viscoelastic model. Journal of Geophysical Research Oceans, 115, C6, C06024.

Westermann, S., M. Langer, J. Boike, M. Heikenfeld, M. Pere, B. Etzelmüller, and G. Krinner. 2016. Simulating the thermal regime and thaw processes of ice-rich permafrost ground with the land-surface model CryoGrid 3. Geoscientific Model Development, 9, 523-546.

White, F.M., M.L. Spaulding, and L. Gominho. 1980. Theoretical examples of the various mechanisms involved in iceberg deterioration in the open ocean environment. National Technical Information Service Publication CG-D-62-8081-20571, Springfield, Virginia.

Wilchinsky, A. V., and D. L. Feltham. 2004. A Continuum Anisotropic Model of Sea-Ice Dynamics. Proceedings of the Royal Society London A, 460, 2105-2140.

Wobus C., R. Anderson, I. Overeem, N. Matell, G. Clow, and F. Urban. 2011. Thermal erosion of a permafrost coastline: improving process-based models using time lapse photography. Arctic, Antarctic, and Alpine Research, 43(3), 474-484.

Woo, M.-k. 2012. Permafrost hydrology. Springer-Verlag, Berlin, Germany.

Young, I. R. 1999. Wind generated ocean waves, Elsevier Publishing.

Zhang, Y., W. Chen, and D. W. Riseborough. 2006. Temporal and spatial changes of permafrost in Canada since the end of the Little Ice Age. Journal of Geophysical Research, 111, D22103.

Zhang, J., A. Schweiger, M. Steele, and H. Stern. 2015. Sea ice floe size distribution in the marginal ice zone: Theory and numerical experiments. Journal of Geophysical Research, 120, 3484-3498.

DISTRIBUTION:

1	MS 0359	D. Chavez, LDRD Office, 1911
1	MS 0899	Technical Library, 9536 (electronic copy)


Sandia National Laboratories